Università degli Studi di Napoli “Parthenope”

Dipartimento di Ingegneria

Doctoral Course (PhD) in

Information and Communication Technology and Engineering

XXXVIII Cycle

Advanced Nanophotonic Biosensors for Ultrasensitive Biomedical Detection

Supervisors: Dr. Vito Mocella (ISASI-CNR)
Prof. Stefania Campopiano
Dr. Silvia Romano (ISASI-CNR)

Candidate: Aida Seifalinezhad Mamaghani

Coordinator: Prof. Agostino Iadicicco

Academic Year 2024/2025

Abstract of the thesis

This thesis presents the development of advanced photonic platforms for biosensing, integrating nanostructured optical architectures, functional materials, and tailored surface chemistries to achieve high sensitivity and selectivity in biomolecular detection. The research bridges fundamental photonic principles with practical diagnostic applications, advancing the field of integrated photonic biosensors both conceptually and technologically.

The first part establishes the theoretical foundations of photonic crystals, exploring light–matter interactions, photonic band structures, and the phenomenon of bound states in the continuum (BIC), which enables ultra-high-Q resonances and extreme light confinement. Building on these principles, the thesis further investigates their implementation in biosensing architectures, supported by an in-depth analysis of optical transduction mechanisms and surface functionalization strategies essential for specific biochemical recognition.

Experimentally, the work demonstrates three major photonic sensing platforms. The first one is a molecularly imprinted polymer (MIP) sensor integrated with a BIC-based nanostructure for the selective, label-free detection of Transforming Growth Factor Beta (TGF-β), achieving femtomolar detection limits and robust performance in complex media. The second sensing platform involves a microfluidic-integrated photonic crystal slab used to investigate the interaction between Secreted Protein Acidic and Rich in Cysteine (SPARC) and Human Serum Albumin (HSA), providing precise real-time kinetic analysis with nanomolar accuracy. These activities were carried out at the Istituto di Scienze Applicate e Sistemi Intelligenti “Eduardo Caianiello” (ISASI) of the Consiglio Nazionale delle Ricerche (CNR) in Naples that also provided the funding for the PhD scholarship. The final platform employs bimodal waveguide interferometry for small-molecule sensing, as shown by ibuprofen detection with optimized surface chemistries and competitive immunoassays. This activity was carried out during an exchange period at the Institut Català de Nanociència i Nanotecnologia (ICN2) in Barcelona. Together, these devices illustrate how resonance phenomena and biochemical functionalization can be effectively combined to achieve both sensitivity and specificity across a broad range of analytes.

The thesis is structured to follow a logical progression from the illustration of the theoretical background up to the experimental results obtained. Chapter 1 introduces the fundamental principles of photonic crystals, describing their underlying physical mechanisms, classification schemes, and the role of bound states in the continuum in achieving high-Q optical resonances. Chapter 2 then examines the main classes of optical biosensors and discusses the essential aspects

of surface functionalization, thus providing the theoretical and practical foundation for subsequent device development. Based on this foundation, Chapter 3 presents the design and realization of a BIC-based molecularly imprinted polymer sensor for the detection of TGF-β, whereas Chapter 4 investigates dynamic protein–protein interactions through a photonic crystal slab integrated with microfluidic handling. The final experimental chapter, Chapter 5, explores the potential of bimodal waveguide interferometry in small-molecule sensing, highlighting its prospective relevance for pharmaceutical applications. The thesis concludes with perspectives on the future development of integrated photonic biosensing systems toward multiplexed, portable, and clinically relevant applications.

List of contents

Chapter 1: Fundamentals and Properties of Photonic Crystals

1.1 Introduction

Photonic crystals (PhCs) are a class of optical materials with periodic variations in refractive index on the scale of the wavelength of light. Due to this periodic dielectric structuring, PhCs exhibit photonic band gaps (PBGs), which are the frequency ranges in which electromagnetic waves are forbidden from propagating in the material [1]. In principle, a photonic crystal shapes the flow of light in a manner analogous to how a semiconductor lattice influences electron wavefunctions [2]. PhCs were first theorized in 1987 by E. Yablonovitch and S. John, who independently proposed that a periodic dielectric lattice could prevent light propagation at certain frequencies [3]. Yablonovitch envisioned inhibiting spontaneous emission in a structured dielectric to improve semiconductor laser efficiency [2], while John suggested strong localization of photons in disordered periodic structures [4]. These pioneering ideas marked the birth of photonic crystal research, establishing the term “photonic crystal” for such periodic optical media [5].

The historical development of photonic crystals has been characterized by rapid theoretical and experimental progress. Following the initial proposals in 1987, Yablonovitch and Gmitter attempted the first 3D photonic band gap structure in 1989 by drilling a periodic array of air holes in a dielectric, achieving a microwave-range PBG [2]. Although this first structure, known as Yablonovite, exhibited only a pseudogap due to anisotropy, it sparked extensive theoretical work. In 1990, K. M. Ho et al. confirmed via full-vector eigenvalue computations that a diamond-like lattice could support a complete 3D band gap [6]. By 1998, the first optical-wavelength 3D photonic crystal with a complete band gap was demonstrated by S. Y. Lin et al. using layer-by-layer microfabrication [7]. Two-dimensional (2D) photonic crystals were realized in the late 1990s as well, notably with the development of photonic crystal fibers (PCFs) by P. St. J. Russell and co-workers, where a periodic array of air holes in a fiber cladding enabled novel guided modes [8]. The early 2000s saw the integration of photonic crystals into semiconductor lasers and LEDs, achieving low-threshold lasing and enhanced light extraction by exploiting PBG effects [9]. Over the past three decades, photonic crystals have developed from a theoretical concept into a robust and versatile platform enabling diverse photonic applications.

Photonic crystals are critically important to the progression of both photonics and nanotechnology. By offering unprecedented control over the propagation of light, PhCs enable phenomena such as inhibited spontaneous emission, high-reflectivity mirrors just a few wavelengths thick, and waveguides with engineered dispersion (including ultra-slow light propagation). They play a key role in optical communication (such as PCF for fiber optics), optoelectronics (photonic crystal LEDs and lasers), sensing, and even quantum information processing. For instance, photonic crystal nanocavities can localize light to sub-wavelength volumes with high Q-factor, enhancing light–matter interactions for quantum emitters or nonlinear optics. In nanotechnology, the ability to confine and channel light in sub-micron patterns has enabled on-chip optical circuits and all-optical components that complement electronic integrated circuits [8]. Photonic crystals also appear in nature, the rainbow-like colors found on particular butterfly wings and opals arise from natural photonic crystal structures that manipulate light via periodicity. In fact, PhCs have had a transformative impact on photonics by providing a versatile route to engineer the spectral and spatial properties of light.

In In this chapter, the fundamental concepts and properties of photonic crystals are introduced, establishing a foundation for the more advanced topics in subsequent chapters. The discussion begins with the core principles of nanophotonic light–matter interaction and Maxwell electromagnetic theory as applied to photonic crystals (Section 1.2). Photonic crystals are then formally defined, and their classification by dimensionality (1D, 2D, 3D) (Section 1.3) is surveyed, including an introduction to lattice structures and Brillouin zones. In Section 1.4, photonic band structures and band gaps, the central concept underlying many photonic crystal phenomena, are examined, including analogies with electronic bandgaps, design principles for achieving PBGs, and the roles of polarization and computational methods in band structure calculations. Section 1.5 discusses an advanced phenomenon, bound states in the continuum (BICs), that can arise in photonic crystals and its significance in trapping light, which is also one of the main focuses of this thesis. This thesis focuses in particular on BICs in photonic crystal slabs and their application in biosensing. Accordingly, this chapter emphasizes the aspects of photonic crystal theory, fabrication, and applications that are most relevant to understanding BIC formation, their dispersion characteristics, and their utilization in practical devices. Section 1.6 reviews fabrication techniques for photonic crystals, from lithography to self-assembly, along with fabrication challenges. Section 1.7 surveys the materials used in photonic crystals (common high-index dielectrics, metallic/plasmonic structures, and examples of natural photonic crystals). In Section 1.8, the optical properties of photonic crystals and their control of light, including propagation, diffraction, waveguiding, defect-localized modes, and dispersion, slow-light effects, are described. Finally,

Section 1.9 highlights key applications of photonic crystals in fibers, lasers, LEDs, solar cells, and emerging areas such as quantum computing, optical circuits, and nonlinear optics.

1.2 Foundations of Nanophotonics Relevant to Photonic Crystals

1.2.1 Light–Matter Interaction at the Nanoscale

At sub-micron length scales, comparable to optical wavelengths, light–matter interactions differ markedly from bulk optics. When structured on the scale of hundreds of nanometers, dielectrics can manipulate photons in ways analogous to how atomic lattices manipulate electron waves [10]. In nanophotonics, interference and diffraction effects become pronounced, as nanostructures can induce strong Bragg scattering of light, creating band gaps that forbid propagation. Furthermore, the local optical density of states can be engineered. As an example, the Purcell effect describes modification (enhancement or suppression) of spontaneous emission due to changes in the local density of states [11]. At the same time, sub-wavelength resonators (like nanocavities in a photonic crystal) can enhance light–matter coupling for certain frequencies, enabling phenomena such as enhanced Raman scattering or low-threshold lasing. The interplay of nanoscale geometry and electromagnetic waves is the basis for photonic crystals ability to control light. Key physical processes at this scale include Bragg reflection, resonant cavity confinement, waveguide mode coupling, and slow-light dispersion, all of which will appear in our discussion of photonic crystal behavior. Indeed, photonic crystals utilize nanoscale periodic structures to control the propagation of light, forming allowed and forbidden photonic states analogous to how a semiconductor lattice defines allowed and forbidden electron energy bands [12].

1.2.2 Maxwell Equations and Electromagnetic Theory in PhCs

Photonic crystals are fundamentally described by Maxwell equations, the classical equations of electrodynamics, applied to a medium with a spatially periodic dielectric function. In source-free, linear, lossless dielectrics (no free charges or currents and ignoring absorption), Maxwell curl equations take the form:

$$\nabla \times \mathrm{E} = -\mu_0 \frac{\partial \mathrm{H}}{\partial \mathrm{t}}, \qquad \nabla \times \mathrm{H} = \varepsilon_0 \frac{\partial}{\partial \mathrm{t}} [\varepsilon(r)\mathrm{E}] , \tag{1-1}$$

with $\nabla \cdot [\varepsilon(\mathrm{r})\,\mathrm{E}]=0$ and $\nabla \cdot \mathrm{H}=0$ in the absence of free charges. Here E is the electric field, H the magnetic field, $\mathrm{D} = \varepsilon_0\, \varepsilon_\mathrm{r}(\mathrm{r})\,\mathrm{E}$ is the electric displacement, and $\mathrm{B} = \mu_0\,\mathrm{H}$ is the magnetic flux density (assuming no magnetic response, relative permeability $\mu_\mathrm{r} = 1$).

By taking the curl of Faraday law $\nabla \times \mathrm{E} = -\frac{\partial \mathrm{B}}{\partial \mathrm{t}}$ and substituting $\mathrm{B} = \mu_0 \mathrm{H}$ (with $\mu_r = 1$), we obtain $\nabla \times (\nabla \times \mathrm{E}) = -\mu_0 \frac{\partial}{\partial t}(\nabla \times \mathrm{H})$. Using Ampère law $\nabla \times \mathrm{H} = \frac{\partial D}{\partial t} = \varepsilon_0 \frac{\partial}{\partial t}[\varepsilon(\mathrm{r})\,\mathrm{E}]$, this becomes $\nabla \times (\nabla \times \mathrm{E}) = -\mu_0 \varepsilon_0 \frac{\partial^2}{\partial t^2}[\varepsilon(\mathrm{r})\,\mathrm{E}]$. Assuming a time-harmonic field $\mathrm{E}(\mathrm{r}, \mathrm{t}) = \mathrm{E}(\mathrm{r})\, e^{-i\omega t}$, we arrive at a wave equation for the electric field in the periodic medium:

$$\nabla \times [\nabla \times \mathrm{E}(r)] = \mu_0 \varepsilon_0 \omega^2 \varepsilon(r)\, \mathrm{E}(r)\,, \tag{1-2}$$

Similarly, by eliminating E in favor of H, one obtains an eigenvalue equation for the magnetic field often called the photonic crystal master equation [13]:

$$\nabla \times \left[\frac{1}{\varepsilon(r)} \nabla \times \mathrm{H}(r)\right] = \left(\frac{\omega}{\mathrm{c}}\right)^2 \mathrm{H}(r)\,, \tag{1-3}$$

which is an eigen-problem for the field profiles and allowed frequencies in a photonic crystal. Equation (1-3) states that we seek solutions for the magnetic field $\mathrm{H}(\mathrm{r})$ that satisfy a linear eigenvalue equation, where $(\omega/\mathrm{c})^2$ is the eigenvalue and $\mathrm{H}(\mathrm{r})$ the eigenfunction. The differential operator $\nabla \times (\frac{1}{\varepsilon(r)} \nabla \times)$ is Hermitian and positive-definite under appropriate boundary conditions, ensuring real eigenvalues for ω^2. An analogous wave equation can be written for $\mathrm{E}(\mathrm{r})$ as well, but working with H is often advantageous in dielectric structures (since H is divergence-free and continuous across dielectric boundaries) [14]. These formulations, often called the master equations of photonic crystals, form the basis for solving photonic band structures. The spatial variation of permittivity, $\varepsilon(\mathrm{r})$, couples the electromagnetic field throughout the periodic unit cell, leading to the formation of Bloch modes as discussed next.

The wave equation (1-3) is an eigenvalue problem with a periodic coefficient $1/\varepsilon(\mathrm{r})$. By Bloch theorem, the eigenmodes in a periodic medium can be chosen as Bloch waves. That is, solutions can be written in the form:

$$\mathrm{H}_{\mathrm{n,k}}(r) = \mathrm{u}_{\mathrm{n,k}}(r)\; e^{\,i\,\mathrm{k}\cdot\mathrm{r}}\,, \tag{1-4}$$

where n is the band index and k is the wavevector (crystal momentum) confined to the first Brillouin zone of the lattice. The function $\mathrm{u}_{\mathrm{n,k}}(\mathrm{r})$ is periodic with the same periodicity as the photonic crystal lattice within the first Brillouin zone, satisfying $u_{(n,k)}(\mathrm{r} + \mathrm{R}) = u_{(n,k)}(\mathrm{r})$ for any lattice vector R. Bloch theorem applies because Maxwell equations (in source-free linear media) are

linear and the material parameters ε(r) are periodic. Consequently, electromagnetic modes in a photonic crystal can be characterized by a wavevector k.

By substituting the Bloch form into the master equation, one can derive the eigenvalue problem for each k: for a fixed wavevector k, one solves

$$\nabla \times \left(\frac{1}{\varepsilon(r)} \nabla \times \mathrm{H}_{\mathrm{n,k}}(r) \right) = (\frac{\omega_{\mathrm{n}}(k)}{\mathrm{c}})^2 \mathrm{H}_{\mathrm{n,k}}(r)\,, \qquad (1\text{-}5)$$

subject to Bloch-periodic boundary conditions on u in the Brillouin zone, forming the r. This yields discrete eigenfrequencies $\omega_{\mathrm{n}}(\mathrm{k})$ for each k photonic band structure. The Bloch modes $\mathrm{H}_{\mathrm{n,k}}$ (and corresponding E) form a complete orthonormal set for expanding arbitrary electromagnetic fields in the periodic structure. An important consequence of Bloch theorem in photonic crystals is that one can restrict analysis to the fundamental domain (one unit cell) in real space and the first Brillouin zone in k-space, greatly simplifying both theoretical and computational analysis.

Formulating Maxwell equations as an eigenvalue problem reveals key parameters that photonic crystal designers can tune. The contrast in $\varepsilon(\mathrm{r})$ between high- and low-index regions is crucial, as a higher dielectric contrast generally produces wider photonic band gaps. The lattice geometry (period a, lattice symmetry, filling fraction of high-index material) determines the existence and size of band gaps. For example, a 2D square lattice of high-index rods in air supports a TE-polarized band gap, whereas a triangular lattice of air holes in high-index dielectric supports a TM gap, these choices relate to how $\varepsilon(\mathrm{r})$ modulates the field for each polarization. The master equation also indicates scaling properties: if all lengths in the PhC are scaled by a factor, the band structure frequencies scale inversely (since Maxwell equations are scale-invariant) [6]. This approach is useful for designing photonic crystals across different operational wavelength bands, from microwave to optical, as a structure can be designed at one scale and then geometrically scaled to operate at another frequency. Another implication is that introducing defects (breaking periodicity locally) creates localized eigenmodes within the band gap, corresponding to allowed states (cavity or waveguide modes) at frequencies where the perfect periodic structure would forbid propagation.

1.3 Definition and Classification of Photonic Crystals

1.3.1 What Are Photonic Crystals?

Photonic crystals are periodic dielectric structures that affect the propagation of light in a manner analogous to how the periodic potential in a semiconductor crystal affects electron motion.

Formally, a photonic crystal is defined by a spatially periodic refractive index $n(r)$ (or dielectric constant $\varepsilon(r)$) with periodicity on the order of the wavelength of interest [15]. This periodic modulation gives rise to a photonic band structure, which defines the allowed optical modes and band gaps for photons, analogous to the electronic band structure in a semiconductor. The presence of a PBG means that light at certain frequencies cannot propagate within the crystal, similar to the way an electronic band gap restricts electron propagation at certain energies in a semiconductor. Because of this, photonic crystals can exhibit unique optical phenomena like complete reflection of certain frequency bands, localization of light around defects, and unusual dispersion relations [16].

1.3.2 Classification Based on Dimensionality

Photonic crystals are commonly classified by the dimensionality of their periodicity: one-dimensional (1D), two-dimensional (2D), or three-dimensional (3D) [17][18]. This refers to the number of spatial directions in which the refractive index is periodically modulated. Figure 1.1 shows the classification of photonic crystals into 1D, 2D, and 3D types, based on their periodic arrangement.

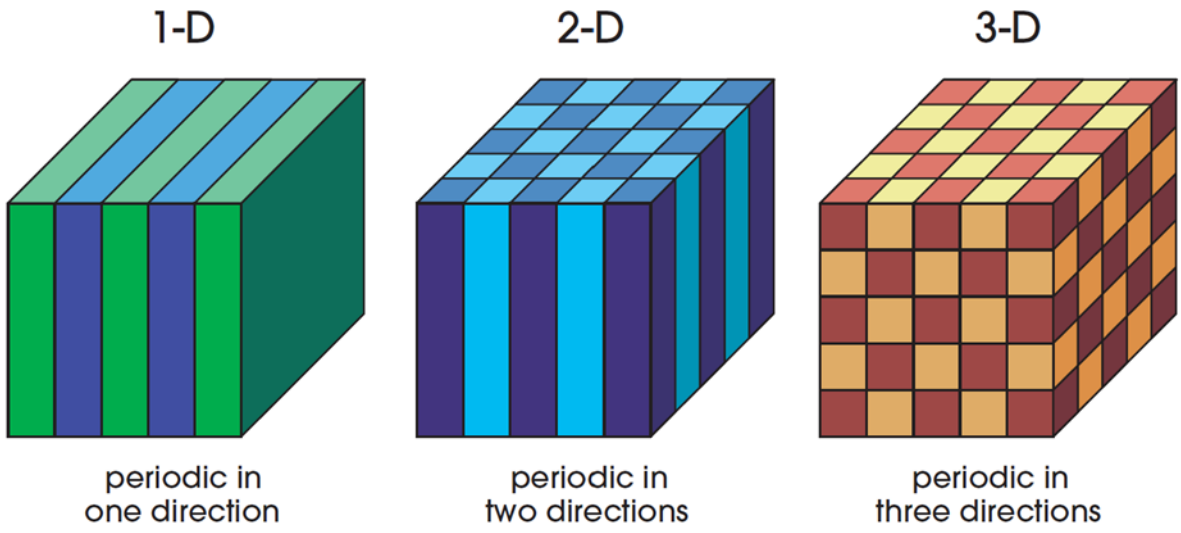

Figure 1.1: Simple examples of one-, two-, and three-dimensional photonic crystals. The different colors represent materials with different dielectric constants. The defining feature of a photonic crystal is the periodicity of dielectric material along one or more axes [19].

A 1D photonic crystal features a refractive index that varies periodically along a single spatial axis, remaining uniform along the other two axes. A classic example is the multilayer dielectric mirror, or distributed Bragg reflector (DBR), which comprises alternating layers of high- and low-index materials stacked together [18]. A typical one-dimensional photonic crystal is a multilayer mirror

composed of alternating SiO_2 and TiO_2 layers. These structures exhibit stop bands in their transmission spectrum, where reflectance approaches unity; they effectively forbid light in a certain wavelength range from propagating through, this is a 1D photonic band gap. Because periodicity is only in one direction, light propagating along that axis sees a periodic potential, whereas in the transverse directions light behaves as in a homogeneous medium [20]. Figure 1.2 illustrates a 1D photonic crystal, a multilayer film with alternating refractive index forms a periodic stack that strongly reflects certain wavelengths.

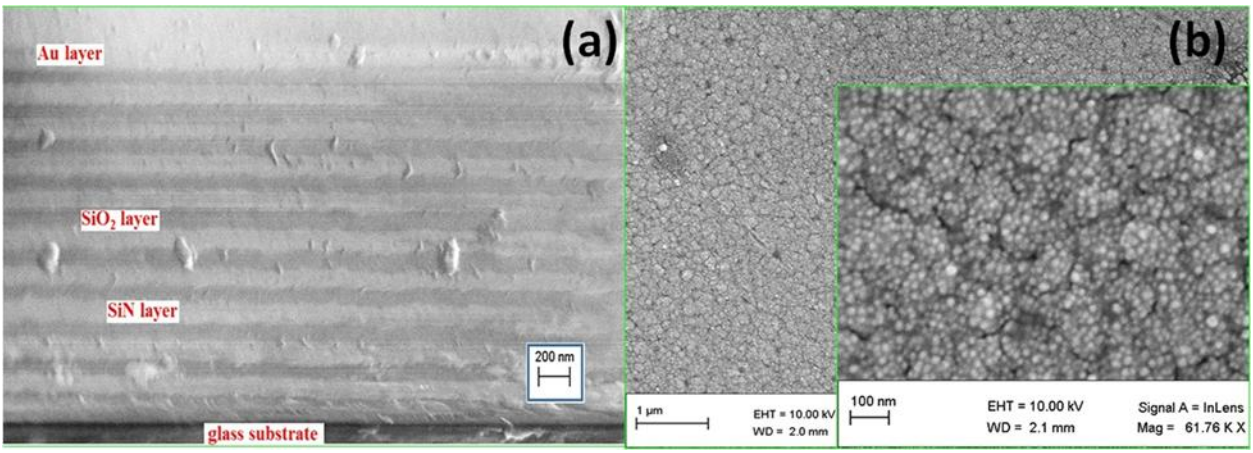

Figure 1.2: SEM images of the ten-layer 1D photonic crystal (1D-PhC) composed of alternating SiO_2/SiN layers deposited on a glass substrate and terminated with an Au film (60 s deposition). (a) Cross-sectional view showing the multilayer structure. (b) Top-view images of the Au layer at two different magnifications [21].

Because of their simple structure, 1D photonic crystals are the easiest to fabricate and analyze. Despite their simplicity, 1D photonic crystals are useful, for example, as high-reflectivity mirrors in VCSELs. However, their band gaps apply only to light propagating along the periodic axis; light from other angles can typically propagate via different Bragg orders.

In a 2D photonic crystal, the refractive index is periodic in two orthogonal directions (x and *y*), and uniform in the third *z* direction. Typically, 2D photonic crystals are implemented as slabs or planar waveguide structures. For example, a thin slab of high-index material, such as silicon, can have a periodic array of air holes etched in a two-dimensional lattice [22]. The slab guides light by index confinement in the vertical (*z*) direction, while the in-plane 2D periodic pattern creates a photonic band structure for the guided modes. Alternatively, one can have a 2D array of high-index rods in a low-index background (such as dielectric pillars in air). In either case, light propagating in-plane (within the high-index layer or rod array) experiences a 2D periodic dielectric environment. A

prominent example is the photonic crystal membrane, a silicon slab patterned with a triangular array of air holes. This structure can exhibit a band gap for in-plane propagation of transverse-electric-like (TE-like) modes, enabling strong in-plane light confinement [23]. Figure 1.3 shows an example of a 2D photonic crystal slab.

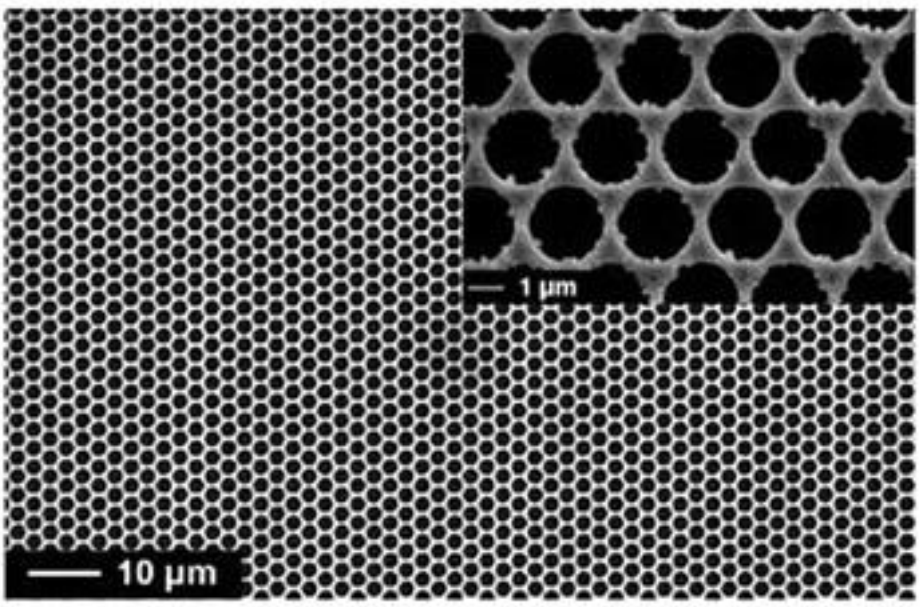

Figure 1.3: Top-view SEM image of the structure grown on patterned Si (111) substrate, showing a two-dimensional hexagonal array of holes [24].

In 2D photonic crystals, light propagation in the plane is governed by a two-dimensional band structure. One dimension (usually out-of-plane) is not periodic, which often means only certain polarizations or guided modes are strictly controlled by the lattice. For example, in a slab with holes, the modes can be categorized into TE-like (electric field predominantly in-plane) or TM-like (magnetic field in-plane); the 2D lattice may open a band gap for one polarization but not the other [25]. 2D PhCs are widely used to realize photonic crystal waveguides (by creating a line defect in the lattice) and nanocavity resonators (by creating a point defect). These have applications in integrated photonics for bending, splitting, or slowing light on chips. Fabrication of 2D photonic crystals is achievable with standard lithography and etching techniques, making them one of the most researched and utilized forms of photonic crystals [17].

A 3D photonic crystal has periodic refractive index modulation in all three spatial dimensions. This is the most general (and challenging) case, comparable to an ideal photonic bandgap crystal where light can be forbidden from propagating in any direction within a certain frequency range. A perfect

3D photonic band gap prohibits spontaneous emission across all directions and polarizations of light [14]. Numerous geometries have been explored for 3D photonic crystals. The earliest successful 3D lattice was the Yablonovite structure, consisting of a three-dimensional array of air holes drilled into a dielectric block in a face-centered-cubic-like arrangement [26]. Another common 3D lattice is the inverse opal structure, made by self-assembling silica or polymer spheres into an fcc lattice and then infilling with high-index material and removing the original spheres [4]. Figure 1.4 illustrates an example of a 3D photonic crystal structure.

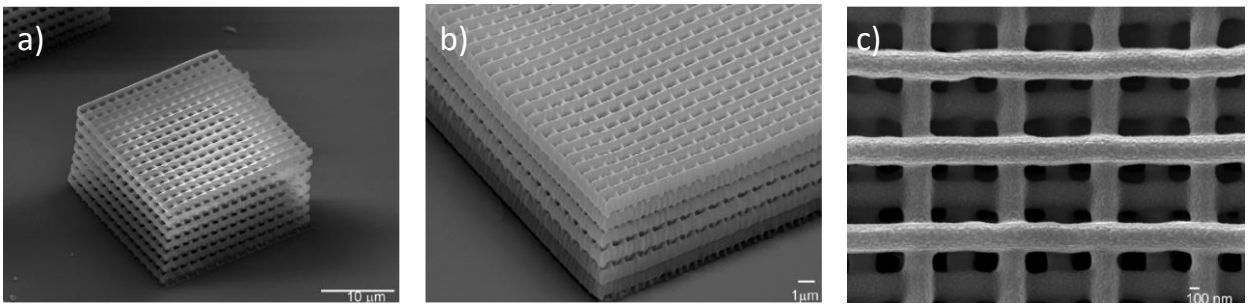

Figure 1.4: a) SEM image of three-dimensional photonic crystal structures; b) detailed view of a single structure; c) top-view image of the structure [27].

Ideal 3D photonic crystals are complex to fabricate, but significant progress has been made. Techniques such as layer-by-layer lithography, holographic lithography, and two-photon polymerization have yielded 3D structures at optical length-scales [17]. Natural examples of 3D PhCs include opals (colloidal crystal of silica spheres, forming a quasi-fcc lattice of spheres in air) and certain butterfly wing scales which form 3D photonic networks [28]. 3D photonic crystals are the only way to obtain an omnidirectional band gap (affecting all polarizations and directions). While 1D and 2D PhCs can have partial band gaps, a 3D PhC is required for a complete PBG. Consequently, three-dimensional photonic crystals are of significant interest for applications such as omnidirectional mirrors, cavity quantum electrodynamics (QED) experiments, where suppression of all vacuum modes except a localized defect mode is desired, and thermal emission control.

1D PhCs function as multilayer mirrors with angular- and frequency-specific band gaps. 2D PhCs provide in-plane band gap control and are common in planar photonic circuits and fibers. 3D PhCs, though challenging to fabricate, can exhibit complete band gaps. Applications include Bragg mirrors and filters (1D), photonic circuits and fibers (2D), and advanced emission control and optical insulation (3D).

1.3.3 Lattice Structures and Brillouin Zones in PhCs

The periodic structure of a photonic crystal can be described by a lattice in real space and a corresponding reciprocal lattice in k-space. Understanding lattice geometry is essential for analyzing photonic band structures and identifying band gaps, since the Brillouin zone and high-symmetry k-points will determine where band gaps occur.

In solid-state physics terms, the reciprocal lattice of a photonic crystal is defined by vectors G such that $e^{i(\mathbf{G}\cdot\mathbf{r})}$ has the periodicity of the real-space lattice. The first Brillouin zone is the Wigner–Seitz cell of the reciprocal lattice; geometrically, it represents the region in k-space that is closer to the origin than to any other reciprocal lattice point. The Brillouin zone is essential for band structure calculations, as photonic band diagrams are typically obtained by computing eigenfrequencies ω(k) for k values along the boundary of the irreducible Brillouin zone (IBZ) [29]. High-symmetry points on the Brillouin zone boundary (such as Γ, X, M, K in 2D lattices) are where band extrema and gaps often occur, due to Bragg diffraction meeting the Bragg condition for zone-edge wavevectors.

For example, a square lattice in real space with period a along x and *y*, has a square reciprocal lattice with lattice constant 2π/a. Its first Brillouin zone is a square in k-space (possibly rotated 45° depending on basis choice), with typical high-symmetry points labeled Γ (center), X (midpoint of a side, along k_x or k_y direction), and M (corner of the BZ, at 45° direction) [30]. A hexagonal (triangular) lattice in real space corresponds to a hexagonal reciprocal lattice, whose first Brillouin zone is a hexagon, with high-symmetry points Γ (center), M (midpoint of edge), and K (corner of the hexagon). Figure 1.5 illustrates the Brillouin zones for square vs. hexagonal 2D lattices.

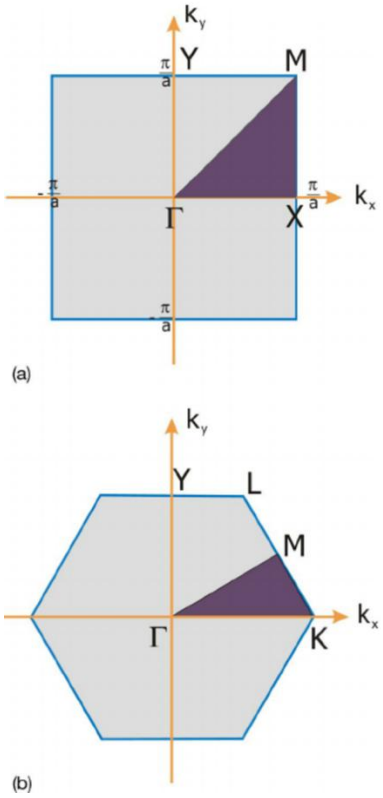

Figure 1.5: Brillouin zones for two example 2D lattices. (a) Square lattice real-space geometry and its first Brillouin zone (shaded region) in reciprocal space, a square with Γ at center, and X, M indicating midpoint and corner symmetry points. The irreducible Brillouin zone for the square lattice is the triangular region Γ–X–M (due to fourfold symmetry). (b) Hexagonal (triangular) lattice and its reciprocal lattice Brillouin zone, a hexagon with Γ at center, M at the face centers, and K points located at the vertices. The IBZ is a triangle Γ–M–K given the sixfold symmetry. Photonic band structures are typically plotted along the IBZ perimeter (such as Γ → X → M → Γ for square lattices, or Γ → M → K → Γ for hexagonal lattices) to identify bandgap frequencies [31].

Lattice symmetries play a key role in defining polarization degeneracies and governing the selection rules that determine the formation of band gaps [32]. For example, a hexagonal lattice exhibits sixfold (C_6) symmetry, which can produce degenerate modes at the K point, while a square lattice, with fourfold (C_4) symmetry, results in a different mode ordering. The concept of the irreducible Brillouin zone helps reduce computational effort, as it is sufficient to calculate the band structure only within the IBZ, with the remaining portions reproduced by symmetry [17] [33].

The Brillouin zone is the natural domain for photonic crystal dispersion relations. Photonic band diagrams usually plot frequency ω (or normalized frequency such as a/λ) vs. wavevector along a path connecting high-symmetry points of the BZ. Band gaps are identified as frequency ranges with no bands for all k in the Brillouin zone. The real-space lattice and its reciprocal determine where

those gaps occur (e.g., at zone boundary X or M), making a solid understanding of lattice and Brillouin zone geometry essential for photonic crystal analysis [5].

The two common 2D lattice types for photonic crystals are square lattices and hexagonal (triangular) lattices. Each has distinct Brillouin zone shapes and thus different band structures and potential for band gaps. In a square lattice of dielectric rods or air holes, the real-space symmetry is C_4 and the reciprocal lattice is square. The irreducible Brillouin zone is a right triangle Γ–X–M. Band gaps in square lattices often occur at zone boundaries (such as between first and second bands at the M point). For dielectric rods in air, a TE-polarized band gap can appear (as the electric field is primarily confined within the high-index rods), whereas for air holes in dielectric, a TM gap is more likely (magnetic field in-plane, electric field out-of-plane) because the continuous high-index background supports TE modes, while isolated high-index rods tend to favor TM modes. In contrast, a hexagonal lattice (sixfold symmetry) has a hexagonal BZ with Γ–M–K as the IBZ triangle. Hexagonal lattices (such as triangular array of air holes) are known to readily produce large TE- polarized band gaps in high-index dielectric slabs. In general, the symmetry and connectivity of the lattice play a crucial role in determining whether a complete band gap can form, and for which polarization it appears.

1.4 Photonic Band Structure and Bandgap

1.4.1 Concept of Photonic Band Structure

Just as electrons in a crystal have allowed energy bands and forbidden gaps, photons in a photonic crystal have allowed frequency bands and forbidden frequency ranges (band gaps) arising from the periodic structure. The photonic band structure describes the relationship $\omega(k)$ between the frequency ω (or often c/λ) of electromagnetic modes and their wavevector k in the crystal. It can be visualized in a band diagram, typically plotting normalized frequency (such as a/λ or $\omega a/2\pi c$) versus k along high-symmetry directions of the Brillouin zone [5].

In periodic dielectrics, Bragg scattering from the periodic index modulation causes standing-wave formation at Brillouin zone boundaries, leading to frequency gaps in the dispersion relation [34][35]. Figure 1.6 shows an example photonic band structure for a photonic crystal slab, highlighting key features. Allowed bands (continuous curves) represent propagating modes, while a photonic band gap appears as a frequency region with no bands (no allowed modes).

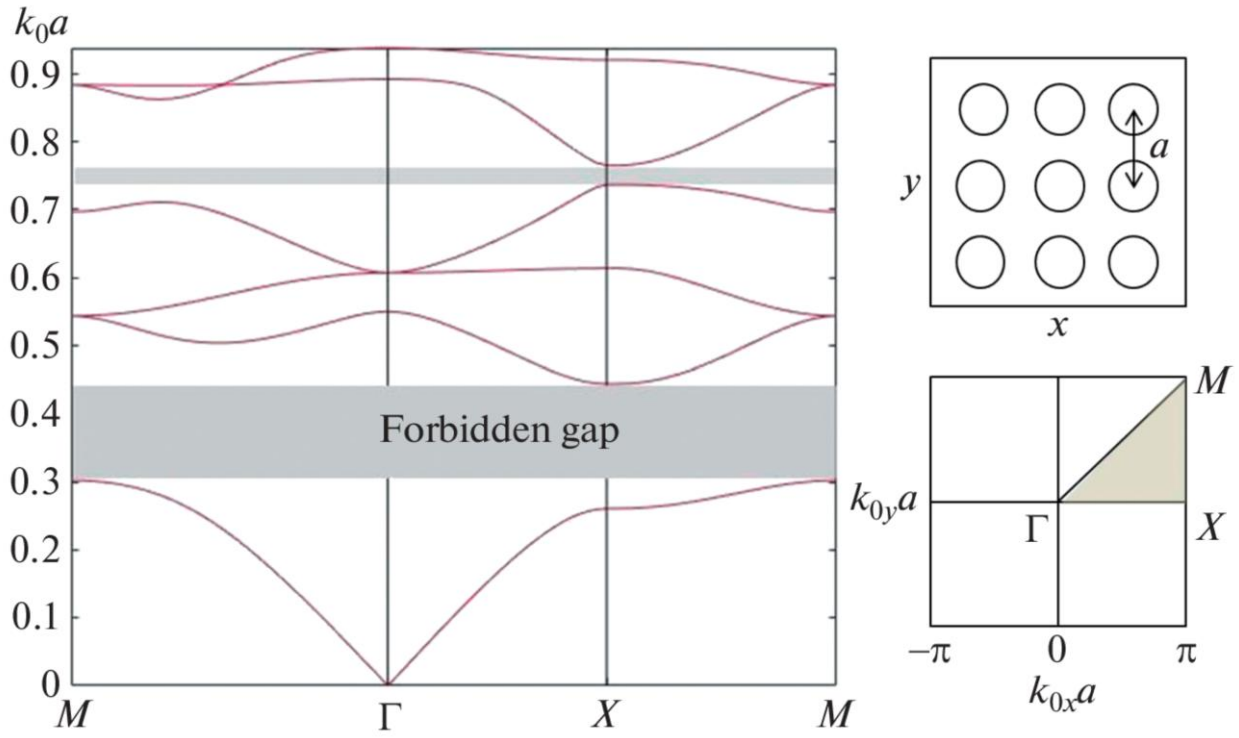

Figure 1.6: Band diagram for TM-polarized radiation (the electric field is directed along the cylindrical rods) in the case of dielectric cylinders constituting a square lattice in air. The radius of the rod is r/a = 0.18, where a is the lattice constant, and permittivity ε = 11.56 [36].

In an allowed band, photons have a well-defined group velocity (the slope of ω(k)) and can propagate through the crystal. Within a band gap, no propagating solutions exist, causing light to be exponentially attenuated; the crystal therefore behaves like a mirror or a "stop-band" filter for those frequencies. The existence of a band gap requires sufficient refractive index contrast and a periodic arrangement that causes Bragg scattering in all relevant directions to cancel out propagating waves [37]. The central frequency of the gap and its width can be tuned by design (changing lattice constant, hole/rod radius, index contrast, etc.). The analogy to electronic band structures is useful, as allowed photonic bands correspond to permitted energy bands for electrons, while photonic band gaps resemble semiconductor bandgaps that prevent electrons or photons from existing within that energy or frequency range inside the crystal [38].

1.4.2 Photonic Bandgap

A photonic bandgap is a frequency interval over which the photonic crystal does not support any propagating electromagnetic modes [39]. In this range, electromagnetic waves incident on the photonic crystal will be reflected or will decay evanescently instead of propagating through. The physical origin of a photonic band gap is multiple Bragg scattering and interference. As light

propagates, it is Bragg-reflected by the periodic index variations, causing all possible propagation paths to interfere destructively and cancel any forward-moving wave [40]. This is directly analogous to how electrons with energies in the bandgap of a semiconductor cannot propagate through the periodic potential due to destructive interference of electron wavefunctions [17].

The significance of a complete photonic bandgap is profound. Within a PBG, spontaneous emission of an embedded light source is suppressed (if its emission frequency lies in the gap) because there are no available photon states for it to emit into. This was one of Yablonovitch original motivations: inhibiting spontaneous emission to improve laser efficiency[2][14]. A photonic band gap also allows for strong electromagnetic confinement. By introducing a defect (like removing a dielectric rod or hole) in an otherwise perfect photonic crystal, a localized mode can form at a frequency within the band gap. This mode remains trapped because the surrounding crystal prevents wave propagation at that specific frequency in all directions. Thus, photonic bandgaps facilitate lossless wavelength-scale cavity modes and waveguide modes that confine light to very small volumes. For example, a point defect in a 2D photonic crystal slab can localize light in all three dimensions at a bandgap frequency, yielding ultra-high Q optical resonators[14][41].

The bandgap concept also enables omnidirectional reflectors. A 3D photonic crystal with a complete bandgap reflects light from all directions within the gap frequencies, surpassing conventional dielectric mirrors, which are angle-dependent [42]. Even in 1D or 2D PhCs, a bandgap can provide high reflectivity in certain directions, enabling distributed Bragg reflectors, fiber Bragg gratings, etc. Another application is PCFs, which guide light through a low-index core by using a photonic crystal cladding. The cladding creates a band gap that confines the light, enabling hollow-core PCFs to guide light through air using this bandgap effect [43]. It should be noted that some fibers commonly referred to as photonic bandgap fibers operate based on anti-resonant mechanisms rather than a true bandgap in k-space. In this chapter, the focus is specifically on true bandgap effects.

1.4.3 Analogy with Electronic Bandgaps

The analogy between photonic crystals and semiconductor crystals was first recognized in the foundational studies on photonic crystals. In semiconductors, the periodic atomic lattice creates allowed electron energy bands and forbidden bandgaps, preventing electrons with energies in the gap from propagating [3]. Similarly, a photonic crystal periodic dielectric structure produces allowed and forbidden photonic bands, blocking light within certain frequency ranges, as illustrated in Figure 1.7.

This analogy extends to their mathematical foundations. Both Schrödinger equation for electron waves in a periodic potential and Maxwell equations for electromagnetic waves in a periodic dielectric can be expressed as eigenvalue problems of the form $\hat{A}\psi = \lambda\psi$. Conceptually, replacing the electron mass and potential with the dielectric permittivity $\varepsilon(r)$ reveals that the two systems share an equivalent eigenvalue structure. As a result, methods developed in solid-state physics, such as Bloch theorem and plane-wave expansions, can be directly applied to photonic crystals, giving rise to band structures analogous to electronic bands [4].

The similarity also appears in their density of states. In semiconductors, the electronic density of states drops to zero within the bandgap, while in photonic crystals, a full bandgap means no available photon modes. This results in suppressed spontaneous emission (since no photonic states exist, emission channels are closed) mirroring how an electronic insulator blocks current. Indeed, one of the early goals of photonic crystal research was to inhibit spontaneous emission through such photonic bandgaps. Even the concept of doping finds an optical counterpart. In semiconductors, introducing impurities creates localized electronic states within the bandgap. Likewise, defects in a photonic crystal, such as a missing rod or modified dielectric region, generate localized photonic modes that confine light, analogous to electrons bound to dopant atoms [14].

Both systems rely on Bragg reflection. In semiconductors, electron bandgaps arise from the interference of electron waves scattered by the periodic atomic potential. In photonic crystals, similar Bragg reflections of light at periodic dielectric interfaces create photonic bandgaps, completing the deep parallel between electronic and photonic periodic structures[44].

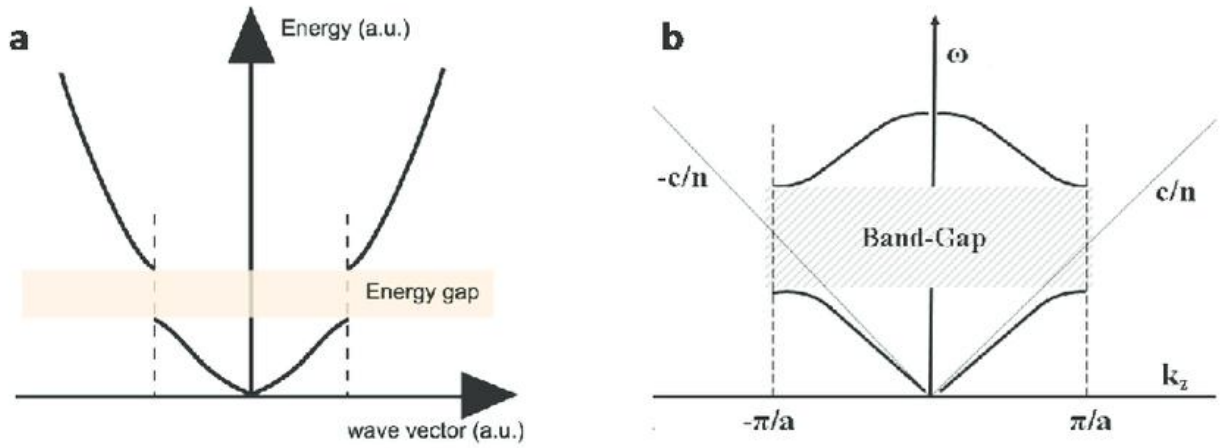

Figure 1.7: Analogy of (a) electronic bandgap in semiconductors vs. (b) photonic bandgap in PhCs [45].

1.4.4 Design Principles and Computational Methods

Designing a photonic crystal to achieve a desired bandgap requires precise control of several parameters. The lattice constant (a) determines the crystal periodicity and shifts the band structure in frequency. Increasing a lowers the normalized band frequencies, as they scale approximately with c/a. To target a specific wavelength λ_0, the lattice constant is typically chosen to be approximately λ_0/n_{eff}, where n_{eff} is the effective refractive index, allowing fine alignment of the bandgap with the desired frequency range.

The refractive index contrast (Δn) between high- and low-index regions largely determines the width and depth of the bandgap. A higher contrast, such as between air (n=1) and silicon (n=3.5), produces stronger scattering and broader gaps, while low contrast may yield only narrow or incomplete gaps. The filling fraction of the high-index material also affects the result, with an optimal value around 30% in 2D structures maximizing the bandgap. The lattice geometry and topology, whether consisting of air holes in a high-index slab or high-index rods in air, determine the symmetry and polarization of the band gap. TE gaps are generally supported by air holes in a high-index matrix, whereas TM gaps are favored by isolated high-index rods [46].

In slab photonic crystals, the thickness plays a key role in vertical confinement. If the slab is too thin, some modes radiate away, narrowing the in-plane bandgap. Generally, a thickness of at least half the wavelength is needed to maintain guided-mode gaps. Introducing defects, such as slightly modifying the size of one hole, creates localized or guided modes within the bandgap, enabling the design of optical waveguides or resonant cavities with tunable frequencies [47].

In practice, photonic crystal design relies on iterative numerical simulations, such as plane-wave expansion or FDTD methods, to optimize these parameters. Studies show that for a triangular lattice of air holes in a high-index slab, a hole radius of about 0.3–0.35 a yields the widest TE bandgap. When the index contrast is fixed by the material, tuning the ratio r/a becomes the most effective strategy for performance optimization [48].

In photonic crystals, bandgap formation depends strongly on the polarization of electromagnetic modes relative to the periodic plane. In a two-dimensional photonic crystal defined in the x–y plane and extending along z, modes are generally classified as transverse electric (TE-like) or transverse magnetic (TM-like) [49][50].TE-like modes have electric fields mainly within the plane of periodicity (Ex, Ey), with little or no component along z (Ez = 0). In ideal 2D systems of infinite rods, the magnetic field (Hz) can be nonzero, while in slab geometries, TE-like modes remain

predominantly in-plane. TM-like modes, on the other hand, have their magnetic fields largely in-plane and electric fields primarily along z (nonzero Ez, with Hx and Hy components) [51].

Photonic bandgaps differ between these polarizations because their fields interact differently with the dielectric structure. Continuous high-index networks confine the in-plane electric field, favoring TE bandgaps, while isolated high-index rods in a low-index background better confine magnetic fields, supporting TM bandgaps. Achieving a complete 2D bandgap that blocks both polarizations is difficult and typically requires combining features favorable to each polarization, using higher-symmetry lattices, or moving to a full 3D photonic crystal [52].

Analyzing photonic crystal band structures relies on computational methods, as analytical solutions exist only for simple one-dimensional cases. The most common approaches are Plane Wave Expansion (PWE), Finite-Difference Time-Domain (FDTD), and Finite Element Method (FEM). PWE works in the frequency domain by expanding the fields and inverse dielectric function as plane waves, converting Maxwell equations into a matrix eigenvalue problem. It efficiently computes band diagrams and field patterns for infinite periodic structures, especially with moderate index contrast, but is less suited for defects or non-periodic geometries without supercells [53].

FDTD solves Maxwell equations in the time domain on a spatial grid, allowing simulation of pulse propagation and direct observation of transmitted and reflected spectra to identify band gaps. It handles nonlinearities, dispersion, and imperfections but is more computationally intensive for fine spectral resolution. FEM, also a frequency-domain method, uses adaptive meshing to solve complex geometries and high-index contrasts, making it ideal for waveguides or defect cavities. Specialized methods like RCWA are used for layered or grating structures [54]. In practice, PWE is often used to design and optimize the bulk lattice, while FDTD or FEM models finite or irregular structures. Together, these computational tools enable visualization of band structures, identification of band gaps, and prediction of photonic crystal behavior beyond analytical possibilities.

1.5 Advanced Phenomena in Photonic Crystals

1.5.1 Bound States in the Continuum (BICs)

BICs are a unique wave phenomenon in which a localized optical mode remains perfectly confined even though its frequency lies within the radiation continuum, where coupling to free-space modes would normally lead to leakage. In the photonic band structure, BICs occur above the light line, within the region that typically supports radiative modes in open systems (Figure 1.8). Despite being embedded in this continuum, a BIC remains non-radiative due to destructive interference or

symmetry protection, resulting in an effectively infinite quality factor. The concept originates from quantum mechanics, where von Neumann and Wigner first demonstrated that specially tailored potentials could sustain localized states above the continuum threshold. In photonics, BICs provide a powerful mechanism for light confinement without loss in open structures such as photonic crystal slabs and dielectric metasurfaces [55].

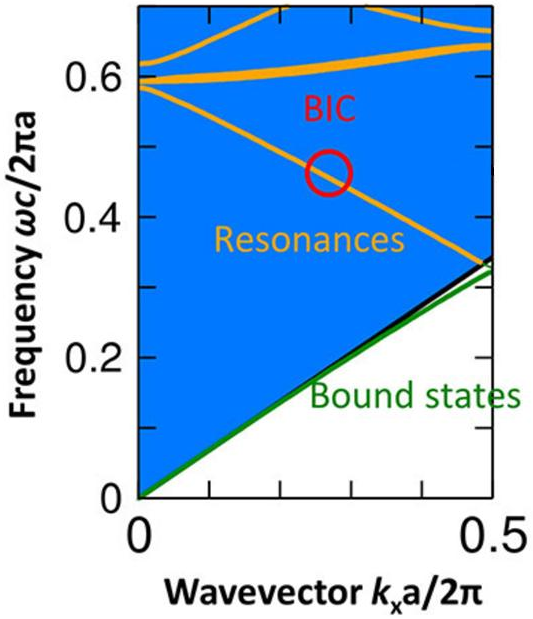

Figure 1.8 : Band structure of a photonic crystal slab. The area shaded in blue is above the light line, and so modes in this region can, in general, couple to radiation and are resonances with finite lifetime. However, at particular wavevectors (circled in red), exceptions (BICs) exist with infinitely long lifetime [56].

There are two main types of photonic BICs. Symmetry-protected BICs occur at highly symmetric points in the Brillouin zone, often at the Γ point (k = 0), where the mode symmetry prevents it from coupling to any radiating waves. For example, an antisymmetric mode may be unable to couple to symmetric far-field waves, remaining trapped despite lying above the light line. Friedrich-Wintgen BICs, or accidental BICs, arise from destructive interference between two leaky resonances. By tuning a structural parameter, the resonances cancel each other radiation, producing a non-radiating mode not dictated by symmetry [57]. In real structures, imperfections and finite size convert ideal BICs into high-Q quasi-BICs with long but finite lifetimes. Experiments have demonstrated photonic crystal slab resonances derived from BICs with Q-factors ranging from 10^4 to 10^6, making them highly promising for applications requiring strong light confinement [58].

BICs are highly attractive for applications requiring strong light confinement because they combine tight spatial localization and high field intensity with negligible radiative loss [59]. They enable

ultra-high-Q resonators and low-threshold lasers on-chip without full 3D photonic bandgaps, with real-world imperfections reducing the theoretically infinite Q to very high but finite values, ideal for lasers and nonlinear optics [60]. BICs also excel in sensing, as their sharp quasi-BIC resonances are highly sensitive to environmental changes like refractive index variations or molecular binding. They can trap light in low-index or normally leaky regions, such as air gaps in dielectric metasurfaces, enhancing light-matter interactions. Modes near a BIC often exhibit slow-light behavior due to flat dispersion, further amplifying nonlinear effects and potentially boosting light-atom coupling in quantum applications [60][61]. BICs appear in photonic crystal waveguides as symmetry-protected anti-radiation modes and can couple with radiating modes to produce Fano resonances, creating sharp, asymmetric spectral features useful for filtering and modulation. While perfect BICs are difficult to realize experimentally, high-Q quasi-BICs with Q-factors of 10^5–10^6 have been achieved, greatly surpassing typical guided resonances and demonstrating their practical value in photonics. BICs are especially attractive for sensing applications, as the quasi-BIC modes in photonic crystal slabs can be engineered for biosensing, and their theoretical concepts will be directly applied in the analysis of the devices studied in later chapters.

1.6 Fabrication Techniques of Photonic Crystals

Creating photonic crystal structures requires nanofabrication methods capable of defining periodic patterns with feature sizes on the order of the wavelength (hundreds of nm for visible/near-IR, or larger for microwave). Depending on dimensionality (1D, 2D, 3D) and material, different fabrication approaches are used. Key techniques and their associated challenges are overviewed here.

1.6.1 Lithographic Techniques: Electron-Beam Lithography, Photolithography

Lithography-based fabrication is a top-down approach well-suited for creating one- and two-dimensional photonic crystals on substrates [62]. Electron-beam lithography (EBL) offers sub-20 nm resolution and flexible pattern design, making it ideal for prototyping 2D structures like hole arrays or pillars in semiconductor layers. The process involves coating a resist, exposing the pattern with an electron beam, developing the resist, and etching it into the substrate. While EBL is slow due to its serial writing nature, it remains essential for research, enabling precise waveguides, cavities, and sensors with features around 100–200 nm [63].

Photolithography provides higher throughput for larger-scale structures, with traditional UV lithography limited to 0.5–1 μm resolution and deep-UV or immersion techniques reaching 100–200 nm. It is suitable for infrared or microwave photonic crystals, and interference lithography can

create periodic 1D, 2D, and even 3D patterns without a mask. Mask-based photolithography is commonly used for 1D structures, while advanced deep-UV methods can produce sub-micron 2D patterns over large areas. Nanoimprint lithography uses a patterned stamp pressed into a polymer resist to replicate nanoscale patterns quickly and cost-effectively over large areas. With 20–50 nm resolution, it is suitable for visible-wavelength photonic crystals and mass-manufacturing devices like LEDs or sensor chips.

Figure 1.9 demonstrates photonic crystal fabrication by lithography and etching, showing a triangular lattice of circular holes in resist and the etched silicon with nearly vertical sidewalls. These lithographic techniques enable precise 1D and 2D photonic crystal fabrication with minimal sidewall roughness, critical for reducing scattering losses. In this thesis, the photonic crystal slab sensors for biosensing applications were fabricated on a square lattice of cylindrical holes in silicon nitride (Si_3N_4) deposited on a SiO_2 substrate using plasma-enhanced chemical vapor deposition (PECVD). The pattern was defined via high-voltage electron-beam lithography, providing precise control over feature size and lattice periodicity, which is critical for BIC formation and optimal sensor performance.

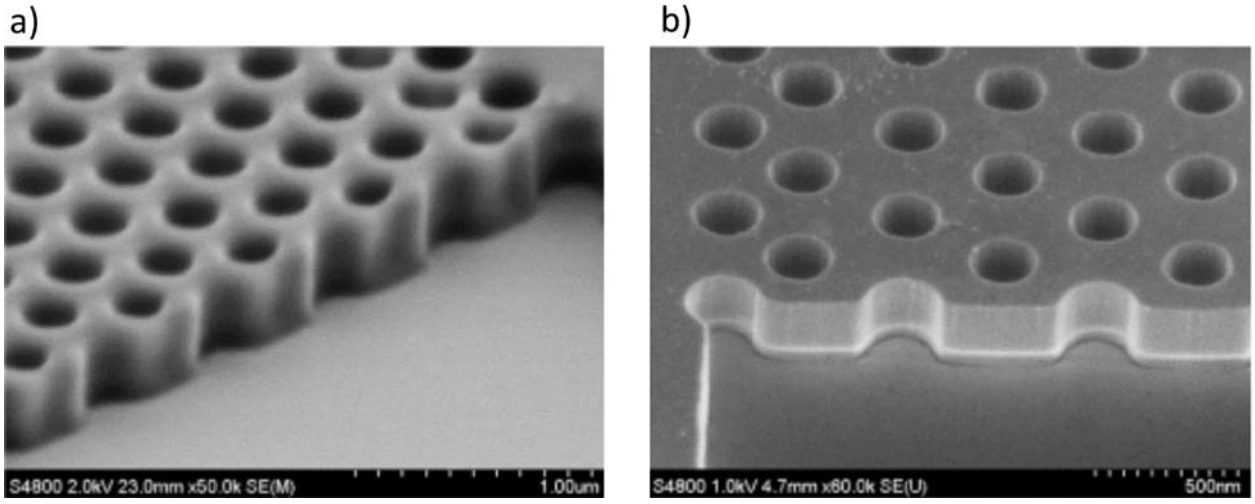

Figure 1.9: Fabrication of 2D photonic crystals. a) SEM image of the e-beam resist (ZEP520A) pattern on an SOI wafer. b) Photonic crystal pattern after etching, in silicon [64].

1.6.2 Self-Assembly Methods: Colloidal Crystals, Block Copolymers

Self-assembly approaches use natural organization processes to create periodic structures, making them valuable for three-dimensional photonic crystals that are difficult to fabricate with top-down lithography [65]. Colloidal self-assembly forms close-packed microsphere lattices, or opals, which can be converted into high-index inverse opals by infiltrating the voids with materials like silicon or

TiO_2. This produces large-area 3D crystals with near-optimal fcc geometry, though controlling defects, grain orientation, and complete infiltration remains challenging.

Block copolymer self-assembly enables nanoscale structures such as lamellae, cylinders, spheres, or gyroids, which can be converted into high-index materials supporting full photonic bandgaps. This method allows smaller features and more complex geometries than colloidal assembly but faces challenges in achieving long-range order and controlling orientation. Other self-assembly methods include DNA-guided nanoparticle lattices, biological templates like butterfly wings, microfluidic colloidal arrays, and liquid crystal-based tunable 1D structures. Natural photonic crystals also inspire synthetic designs, including chiral materials. Self-assembled photonic crystals provide a low-cost route to large 3D volumes, but defects and cracks are difficult to control, and adding designed features like waveguides is challenging. Combining self-assembly with lithography, such as patterned substrates or holographic exposure, can improve defect management and structural orientation [66].

1.6.3 Other Fabrication Approaches and Their Challenges

Beyond standard lithography and colloidal self-assembly, several specialized techniques enable complex and three-dimensional photonic crystal fabrication. Direct laser writing using two-photon polymerization can create intricate 3D structures such as woodpile and gyroid lattices with approximately 100 nm lateral and 300 nm axial resolution. These polymer templates can be converted to high-index materials, and defects or precise features can be incorporated, though the method is slow for large volumes and requires additional processing [67].

Deep reactive-ion etching (DRIE) with layer stacking builds 3D crystals by patterning and aligning multiple 2D layers, sometimes using angled etching or wafer bonding to form complex lattices. X-ray lithography (LIGA) can produce high-aspect-ratio 3D microstructures through multi-angle exposures, enabling polymer templates that can later be converted into inverse structures, though it is less commonly used in photonics [68]. Other approaches include chemical etching, focused ion beam milling for prototyping, and anisotropic etching in silicon for 1D or 2D crystals. At larger scales, microwave photonic crystals can be made by machining or stacking circuit boards, while terahertz structures can be fabricated via 3D printing, where feature sizes of tens of microns are sufficient.

Fabricating photonic crystals, especially three-dimensional and large-area devices, however, remains challenging. Dimensional accuracy and surface quality are critical, as small variations, rough sidewalls, or etch imperfections can increase scattering and losses, while high-Q cavities

require smooth, vertical features. Reproducibility and yield are also essential, since variations in lattice constants or hole sizes can shift bandgaps, and defects can degrade performance, particularly in slow-light waveguides. For 3D structures, precise alignment of multiple layers is crucial to maintain symmetry and prevent leakage.

Material constraints introduce additional complexity. Silicon and III-V semiconductors offer high index contrast, while polymers or metals may be required for certain applications, each presenting distinct fabrication challenges. Scaling and cost require trade-offs, since electron-beam lithography is precise but slow, while nanoimprint and self-assembly can cover larger areas with lower accuracy. Integration with other components demands precise mode matching and compliance with CMOS design rules.

Other challenges include aspect ratio limits for deep 3D etching and the fixed air filling fraction in inverse opals, which may not optimize the bandgap. Cracking during large-scale self-assembly is also an issue. Despite these hurdles, functional photonic crystal devices (lasers, LEDs, and fibers) have been realized. Techniques such as stacking capillaries for photonic crystal fibers or deep-UV lithography with multiple patterning for chip-scale waveguides demonstrate steady progress. As fabrication and integration improve, photonic crystals are expected to become increasingly widespread in optics.

1.7 Materials Used in Photonic Crystals

1.7.1 Dielectric and Metallic Materials

Photonic crystals require materials with high refractive index and low absorption at the operating wavelength. Silicon (n = 3.45) is ideal for infrared photonic crystals, offering strong confinement and wide bandgaps, though it is opaque in the visible. III-V semiconductors like GaAs, InP, and GaN enable active devices such as lasers and LEDs, operating from near-IR to visible, but are more challenging to fabricate [69].

Silica and other glasses have low indices (n = 1.45), limiting them to partial gaps, though they are widely used in photonic crystal fibers and self-assembled opals; higher-index glasses like chalcogenides enable infrared applications. Titanium dioxide (n = 2.5–2.7) is suitable for visible photonic crystals, while diamond (n = 2.4) offers transparency and thermal stability for quantum photonics. Polymers (n = 1.3–1.7) are easy to pattern for sensing or active devices but generally cannot support full bandgaps at optical frequencies. A complete photonic bandgap generally requires a high index contrast, often greater than 2:1, such as air combined with silicon or

multilayer stacks of high-index materials [70]. Low absorption is essential, and index dispersion can slightly shift band positions but is manageable within the narrow bandwidth of a photonic crystal.

Metals, with their negative dielectric permittivity, support surface plasmons that enable strong light confinement but also introduce absorption losses. Despite this limitation, metallic photonic crystals and plasmonic structures use periodic metal patterns to create bandgap-like effects and localized optical modes. Plasmonic photonic crystals, such as metal nanoparticle arrays or perforated metal films, exhibit surface plasmon resonances that filter and localize light. Though they lack a full photonic bandgap, they sustain plasmonic stop bands for surface waves, including spoof plasmons at microwave frequencies [71].

Hybrid dielectric–plasmonic systems combine metals with photonic crystals to enhance or tune light confinement [72]. Examples include metal-coated cavities for tighter mode localization, silicon–ITO slabs with electrically tunable resonances, and metal-filled fibers for plasmonic sensing. At lower frequencies, metals behave as near-perfect conductors, allowing all-metal photonic crystals to form high-reflectivity band structures for microwaves and terahertz waves. These structures are used in plasmonic biosensors, where Tamm plasmon modes provide sharp, index-sensitive resonances, and in thermophotonic systems like tungsten PhCs that emit narrowband IR radiation matched to photovoltaic bandgaps. Although metallic PhCs suffer from losses, their strong field confinement makes them valuable for filters, sensors, and THz applications.

1.7.2 Natural Photonic Crystals

Nature has evolved nanostructures that manipulate light to produce vivid structural colors [73]. Morpho butterfly wings (Figure 1.10), for example, use a “Christmas tree” chitin lattice acting as a photonic crystal slab to generate iridescent blue, while some beetles have 3D chitin-air lattices producing metallic greens. Slight disorder in these structures broadens reflection, making colors visible from multiple angles.

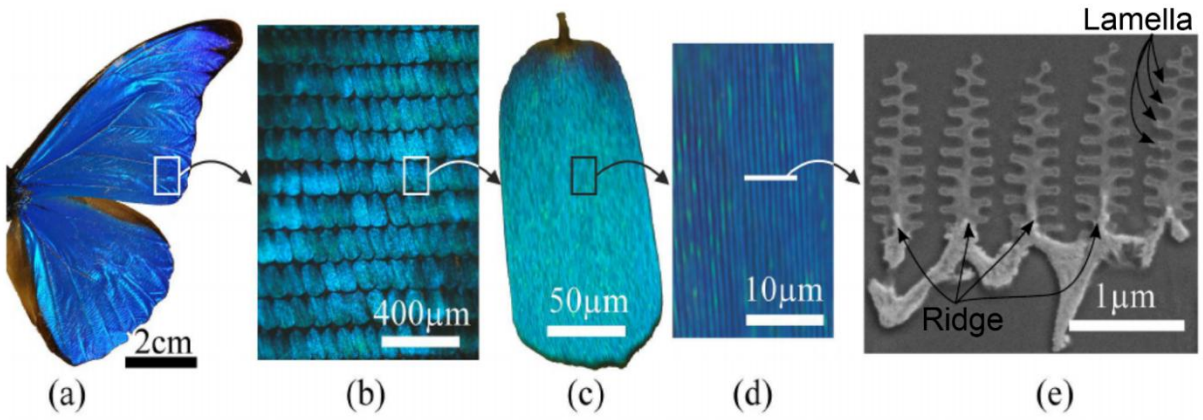

Figure 1.10: Zooming into the structural patterns of the Morpho rhetenor buttery: from the whole wing into the Christmas tree like nanostructure inside the scales. a) Photo of a Morpho rhetenor buttery wing. b) Photo of the blue scales which are arranged like shingles on a roof. c) A single scale has a typical width and length of 80 μm and 200 μm, respectively. d) The optical microscopy image shows the quasi-periodic structure of the ridges. e) The SEM image of the cross-section of the ridges reveals the Christmas tree like nanostructure which forms a multilayer stack of air and chitin [74].

Opals and pearls are natural colloidal photonic crystals; silica spheres in an fcc lattice produce iridescence via Bragg diffraction, while imperfect ordering and modest index contrast still enable strong color effects. Marine animals and scarab beetles exhibit helicoidal, lamellar, or diamond-like photonic structures, reflecting circularly polarized light or specific spectral bands. Peacock feathers show quasi-hexagonal lattices of melanin rods in keratin, creating iridescent blues and greens [75]. These natural photonic crystals inspire biomimetic designs, demonstrating strategies like hierarchical, multi-scale structures that diffuse light for broad-angle visibility. Combining structural color with pigments, such as blue plus yellow for green, further enhances color intensity and stability, showing how nature balances optical effects with practical functionality.

1.8 Optical Properties and Control of Light in Photonic Crystals

1.8.1 Light Propagation, Diffraction, and Waveguiding

Photonic crystals can control light propagation through Bragg diffraction and band dispersion, causing interference effects that shape the flow of light. At certain wavelengths, Bragg scattering produces stop bands that block propagation, while partial gaps can create high reflectivity in specific directions [76][77]. Their direction-dependent dispersion enables phenomena like self-collimation, where beams travel along fixed paths, and superprism effects, where small frequency shifts cause large beam deflections. In some bands near dispersion crossings, photonic crystals even exhibit negative refraction, behaving like a medium with an effective negative index. By providing

reciprocal lattice vectors, photonic crystals allow phase-matching for wave components unavailable in homogeneous media. This capability enables compact devices that bend, split, or focus light, including slabs demonstrating negative refraction and photonic crystal waveguides with highly controlled light routing.

Photonic crystals enable waveguides that differ fundamentally from conventional TIR designs, particularly in fibers and slabs. In PCFs, air-hole patterns form a 2D photonic crystal cladding around a solid or hollow core. Index-guiding PCFs use a solid, higher-index core to support only the fundamental mode and enable large mode areas, while photonic bandgap fibers confine light in a hollow core for low-loss guidance and high-power pulses. PCFs also allow precise dispersion control through adjustments of hole size, spacing, and core dimensions, enabling soliton propagation and supercontinuum generation [78][79].

Photonic crystal slab waveguides are formed by line defects in a 2D photonic crystal slab, confining light within the defect since frequencies in the bandgap cannot escape [80]. They offer tight mode confinement, strong dispersion control, and slow-light propagation, enhancing light–matter interactions but increasing sensitivity to scattering. These waveguides can bend sharply with minimal loss, enabling compact on-chip routing, and can act as wavelength splitters or couple to adjacent cavities for narrowband filtering and low-threshold lasing [81]. Fabrication imperfections, especially near slow-light regimes, cause backscattering and higher loss compared to ridge waveguides, motivating smoothing techniques like annealing [82]. Despite these challenges, photonic crystal waveguides provide unique capabilities, including extreme bending, engineered dispersion, and enhanced nonlinear interactions via integrated cavities.

1.8.2 Defects and Localized Modes

Introducing defects in a photonic crystal breaks its periodicity, creating localized modes within the bandgap that trap light. These are analogous to impurities in semiconductors, which produce localized electron states. Point defects, such as a missing or enlarged hole, form nanocavities with tiny mode volumes and high quality factors [83]. For example, H1 or L3 cavities in silicon slabs can achieve Q values from 10^5 up to 10^7, enabling strong light–matter interactions, ultra-low threshold nanolasers, single-photon sources, and sensitive refractive index sensors.

Line defects act as waveguides, and when terminated or perturbed, they form finite-length resonators, similar to Fabry–Pérot cavities but with Bragg mirrors [84]. In 3D crystals, planar defects can produce modes localized in one dimension, forming mirror-like cavities or waveguide layers. Because these defect modes lie within the bandgap, they are highly confined, though

fabrication imperfections can slightly reduce their Q [85]. Defect modes are crucial for functional devices. Embedding gain materials allows the creation of nanolasers, coupling cavities to waveguides enables add-drop filters, and high-Q cavities enhance nonlinear optical effects. Arrays of coupled cavities can also form slow-light waveguides, supporting delay lines and enhanced nonlinear phase control.

1.8.3 Dispersion and Slow-Light Effects

Photonic crystals provide precise control over light dispersion, enabling slow light, fast light, and unusual propagation effects not possible in bulk materials [86]. Near flat regions of the band structure, group velocities can drop to c/100–c/300, enhancing nonlinear interactions, optical gain, and phase shifts, which allows compact devices like modulators and optical buffers. Ultra-slow light is highly sensitive to disorder, so moderately slow light is often preferred to balance enhancement and loss.

These structures also allow advanced dispersion engineering, producing near-zero group velocity dispersion for low-distortion pulse transmission or high dispersion for pulse compression and phase matching. Photonic crystal fibers exploit this to generate broadband supercontinuum light, while waveguides can be tailored for flat or highly nonlinear dispersion [87]. Effects like the superprism, where small wavelength changes cause large angular deviations, highlight the strong control over light achievable in photonic crystals. Slow-light waveguides combined with refractive index tuning can temporarily halt light for optical buffering, although losses limit long-term storage. By carefully designing the band structure, photonic crystals can achieve negative refraction, enhanced light–matter interactions, supercontinuum generation, low-threshold lasing, sensing, and dispersive photonic components, highlighting the versatility of dispersion engineering in nanophotonics.

1.9 Applications of Photonic Crystals

Photonic crystals have moved from theoretical curiosities to enabling a variety of applications. A few major areas are highlighted in this section.

1.9.1 Photonic Crystal Sensors

Optical sensors based on photonic crystals exploit the strong sensitivity of resonant modes to local perturbations, such as changes in refractive index, molecular binding events, or surface adsorption. In a photonic crystal slab, a small modification of the dielectric environment, for example by introduction of an analyte or a bio-receptor layer, alters the resonance wavelength and modifies the quality factor of the supported modes. The periodic structure provides field confinement, slow-light

enhancement or guided mode resonance, thereby amplifying the interaction between light and the analyte. Such sensors offer label-free operation, high surface-to-volume overlap, and potential for compact integration in fluidic or lab-on-chip platforms. The sensitivity, detection limit and figure of merit (FOM) of a photonic crystal sensor are therefore strongly influenced by the modal confinement, the quality factor of the resonance, and the strength of the evanescent or near-field extension into the analyte region.

Within this field, sensors based on BICs in photonic crystal slabs have emerged as a particularly promising field , and indeed it is the main contribution focus of this thesis. BIC-based photonic crystal sensors employ resonances that are ideally decoupled from the radiation continuum, thereby attaining ultra-high quality factors and sharp spectral features, which in turn enhance refractive index sensitivity and reduce the resonant linewidth. The result is a significantly improved FOM compared with conventional guided-resonance or defect-cavity sensors. BIC-based sensing platforms have attracted growing attention in recent years for their exceptional sensitivity. In a study by Romano et al., label-free detection of the p53–MDM2 interaction was demonstrated using a BIC-supporting photonic crystal, achieving a detection limit of approximately 66 nM [88]. In subsequent research, Romano group developed all-dielectric metasurfaces sustaining high-Q BIC modes for ultrasensitive biodetection, reaching bulk sensitivity of 178 nm/RIU and enabling detection of ultra-low weight molecules [89]. In the thesis, the formation, dispersion engineering and device exploitation of BICs in photonic crystal slabs are analyzed in detail, with the aim of advancing the practical implementation of BIC-based sensors.

1.9.2 Photonic Crystal Fibers

Photonic crystals have revolutionized fiber optics through PCFs, which use a microstructured cladding of air holes instead of relying on total internal reflection. This design allows endlessly single-mode operation over a wide wavelength range, making PCFs ideal for large-mode-area high-power lasers and amplifiers. Hollow-core PCFs exploit photonic bandgaps to guide light through air, reducing loss and nonlinearity, achieving sub-1 dB/km attenuation, and enabling high-power pulse delivery and low-latency data links.

PCFs offer precise dispersion control by adjusting hole size, spacing, and core shape, enabling ultraflat or anomalous dispersion and shifting zero-dispersion wavelengths [90]. This capability has enabled supercontinuum generation for broadband spectroscopy and frequency combs. They also serve as sensitive sensors, with hollow or fluid-filled cores detecting refractive index changes over long interaction lengths. Strong confinement and tailored dispersion enhance nonlinear optical

effects, including four-wave mixing, Raman scattering, and supercontinuum generation. Integrating PCFs with nonlinear materials or semiconductors enables octave-spanning frequency combs and other advanced devices. These innovations demonstrate the practical impact of photonic crystals in fiber optics, from broadband sources to precision sensing and ultrashort-pulse delivery.

1.9.3 Photonic Crystal LEDs and Lasers

Photonic crystals have improved LEDs and lasers by enhancing light extraction, beam control, and mode confinement [91]. In high-index LEDs like GaN or GaAs, 2D photonic crystal patterns diffract trapped light, often doubling efficiency while enabling control over emission wavelength and direction [92]. In PhC surface-emitting lasers (PCSELs), 2D photonic crystals provide distributed feedback over a wide area, producing coherent high-power beams with customizable shapes, useful for LiDAR, projection, and beam steering. Defect cavities in photonic crystals create nanolasers with near-cubic-wavelength mode volumes and high Q factors, achieving near-thresholdless lasing and serving as sensitive sensors. Photonic crystals also enable precise mode control and beam shaping in broad-area lasers and QCLs, support multi-wavelength or dual-color emission, and allow mirrors with defects to lock lasers to specific frequencies for stable single-mode operation.

1.9.4 Photovoltaics and Energy Applications

Photonic crystals enhance solar devices by improving light management and spectral control [93]. Surface or back-layer patterns trap light, increasing internal reflections and boosting absorption, especially near the bandgap. In thin silicon cells, 2D photonic crystal back reflectors improve infrared response, while spectral splitting directs specific wavelengths to subcells. Slow-light effects further extend optical paths, enhancing thin-film efficiency.

Angle-selective photonic crystals facilitate radiative cooling by allowing sunlight to pass through while reflecting infrared radiation [94]. Photonic crystal lattices, whether dielectric or metallic, can be engineered to tailor emission in thermophotovoltaic systems, aligning it with bandgaps and minimizing sub-bandgap losses. Subwavelength moth-eye structures act as broadband anti-reflection coatings, simultaneously improving light trapping.

1.9.5 Emerging Applications

Photonic crystals enable advanced photonic applications by controlling light at the nanoscale. In quantum information, high-Q nanocavities with quantum dots produce on-demand single photons, while waveguides and topological PhCs allow robust, backscatter-immune photon routing and

strong light-matter coupling for quantum devices [95]. In integrated circuits, PhCs create compact filters, bends, and switches, with nanocavities enabling on-chip add-drop filtering and low-energy optical switching. Topological PhCs provide defect-immune waveguides and delay lines. PhCs also enhance nonlinear and ultrafast optics, supporting supercontinuum generation, low-energy optical switching, harmonic generation, and potentially integrated optical isolators, demonstrating their versatility for future quantum, photonic, and optical communication technologies [96].

1.10 References

[1] H.-X. Wang and J.-H. Jiang, "A Short Review of All-Dielectric Topological Photonic Crystals," *Front Phys*, vol. 10, Apr. 2022, doi: 10.3389/fphy.2022.866552.

[2] M. A. Butt, S. N. Khonina, and N. L. Kazanskiy, "Recent advances in photonic crystal optical devices: A review," *Opt Laser Technol*, vol. 142, p. 107265, Oct. 2021, doi: 10.1016/j.optlastec.2021.107265.

[3] E. Yablonovitch, "Inhibited Spontaneous Emission in Solid-State Physics and Electronics," *Phys Rev Lett*, vol. 58, no. 20, pp. 2059–2062, May 1987, doi: 10.1103/PhysRevLett.58.2059.

[4] S. John, "Strong localization of photons in certain disordered dielectric superlattices," *Phys Rev Lett*, vol. 58, no. 23, pp. 2486–2489, Jun. 1987, doi: 10.1103/PhysRevLett.58.2486.

[5] K. Sakoda, *Optical Properties of Photonic Crystals*, vol. 80. Berlin, Heidelberg: Springer Berlin Heidelberg, 2005. doi: 10.1007/b138376.

[6] K. M. Ho, C. T. Chan, and C. M. Soukoulis, "Existence of a photonic gap in periodic dielectric structures," *Phys Rev Lett*, vol. 65, no. 25, pp. 3152–3155, Dec. 1990, doi: 10.1103/PhysRevLett.65.3152.

[7] S.-Y. Lin, E. Chow, V. Hietala, P. R. Villeneuve, and J. D. Joannopoulos, "Experimental Demonstration of Guiding and Bending of Electromagnetic Waves in a Photonic Crystal," *Science (1979)*, vol. 282, no. 5387, pp. 274–276, Oct. 1998, doi: 10.1126/science.282.5387.274.

[8] P. Russell, "Photonic Crystal Fibers," *Science (1979)*, vol. 299, no. 5605, pp. 358–362, Jan. 2003, doi: 10.1126/science.1079280.

[9] W. Zhou and M. Pan, "The future of photonic crystal surface-emitting lasers," *Appl Phys Lett*, vol. 123, no. 14, Oct. 2023, doi: 10.1063/5.0172272.

[10] J. Du *et al.*, “Manipulation of unidirectional side scattering of light in transition metal dichalcogenide nanoresonators,” *Phys Rev B*, vol. 109, no. 11, p. 115426, Mar. 2024, doi: 10.1103/PhysRevB.109.115426.

[11] T. Lee and H. Iizuka, “Bragg scattering based acoustic topological transition controlled by local resonance,” *Phys Rev B*, vol. 99, no. 6, p. 064305, Feb. 2019, doi: 10.1103/PhysRevB.99.064305.

[12] M. Burresi *et al.*, “Magnetic Light-Matter Interactions in a Photonic Crystal Nanocavity,” *Phys Rev Lett*, vol. 105, no. 12, p. 123901, Sep. 2010, doi: 10.1103/PhysRevLett.105.123901.

[13] E. Yablonovitch, “Photonic Crystals,” *J Mod Opt*, vol. 41, no. 2, pp. 173–194, Feb. 1994, doi: 10.1080/09500349414550261.

[14] E. Yablonovitch and T. J. Gmitter, “Photonic band structure: The face-centered-cubic case,” *Phys Rev Lett*, vol. 63, no. 18, pp. 1950–1953, Oct. 1989, doi: 10.1103/PhysRevLett.63.1950.

[15] M. Bellingeri, A. Chiasera, I. Kriegel, and F. Scotognella, “Optical properties of periodic, quasi-periodic, and disordered one-dimensional photonic structures,” *Opt Mater (Amst)*, vol. 72, pp. 403–421, Oct. 2017, doi: 10.1016/j.optmat.2017.06.033.

[16] W. M. Robertson, G. Arjavalingam, R. D. Meade, K. D. Brommer, A. M. Rappe, and J. D. Joannopoulos, “Measurement of photonic band structure in a two-dimensional periodic dielectric array,” *Phys Rev Lett*, vol. 68, no. 13, pp. 2023–2026, Mar. 1992, doi: 10.1103/PhysRevLett.68.2023.

[17] J. D. Joannopoulos, S. G. Johnson, J. N. Winn, and R. D. Meade, *Photonic Crystals: Molding the Flow of Light (Second Edition)*, 2nd ed. Princeton University Press, 2008.

[18] R. K. Cersonsky, J. Antonaglia, B. D. Dice, and S. C. Glotzer, “The diversity of three-dimensional photonic crystals,” *Nat Commun*, vol. 12, no. 1, p. 2543, May 2021, doi: 10.1038/s41467-021-22809-6.

[19] A. El Mouncharih *et al.*, “One-dimensional photonic crystal-based biosensor for the detection of glucose concentration in human urine,” *J Nanophotonics*, vol. 17, no. 02, May 2023, doi: 10.1117/1.JNP.17.026007.

[20] F. Wu, Y. She, T. Zhou, Z. Cheng, and J. Huang, “Hybrid one-dimensional photonic crystals containing anisotropic metamaterials: Angle-driven photonic band gaps and angle-driven Tamm plasmon polaritons,” *Phys Rev A (Coll Park)*, vol. 110, no. 2, p. 023503, Aug. 2024, doi: 10.1103/PhysRevA.110.023503.

[21] M. Shaban, A. M. Ahmed, E. Abdel-Rahman, and H. Hamdy, “Tunability and Sensing Properties of Plasmonic/1D Photonic Crystal,” *Sci Rep*, vol. 7, no. 1, p. 41983, Feb. 2017, doi: 10.1038/srep41983.

[22] D. J. Rohrbach, E. C. Tracy, J. Walker, H. Baumann, and U. Sunar, “Blood flow dynamics during local photoreaction in a head and neck tumor model,” *Front Phys*, vol. 3, Mar. 2015, doi: 10.3389/fphy.2015.00013.

[23] Y. Akahane, T. Asano, B.-S. Song, and S. Noda, “High-Q photonic nanocavity in a two-dimensional photonic crystal,” *Nature*, vol. 425, no. 6961, pp. 944–947, Oct. 2003, doi: 10.1038/nature02063.

[24] B. Weng, J. Qiu, and Z. Shi, “Continuous-wave mid-infrared photonic crystal light emitters at room temperature,” *Applied Physics B*, vol. 123, no. 1, p. 29, Jan. 2017, doi: 10.1007/s00340-016-6622-6.

[25] E. Dulkeith, S. J. McNab, and Y. A. Vlasov, “Mapping the optical properties of slab-type two-dimensional photonic crystal waveguides,” *Phys Rev B*, vol. 72, no. 11, p. 115102, Sep. 2005, doi: 10.1103/PhysRevB.72.115102.

[26] G. J. Schneider, E. D. Wetzel, J. A. Murakowski, and D. W. Prather, “Fabrication of three-dimensional Yablonovite photonic crystals by multiple-exposure UV interference lithography,” E. G. Johnson, G. P. Nordin, and T. J. Suleski, Eds., Jan. 2005, p. 9. doi: 10.1117/12.591090.

[27] I. Sakellari *et al.*, “Direct laser writing of photonic nanostructures,” M. A. Noginov, N. I. Zheludev, A. D. Boardman, and N. Engheta, Eds., Aug. 2009, p. 73920Y. doi: 10.1117/12.825560.

[28] Y. Kang, J. Zhao, Y. Zeng, X. Du, and Z. Gu, “3D Printing Photonic Crystals: A Review,” *Small*, vol. 20, no. 46, Nov. 2024, doi: 10.1002/smll.202403525.

[29] L. C. Andreani and D. Gerace, “Photonic-crystal slabs with a triangular lattice of triangular holes investigated using a guided-mode expansion method,” *Phys Rev B*, vol. 73, no. 23, p. 235114, Jun. 2006, doi: 10.1103/PhysRevB.73.235114.

[30] P. Sivarajah, A. A. Maznev, B. K. Ofori-Okai, and K. A. Nelson, “What is the Brillouin zone of an anisotropic photonic crystal?,” *Phys Rev B*, vol. 93, no. 5, p. 054204, Feb. 2016, doi: 10.1103/PhysRevB.93.054204.

[31] T.-T. Wu, Z.-G. Huang, and S. Lin, “Surface and bulk acoustic waves in two-dimensional phononic crystal consisting of materials with general anisotropy,” *Phys Rev B*, vol. 69, no. 9, p. 094301, Mar. 2004, doi: 10.1103/PhysRevB.69.094301.

[32] T. Trifonov, L. F. Marsal, A. Rodríguez, J. Pallarès, and R. Alcubilla, “Effects of symmetry reduction in two-dimensional square and triangular lattices,” *Phys Rev B*, vol. 69, no. 23, p. 235112, Jun. 2004, doi: 10.1103/PhysRevB.69.235112.

[33] H. Buljan, M. Soljačić, T. Carmon, and M. Segev, “Cavity pattern formation with incoherent light,” *Phys Rev E*, vol. 68, no. 1, p. 016616, Jul. 2003, doi: 10.1103/PhysRevE.68.016616.

[34] D. Cheng, E. Lustig, K. Wang, and S. Fan, “Multi-dimensional band structure spectroscopy in the synthetic frequency dimension,” *Light Sci Appl*, vol. 12, no. 1, p. 158, Jun. 2023, doi: 10.1038/s41377-023-01196-1.

[35] C. Xu, G. Wang, Z. H. Hang, J. Luo, C. T. Chan, and Y. Lai, “Design of full-k-space flat bands in photonic crystals beyond the tight-binding picture,” *Sci Rep*, vol. 5, no. 1, p. 18181, Dec. 2015, doi: 10.1038/srep18181.

[36] G. V. Shadrina and E. N. Bulgakov, “Optical Bistability and Symmetry Breaking at Resonance Scattering of Light by a Finite Photonic Crystal with a Nonlinear Resonant Cavity,” *Journal of Experimental and Theoretical Physics*, vol. 135, no. 5, pp. 632–641, Nov. 2022, doi: 10.1134/S1063776122110176.

[37] M. Notomi, “Theory of light propagation in strongly modulated photonic crystals: Refractionlike behavior in the vicinity of the photonic band gap,” *Phys Rev B*, vol. 62, no. 16, pp. 10696–10705, Oct. 2000, doi: 10.1103/PhysRevB.62.10696.

[38] O. D. H. Pardo and R. R. Rey-González, “Photonic band gap atlas, formula extension, and design applications in 1D photonic crystals,” *Photonics Nanostruct*, vol. 63, p. 101355, Feb. 2025, doi: 10.1016/j.photonics.2025.101355.

[39] S. Slama, C. von Cube, M. Kohler, C. Zimmermann, and Ph. W. Courteille, “Multiple reflections and diffuse scattering in Bragg scattering at optical lattices,” *Phys Rev A (Coll Park)*, vol. 73, no. 2, p. 023424, Feb. 2006, doi: 10.1103/PhysRevA.73.023424.

[40] A. Della Villa, S. Enoch, G. Tayeb, V. Pierro, V. Galdi, and F. Capolino, “Band Gap Formation and Multiple Scattering in Photonic Quasicrystals with a Penrose-Type Lattice,” *Phys Rev Lett*, vol. 94, no. 18, p. 183903, May 2005, doi: 10.1103/PhysRevLett.94.183903.

[41] A. Kress *et al.*, “Manipulation of the spontaneous emission dynamics of quantum dots in two-dimensional photonic crystals,” *Phys Rev B*, vol. 71, no. 24, p. 241304, Jun. 2005, doi: 10.1103/PhysRevB.71.241304.

[42] M. Pelton *et al.*, “Efficient Source of Single Photons: A Single Quantum Dot in a Micropost Microcavity,” *Phys Rev Lett*, vol. 89, no. 23, p. 233602, Nov. 2002, doi: 10.1103/PhysRevLett.89.233602.

[43] P. St. J. Russell, S. Tredwell, and P. J. Roberts, “Full photonic bandgaps and spontaneous emission control in 1D multilayer dielectric structures,” *Opt Commun*, vol. 160, no. 1–3, pp. 66–71, Feb. 1999, doi: 10.1016/S0030-4018(98)00659-2.

[44] E. Istrate and E. H. Sargent, “Photonic crystal heterostructures and interfaces,” *Rev Mod Phys*, vol. 78, no. 2, pp. 455–481, May 2006, doi: 10.1103/RevModPhys.78.455.

[45] H. Zheng and S. Ravaine, “Bottom-Up Assembly and Applications of Photonic Materials,” *Crystals (Basel)*, vol. 6, no. 5, p. 54, May 2016, doi: 10.3390/cryst6050054.

[46] S. Li, H. Lin, F. Meng, D. Moss, X. Huang, and B. Jia, “On-Demand Design of Tunable Complete Photonic Band Gaps based on Bloch Mode Analysis,” *Sci Rep*, vol. 8, no. 1, p. 14283, Sep. 2018, doi: 10.1038/s41598-018-32422-1.

[47] H. Men, N. C. Nguyen, R. M. Freund, K. M. Lim, P. A. Parrilo, and J. Peraire, “Design of photonic crystals with multiple and combined band gaps,” *Phys Rev E*, vol. 83, no. 4, p. 046703, Apr. 2011, doi: 10.1103/PhysRevE.83.046703.

[48] A. Itin, “Geometric approach to design of photonic crystals and metamaterials via optimal toric packings,” *Phys Rev B*, vol. 111, no. 12, p. L121404, Mar. 2025, doi: 10.1103/PhysRevB.111.L121404.

[49] D. Wan and S. C. Glotzer, “Unexpected Dependence of Photonic Band Gap Size on Randomness in Self-Assembled Colloidal Crystals,” *Phys Rev Lett*, vol. 126, no. 20, p. 208002, May 2021, doi: 10.1103/PhysRevLett.126.208002.

[50] R. Ohnuki, Y. Kobayashi, and S. Yoshioka, “Polarization-dependent reflection of I-WP minimal-surface-based photonic crystal,” *Phys Rev E*, vol. 106, no. 1, p. 014123, Jul. 2022, doi: 10.1103/PhysRevE.106.014123.

[51] G. Ren, P. Shum, J. Hu, X. Yu, and Y. Gong, “Polarization-Dependent Bandgap Splitting and Mode Guiding in Liquid Crystal Photonic Bandgap Fibers,” *Journal of Lightwave Technology*, vol. 26, no. 22, pp. 3650–3659, Nov. 2008, doi: 10.1109/JLT.2008.920125.

[52] Ch. Schuller, J. P. Reithmaier, J. Zimmermann, M. Kamp, A. Forchel, and S. Anand, “Polarization-dependent optical properties of planar photonic crystals infiltrated with liquid crystals,” *Appl Phys Lett*, vol. 87, no. 12, Sep. 2005, doi: 10.1063/1.2053353.

[53] A. Raman and S. Fan, “Photonic Band Structure of Dispersive Metamaterials Formulated as a Hermitian Eigenvalue Problem,” *Phys Rev Lett*, vol. 104, no. 8, p. 087401, Feb. 2010, doi: 10.1103/PhysRevLett.104.087401.

[54] D. C. Dobson, J. Gopalakrishnan, and J. E. Pasciak, “An Efficient Method for Band Structure Calculations in 3D Photonic Crystals,” *J Comput Phys*, vol. 161, no. 2, pp. 668–679, Jul. 2000, doi: 10.1006/jcph.2000.6521.

[55] A. Cerjan *et al.*, “Observation of bound states in the continuum embedded in symmetry bandgaps,” *Sci Adv*, vol. 7, no. 52, Dec. 2021, doi: 10.1126/sciadv.abk1117.

[56] B. Zhen, C. W. Hsu, L. Lu, A. D. Stone, and M. Soljačić, “Explaining zero-linewidth resonances by their topological nature,” *SPIE Newsroom*, Mar. 2015, doi: 10.1117/2.1201502.005804.

[57] N. D. Le *et al.*, “Super Bound States in the Continuum on a Photonic Flatband: Concept, Experimental Realization, and Optical Trapping Demonstration,” *Phys Rev Lett*, vol. 132, no. 17, p. 173802, Apr. 2024, doi: 10.1103/PhysRevLett.132.173802.

[58] R.-L. Chern, J.-C. Chang, and H.-C. Yang, “Bound states in the continuum in anisotropic photonic crystal slabs,” *Sci Rep*, vol. 13, no. 1, p. 14139, Aug. 2023, doi: 10.1038/s41598-023-40869-0.

[59] M. Kang, T. Liu, C. T. Chan, and M. Xiao, “Applications of bound states in the continuum in photonics,” *Nature Reviews Physics*, vol. 5, no. 11, pp. 659–678, Oct. 2023, doi: 10.1038/s42254-023-00642-8.

[60] D. C. Marinica, A. G. Borisov, and S. V. Shabanov, “Bound States in the Continuum in Photonics,” *Phys Rev Lett*, vol. 100, no. 18, p. 183902, May 2008, doi: 10.1103/PhysRevLett.100.183902.

[61] S. I. Azzam and A. V. Kildishev, “Photonic Bound States in the Continuum: From Basics to Applications,” *Adv Opt Mater*, vol. 9, no. 1, Jan. 2021, doi: 10.1002/adom.202001469.

[62] U. Biswas, C. Nayak, and J. K. Rakshit, “Fabrication techniques and applications of two-dimensional photonic crystal: history and the present status,” *Optical Engineering*, vol. 62, no. 01, Dec. 2022, doi: 10.1117/1.OE.62.1.010901.

[63] J. Li, J. Yan, L. Jiang, J. Yu, H. Guo, and L. Qu, “Nanoscale multi-beam lithography of photonic crystals with ultrafast laser,” *Light Sci Appl*, vol. 12, no. 1, p. 164, Jul. 2023, doi: 10.1038/s41377-023-01178-3.

[64] C. P. Reardon, I. H. Rey, K. Welna, L. O’Faolain, and T. F. Krauss, “Fabrication And Characterization Of Photonic Crystal Slow Light Waveguides And Cavities,” *Journal of Visualized Experiments*, no. 69, Nov. 2012, doi: 10.3791/50216.

[65] A. Hensley, W. M. Jacobs, and W. B. Rogers, “Self-assembly of photonic crystals by controlling the nucleation and growth of DNA-coated colloids,” *Proceedings of the National Academy of Sciences*, vol. 119, no. 1, Jan. 2022, doi: 10.1073/pnas.2114050118.

[66] J. Liu *et al.*, “Colloidal Photonic Crystals: Advanced Assembly Strategies and Frontier Optical Applications,” *Laser Photon Rev*, Oct. 2025, doi: 10.1002/lpor.202502259.

[67] M. Deubel, G. von Freymann, M. Wegener, S. Pereira, K. Busch, and C. M. Soukoulis, “Direct laser writing of three-dimensional photonic-crystal templates for

telecommunications," *Nat Mater*, vol. 3, no. 7, pp. 444–447, Jul. 2004, doi: 10.1038/nmat1155.

[68] Y. Hu *et al.*, "Toward Direct Laser Writing of Actively Tuneable 3D Photonic Crystals," *Adv Opt Mater*, vol. 5, no. 3, Feb. 2017, doi: 10.1002/adom.201600458.

[69] G. K. Johri, "The study of dielectric materials as photonic crystals based on the mechanism of photonic band gap," in *Proceedings of 2002 IEEE 14th International Conference on Dielectric Liquids. ICDL 2002 (Cat. No.02CH37319)*, IEEE, pp. 347–349. doi: 10.1109/ICDL.2002.1022765.

[70] Z. Geng *et al.*, "A Photonic crystal fiber with large effective refractive index separation and low dispersion," *PLoS One*, vol. 15, no. 5, p. e0232982, May 2020, doi: 10.1371/journal.pone.0232982.

[71] A. S. Hall *et al.*, "Broadband Light Absorption with Multiple Surface Plasmon Polariton Waves Excited at the Interface of a Metallic Grating and Photonic Crystal," *ACS Nano*, vol. 7, no. 6, pp. 4995–5007, Jun. 2013, doi: 10.1021/nn4003488.

[72] L. Hajshahvaladi, H. Kaatuzian, M. Moghaddasi, and M. Danaie, "Hybridization of surface plasmons and photonic crystal resonators for high-sensitivity and high-resolution sensing applications," *Sci Rep*, vol. 12, no. 1, p. 21292, Dec. 2022, doi: 10.1038/s41598-022-25980-y.

[73] J. P. Vigneron and P. Simonis, "Natural photonic crystals," *Physica B Condens Matter*, vol. 407, no. 20, pp. 4032–4036, Oct. 2012, doi: 10.1016/j.physb.2011.12.130.

[74] R. H. Siddique *et al.*, "Utilizing laser interference lithography to fabricate hierarchical optical active nanostructures inspired by the blue Morpho butterfly," R. Liang and J. A. Shaw, Eds., Sep. 2014, p. 91870E. doi: 10.1117/12.2066467.

[75] H. Chen, J. Wei, F. Pan, T. Yuan, Y. Fang, and Q. Wang, "Advances in Photonic Crystal Research for Structural Color," *Adv Mater Technol*, vol. 10, no. 4, Feb. 2025, doi: 10.1002/admt.202400865.

[76] W. L. Vos and H. M. van Driel, "Higher order Bragg diffraction by strongly photonic fcc crystals: onset of a photonic bandgap," *Phys Lett A*, vol. 272, no. 1–2, pp. 101–106, Jul. 2000, doi: 10.1016/S0375-9601(00)00388-1.

[77] I. I. Shishkin, M. V. Rybin, K. B. Samusev, V. G. Golubev, and M. F. Limonov, "Multiple Bragg diffraction in opal-based photonic crystals: Spectral and spatial dispersion," *Phys Rev B*, vol. 89, no. 3, p. 035124, Jan. 2014, doi: 10.1103/PhysRevB.89.035124.

[78] R. J. Noble, J. E. Spencer, and B. T. Kuhlmey, “Hollow-core photonic band gap fibers for particle acceleration,” *Physical Review Special Topics - Accelerators and Beams*, vol. 14, no. 12, p. 121303, Dec. 2011, doi: 10.1103/PhysRevSTAB.14.121303.

[79] Y. Zhu *et al.*, “Design of Multi-Core Hollow-Core Photonic Bandgap Fibers,” *Journal of Lightwave Technology*, vol. 43, no. 3, pp. 1364–1371, Feb. 2025, doi: 10.1109/JLT.2024.3485160.

[80] K. Asakawa, “Fabrication and characterization of photonic crystal slab waveguides and application to ultra-fast all-optical switching devices,” in *Proceedings of 2003 5th International Conference on Transparent Optical Networks, 2003.*, IEEE, pp. 193–197. doi: 10.1109/ICTON.2003.1264614.

[81] S. G. Johnson, P. R. Villeneuve, S. Fan, and J. D. Joannopoulos, “Linear waveguides in photonic-crystal slabs,” *Phys Rev B*, vol. 62, no. 12, pp. 8212–8222, Sep. 2000, doi: 10.1103/PhysRevB.62.8212.

[82] U. Huebner, R. Boucher, W. Morgenroth, M. Schmidt, and M. Eich, “Fabrication of photonic crystal structures in polymer waveguide material,” *Microelectron Eng*, vol. 83, no. 4–9, pp. 1138–1141, Apr. 2006, doi: 10.1016/j.mee.2006.01.028.

[83] S. Vaidya, W. A. Benalcazar, A. Cerjan, and M. C. Rechtsman, “Point-Defect-Localized Bound States in the Continuum in Photonic Crystals and Structured Fibers,” *Phys Rev Lett*, vol. 127, no. 2, p. 023605, Jul. 2021, doi: 10.1103/PhysRevLett.127.023605.

[84] M. K. Moghaddam and R. Fleury, “Slow light engineering in resonant photonic crystal line-defect waveguides,” *Opt Express*, vol. 27, no. 18, p. 26229, Sep. 2019, doi: 10.1364/OE.27.026229.

[85] T. Baba, D. Mori, K. Inoshita, and Y. Kuroki, “Light Localizations in Photonic Crystal Line Defect Waveguides,” *IEEE Journal of Selected Topics in Quantum Electronics*, vol. 10, no. 3, pp. 484–491, May 2004, doi: 10.1109/JSTQE.2004.829201.

[86] D. Rodriguez-Guillen, A. Díez, M. V. Andrés, and L. Velazquez-Ibarra, “Inverse design of photonic crystal fibers for dispersion engineering using neural networks,” *Opt Commun*, vol. 587, p. 131891, Aug. 2025, doi: 10.1016/j.optcom.2025.131891.

[87] D. W. Prather *et al.*, “Dispersion engineering of photonic crystals,” P. Lalanne, Ed., Dec. 2003, p. 30. doi: 10.1117/12.504651.

[88] S. Romano *et al.*, “Optical Biosensors Based on Photonic Crystals Supporting Bound States in the Continuum,” *Materials*, vol. 11, no. 4, p. 526, Mar. 2018, doi: 10.3390/ma11040526.

[89] S. Romano *et al.*, “Label-free sensing of ultralow-weight molecules with all-dielectric metasurfaces supporting bound states in the continuum,” *Photonics Res*, vol. 6, no. 7, p. 726, Jul. 2018, doi: 10.1364/PRJ.6.000726.

[90] J. Pniewski *et al.*, “Dispersion properties of all-solid photonic crystal fibers with nanostructured core,” K. Kalli and A. Mendez, Eds., Jun. 2012, p. 84261J. doi: 10.1117/12.922699.

[91] Dang Hoang Long, In-Kag Hwang, and Sang-Wan Ryu, “Design Optimization of Photonic Crystal Structure for Improved Light Extraction of GaN LED,” *IEEE Journal of Selected Topics in Quantum Electronics*, vol. 15, no. 4, pp. 1257–1263, Jul. 2009, doi: 10.1109/JSTQE.2009.2014471.

[92] C. Wiesmann, K. Bergenek, N. Linder, and U. T. Schwarz, “Photonic crystal LEDs – designing light extraction,” *Laser Photon Rev*, vol. 3, no. 3, pp. 262–286, Apr. 2009, doi: 10.1002/lpor.200810053.

[93] Ç. Çetinkaya *et al.*, “Highly improved light harvesting and photovoltaic performance in CdTe solar cell with functional designed 1D-photonic crystal via light management engineering,” *Sci Rep*, vol. 12, no. 1, p. 11245, Jul. 2022, doi: 10.1038/s41598-022-15078-w.

[94] J. Krügener *et al.*, “Photonic crystals for highly efficient silicon single junction solar cells,” *Solar Energy Materials and Solar Cells*, vol. 233, p. 111337, Dec. 2021, doi: 10.1016/j.solmat.2021.111337.

[95] S. Slussarenko and G. J. Pryde, “Photonic quantum information processing: A concise review,” *Appl Phys Rev*, vol. 6, no. 4, Dec. 2019, doi: 10.1063/1.5115814.

[96] D. Englund, I. Fushman, A. Faraon, B. Ellis, and J. Vučković, “Photonic crystal chips for optical communications and quantum information processing,” S. M. Weiss, G. S. Subramania, and F. García-Santamaría, Eds., Aug. 2008, p. 70310C. doi: 10.1117/12.796817.

Chapter 2: Optical Biosensors

2.1 Introduction to Optical Biosensors

Optical Label-free biosensors, which enable real-time kinetics measurement without label bias, detect changes in the optical properties of a sensing element and convert them into an optical signal proportional to the concentration of a biological analyte. The development of optical biosensing is driven by the need to identify trace amounts of biomolecules with high specificity, without using fluorescent or enzymatic labeling. Traditional assays often involve complicated sample preparation, limited sensitivity and long analysis times [1]. In contrast, label-free optical sensors monitor minute perturbations in the local refractive index or optical phase in real time, enabling direct measurement of biomolecular interactions while preserving biological function. These attributes make optical biosensors attractive for point-of-care diagnostics, environmental monitoring and pharmaceutical quality control.

Among optical techniques, it is worth mentioning surface plasmon resonance (SPR), microcavities, interferometers and photonic crystal sensors. The key advantage common to these approaches their ability to convert molecular binding events at the sensor surface into detectable optical signals without the need for external labels. This eliminates nonspecific interactions introduced by tags and enables real-time monitoring of binding kinetics[1]. Furthermore, integrated photonic sensors can be miniaturized using complementary metal-oxide-semiconductor (CMOS) technology, supporting multiplexed detection and the development of portable devices.

2.1.1 Motivation for biosensing

Target analytes such as small molecules, proteins and nucleic acids often appear in complex matrices at concentrations ranging from femtomolar to millimolar levels. Achieving adequate sensitivity while maintaining specificity against background interference is a central challenge. Optical biosensors overcome this limitation by detecting inherent refractive index or phase shifts that occur upon molecular binding, enabling label-free analysis. Moreover, biosensors must discriminate between structurally similar molecules, necessitating well-controlled surface chemistry to immobilize selective recognition elements while suppressing nonspecific adsorption. As the

following sections discuss, the sensitivity and specificity of optical biosensors depend on both the optical transduction mechanism and the surface functionalization strategy.

2.1.2 Advantages of optical biosensors for real-time, label-free detection

As already mentioned, label-free optical biosensors offer several advantages over traditional labelled assays. They enable real-time observation of binding kinetics, as the optical response occurs immediately with changes in surface mass density or refractive index. The absence of labels including fluorescent or enzymatic labels, also eliminates the need for lengthy sample preparation and avoids the perturbation of binding equilibria [1]. The optical detection methods can achieve remarkable sensitivity, with microcavity and interferometric sensors capable of resolving refractive index variations as small as 10^{-6} to 10^{-9} RIU [2]. These integrated photonic sensors leverage mature semiconductor fabrication to yield compact, low-cost devices capable of multiplexed detection on a single chip.

2.1.3 Scope of this chapter

This chapter examines the fundamental principles and performance characteristics of the main categories of label-free optical biosensors. Section 2 introduces the mechanisms of optical detection, the metrics used to characterize sensor performance, and the role of surface functionalization. Section 3 outlines the main types of sensors, including SPR devices, ring resonators, interferometers, and photonic crystal biosensors. Section 4 discusses functionalization strategies in optical biosensors, with a focus on Silane-PEG-COOH and APTES-based amine functionalization, along with related surface chemistries. Section 5 reviews the findings of selected studies that employed photonic crystal sensors.

2.2 Principles of Label-Free Optical Biosensing

Label-free optical biosensors rely on detecting perturbations in the optical properties of a waveguide, microcavity or nanostructure caused by biomolecule binding at the sensor surface [3]. A typical sensor comprises a transducer, in which light is confined and a biorecognition layer that selectively captures the target analyte. When binding occurs, the attached analytes modify the local refractive index, which in turn alters the propagation constant or resonance condition of the optical mode. The resulting shift in wavelength, phase, amplitude or intensity serves as the analytical signal [1]. Many optical biosensors operate by tracking changes in the effective refractive index n_{eff} of a guided mode [4]. The main categories of such biosensors and their operating principles will be discussed in detail in Section 2.3. As an example, Figure 2.1 depicts a representative waveguide

biosensor in which a guided optical mode interacts evanescently with an analyte layer on the sensor surface.

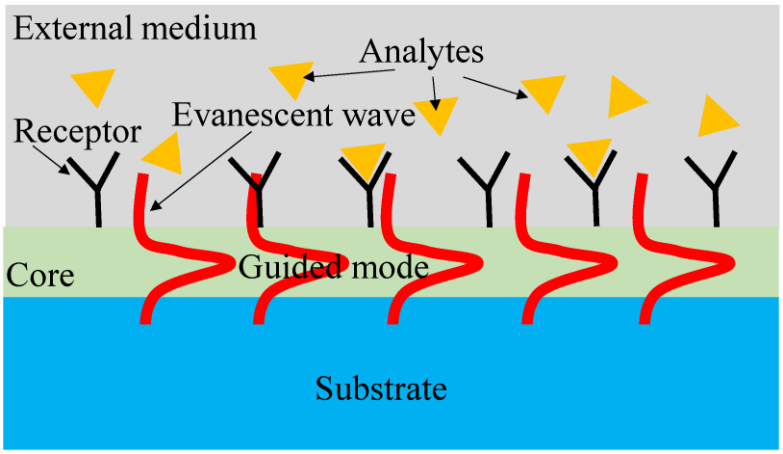

Figure 2.1: Schematic representation of a waveguide-based label-free optical biosensor. Light is confined within the waveguide, generating an evanescent field that extends into the external medium. When analyte molecules bind to receptors immobilized on the sensor surface, they interact with the evanescent wave, causing a change in the local refractive index. This perturbation modifies the guided optical mode, producing a measurable shift in the sensor optical signal [5].

2.2.1 Key performance metrics

The performance of an optical biosensor is characterized by its sensitivity (S), limit of detection (LOD) and selectivity. Sensitivity measures the sensor response to a change in refractive index or analyte concentration and is commonly reported as the wavelength/phase shift per refractive index unit (RIU) or per concentration unit (e.g., M). For resonant sensors, the sensitivity is proportional to the confinement of the evanescent field in the analyte region. The LOD is defined as the smallest analyte concentration that produces a signal distinguishable from noise. The limit of detection can be estimated as $\mathrm{LOD} = \frac{3\sigma}{S}$, where σ is the standard deviation of the blank signal (noise) and S is the sensitivity of the sensor. Selectivity depends on the specificity and binding affinity of the biorecognition element; nonspecific binding must be minimized through appropriate surface chemistry [6][7].

2.2.2 Role of surface functionalization in biological recognition

The selective capture of analytes depends on immobilizing biorecognition molecules, such as antibodies, aptamers, peptides, or enzymes, onto the sensor surface while retaining their functional activity. Surface functionalization must provide reactive sites for covalent attachment, minimize nonspecific adsorption, and preserve the optical properties of the transducer [8][9]. For example,

Silane chemistry provides a versatile method to functionalize silica and silicon nitride surfaces, which can be hydroxylated using oxygen plasma to generate reactive -OH groups. After hydroxylation, poly(ethylene glycol) (PEG)-silanes can be applied to introduce carboxyl groups, which can then be activated via 1-ethyl-3-(3-dimethylaminopropyl)carbodiimide/N-hydroxysuccinimide (EDC/NHS) chemistry to covalently bind amine-terminated ligands. In contrast, 3-aminopropyltriethoxysilane (APTES) produces amine-terminated surfaces that enable covalent immobilization of biomolecules through EDC/NHS-mediated activation of their carboxyl groups, allowing amide bond formation between the ligand and the surface [10][11]. The choice of functionalization approach directly affects the sensitivity, stability, and reusability of optical biosensors and will be explored further in Section 4.

2.3 Types of Optical Biosensors

The diversity of optical biosensor platforms reflects the many ways in which light can interact with matter [12]. Several optical biosensor nanotechnologies, either based on nanoplasmonics (such as SPR biosensors) or silicon nanophotonics (such as ring resonators, interferometers and photonic crystals), have been developed and even commercialized. These sensors all rely on the same physical working mechanism, the evanescent field sensing principle. Figure 2.2 presents an overview of the main biosensor classes discussed in the following and illustrates how they fit within the broader category of optical biosensors.

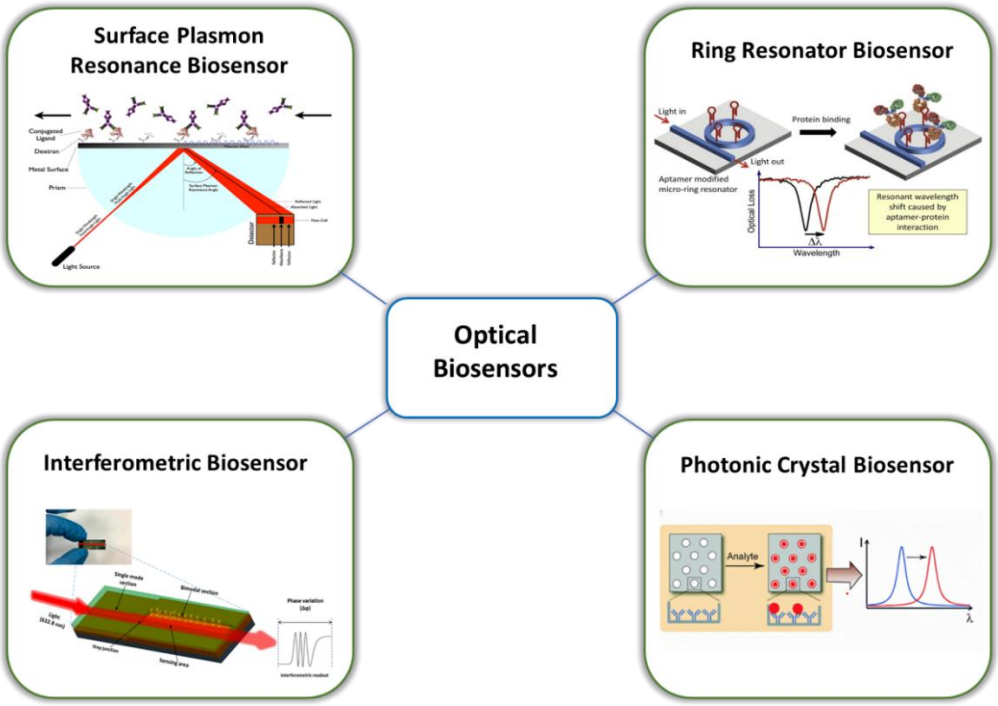

Figure 2.2: Classification of optical biosensors, including Surface Plasmon Resonance biosensors, Ring Resonator biosensors, Interferometric biosensors, and Photonic Crystal biosensors.

2.3.1 Surface Plasmon Resonance sensors

Surface Plasmon Resonance sensors exploit the interaction between incident photons and free electrons at a metal-dielectric interface to monitor refractive index changes near the sensor surface [13]. When light is incident on a thin metallic layer (typically gold) at a specific angle of incidence, a portion of the light couples to collective oscillations of free electrons, known as surface plasmons. These surface plasmons propagate along the metal surface, generating an evanescent electromagnetic field that extends approximately 300 nm into the adjacent dielectric medium [14].

For efficient excitation of surface plasmons, the component of the light wavevector parallel to the interface must match the propagation constant of the surface plasmon [15]. This momentum-matching condition can be achieved through coupling mechanisms such as attenuated total reflection or diffraction, implemented using coupling devices like prism, waveguide, or grating couplers. Among these, the prism coupler in the Kretschmann configuration is the most widely used. In this setup, a light beam passes through a high-refractive-index prism and undergoes total internal reflection at the prism-metal interface, producing an evanescent wave that penetrates the thin metal layer. The propagation constant of this evanescent wave, given by

$$k = \frac{2\pi}{\lambda} n_p \sin\theta \tag{2-1}$$

where n_p is the refractive index of the prism and θ is the incidence angle. Once the coupling condition is satisfied, energy is efficiently transferred from the light wave to the surface plasmons, resulting in a characteristic drop in the intensity of the reflected light. The resonance condition is extremely sensitive to the refractive index of the medium adjacent to the metal film [16][15]. Thus, when biomolecular interactions such as antigen-antibody binding or DNA hybridization occur on the functionalized surface, they alter the local refractive index. This change shifts the resonance condition, which can be detected by monitoring variations in the reflected light intensity or by tracking shifts in the resonance angle or wavelength. Figure 2.3 illustrates a schematic representation of a conventional SPR biosensor, where analyte binding to the functionalized surface leads to a measurable shift in the resonance angle.

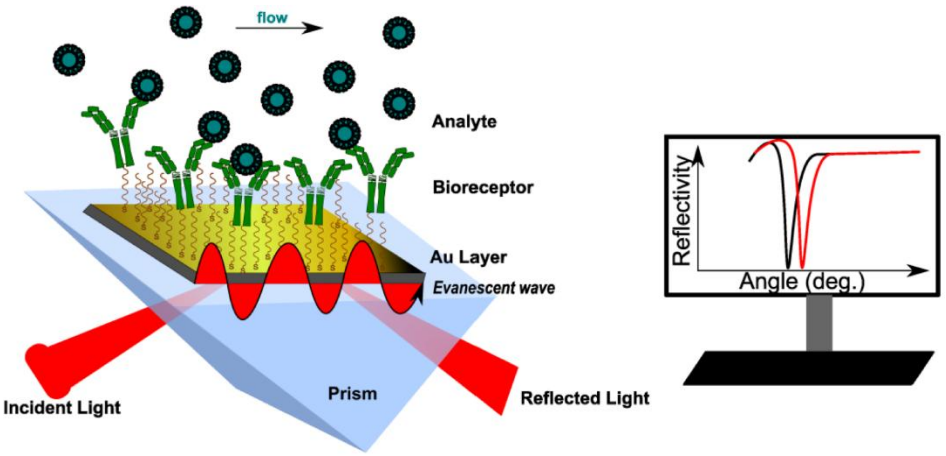

Figure 2.3: Schematic presentation of conventional SPR biosensor. The analyte binding to the immobilized bioreceptor causes a change in RI near the surface, recorded as the shift of the resonance angle [17].

Depending on which optical parameter is measured, SPR sensors can be classified as angular, wavelength, intensity, or phase-modulated devices [18]. The detection limit of these SPR biosensors is in the range of 10^{-5}-10^{-6} RIU [19]. Their high sensitivity, label-free operation, and real-time monitoring capability make them among the most robust and widely employed optical biosensors in biomedical research, drug discovery, and environmental monitoring. Importantly, recent advances in SPR technology have focused on integrated and multi-channel architectures to improve multiplexing capability and miniaturization [20].

2.3.2 Ring resonator sensors

A ring resonator sensor is an integrated optical device that operates on the principle of light resonance within a circular waveguide structure [21]. Typically, it consists of a high-refractive-index ring waveguide (often made of materials such as silicon) that is coupled to a straight bus waveguide. When light is coupled from the bus waveguide into the ring, it propagates around the loop in the form of whispering gallery modes (WGMs), which arise from multiple total internal reflections along the curved surface. Constructive interference occurs when the optical path length supports an integer multiple of the wavelength, leading to strong field enhancement at specific resonance wavelengths.

The resonance condition of a ring resonator is given by:

$$\lambda_{\text{res}} = \frac{2\pi n_{\text{eff}} r}{m}, \tag{2-2}$$

where m is an integer describing the WGM angular momentum, r is the ring radius, and n_{eff} is the effective refractive index experienced by the WGM. Any perturbation in the refractive index of the surrounding environment, such as that caused by biomolecular binding on the functionalized ring surface, alters n_{eff}, resulting in a measurable resonance wavelength shift. This shift can be monitored by scanning the wavelength or by tracking the intensity variation at a fixed wavelength. Figure 2.4 shows a schematic of a ring resonator coupled to a straight bus waveguide. When a biomolecule binds to the functionalized ring surface, the evanescent field detects the resulting refractive index change, producing a measurable resonance shift [22].

Unlike straight waveguides, where the light-matter interaction is limited by the waveguide length, the ring geometry allows the circulating light to interact repeatedly with surface-bound analytes, effectively increasing the optical path length. This enhancement is quantified by the quality factor (Q factor), which relates to the effective optical path length as

$$L_{eff} = \frac{Q\lambda}{2\pi n}, \tag{2-3}$$

where n is the refractive index of the resonator. High Q factors correspond to low optical losses and long photon lifetimes, producing narrow resonance linewidths and high peak resolution, key features that directly translate into high sensitivity [23]. In practice, Q factors up to 10^6 can be achieved in ring resonators with diameters of only a few tens of micrometers (typically 50-200 μm), corresponding to effective path lengths equivalent to several centimeters in straight waveguides.

Ring resonator sensors are particularly attractive for biosensing applications [24]. The evanescent field of the WGM interacts with analytes on the resonator surface, allowing the detection of refractive index changes as small as 10^{-7} RIU. Ring resonators integrated with microfluidic systems have been successfully used to detect proteins such as human serum albumin and arrays of ring resonators can also be multiplexed for the simultaneous detection of multiple analytes, making them highly suitable for high-throughput diagnostic applications [25]. Despite their advantages, RR sensors face challenges related to scattering losses, fabrication imperfections, and temperature sensitivity, which can obscure subtle resonance shifts. Nevertheless, ongoing advances in material engineering, temperature compensation, and on-chip integration continue to expand the performance and versatility of ring resonator biosensors for biomedical, environmental, and chemical sensing applications [26].

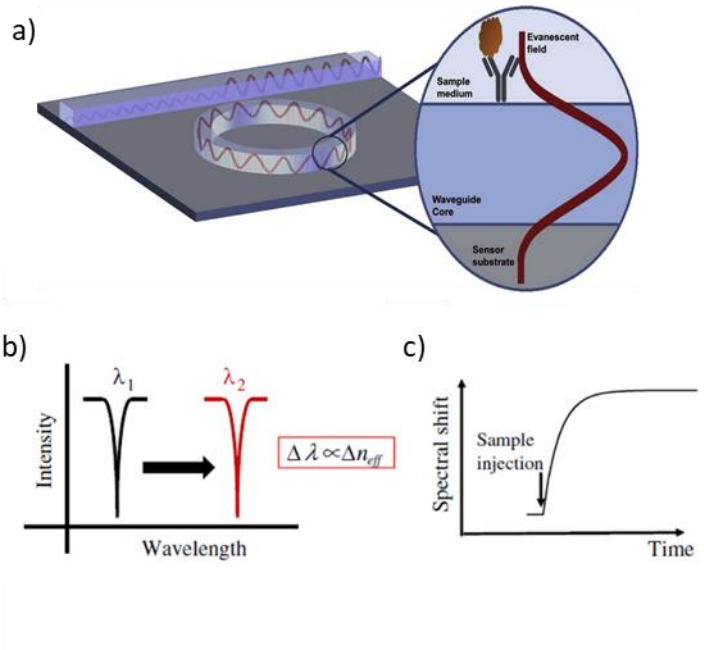

Figure 2.4: Working principle of a ring resonator biosensor: a) Schematic illustration of a ring resonator biosensor (The zoomed-in section shows the evanescent field extending from the waveguide core into the sample medium, allowing for interaction with biomolecules), b) The resonant mode undergoes a shift in response to the local refractive index variation caused by molecular binding, c) The corresponding signal is obtained by tracking the spectral shift in real time [27][28].

2.3.3 Interferometric sensors

Interferometric biosensors detect variations in the refractive index by measuring phase differences between two optical paths or modes. In these sensors, an interference pattern is generated when two or more light waves propagating through separate optical paths are recombined [29]. The different propagation velocities of the light waves, arising from the interaction of their evanescent fields with the surrounding medium, result in a measurable phase shift. This phase variation correlates with biochemical interactions occurring near the sensor surface or with bulk refractive index changes in flowing solutions.

Among the various interferometric configurations, Mach-Zehnder interferometers (MZI) [30], Young interferometers (YI), and dual-polarization interferometers (DPI) are the most commonly used in integrated waveguide biosensing. In an integrated MZI configuration, light from an input single-mode waveguide is split into two arms (a sensing arm and a reference arm) using a Y-junction [30]. After propagating through a certain distance, the two beams are recombined in an output waveguide to produce an interference signal. The sensing arm is partially exposed to the external medium, where biological interactions occur. When a biomolecule binds to the functionalized surface or when analyte concentration changes, the resulting variation in the local

refractive index alters the effective refractive index of the sensing arm, inducing a phase difference upon recombination [31]. Figure 2.5 provides a schematic overview of the working principle of an interferometric biosensor, highlighting the reference and sensing arms, the interaction of analytes with the sensing surface, and the resulting interference signal that is measured at the detector [2].

The phase difference ($\Delta\phi$) can be expressed as:

$$\Delta\phi = \frac{2\pi L}{\lambda}(N_S - N_R), \tag{2-4}$$

and the total output intensity (I_T) as:

$$I_T = I_S + I_R + 2\sqrt{I_S I_R}\cos\big(\Delta\Phi(t)\big), \tag{2-5}$$

where N_S and N_R are the effective refractive indices of the sensing and reference arms, L is the optical path length, and λ is the wavelength of light.

By demodulating this phase difference, the interferometer quantifies minute changes in the refractive index of the sensing medium, enabling highly sensitive, label-free detection of biomolecular interactions. An inherent advantage of the MZI design is its use of an internal reference arm, which compensates for environmental disturbances such as temperature fluctuations or nonspecific adsorption, thereby enhancing measurement stability and reliability.

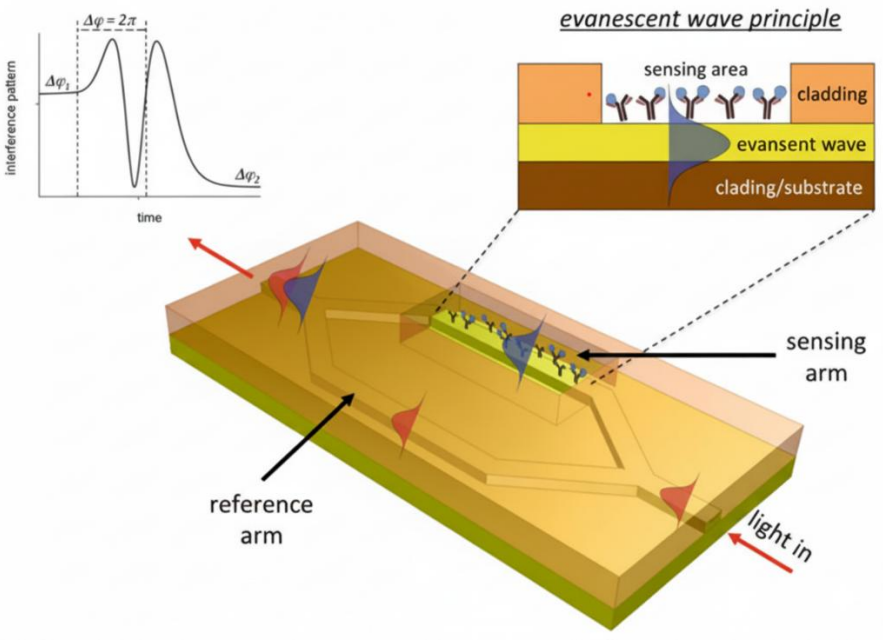

Figure 2.5: Scheme of the working principle of an interferometric biosensor. Light entering the device is split into a reference arm and a sensing arm. Biomolecular binding on the functionalized sensing area alters the local refractive index, causing a measurable phase shift (Δϕ) in the sensing arm, which leads to changes in the interference pattern upon recombination. The upper inset further illustrates the evanescent wave principle, showing the evanescent field extending from the waveguide core to interact with biomolecules immobilized on the surface of the sensing area [32].

2.3.4 Photonic crystal sensors

As already mentioned in Chapter 1, photonic crystals are nanostructured media that exhibit periodic modulation of the refractive index, allowing precise control over the propagation of light. Similar to the way that semiconductors regulate the flow of electrons, photonic crystals control the movement of photons through their periodic dielectric structure. This periodic arrangement gives rise to a photonic bandgap, a range of frequencies where light cannot propagate due to destructive interference between incident and reflected waves at the dielectric interfaces [33]. This unique property enables the manipulation of light within photonic crystals, allowing functionalities such as optical filtering, waveguiding, light confinement, and slow-light propagation, which are essential for high-performance photonic and sensing applications [34].

In biosensing, photonic crystal structures have been widely used as label-free sensors for detecting biomolecular interactions. Their operating principle is based on monitoring refractive index variations induced by the adsorption of biomolecules onto a functionalized surface. These RI changes shift the resonance wavelength of the photonic mode confined within the crystal. Because PhC devices exhibit narrow spectral linewidths, even small wavelength shifts can be resolved, enabling detection of analytes at very low concentrations or biomolecules with low molecular weight, such as small-molecule drug compounds. Furthermore, PhC biosensors allow real-time analysis of binding kinetics and affinities without the need for labeling, making them powerful tools for molecular diagnostics and interaction studies [33]. A simple schematic of biosensing using photonic crystals is illustrated in Figure 2.6.

As discussed in Chapter 1, Bound States in the Continuum are exceptional optical modes that remain perfectly confined within the radiation continuum, achieving theoretically infinite quality factors. Unlike conventional resonances that radiate energy, BICs suppress radiative losses through mechanisms such as symmetry protection or destructive interference. This leads to highly localized electromagnetic fields that significantly enhance light–matter interactions within the sensing region. Recent developments have extended the concept of BICs to photonic crystal platforms, offering a new approach to light confinement beyond traditional photonic bandgap designs [34].

The incorporation of high-Q BIC resonances in photonic crystal metasurfaces significantly improves biosensor performance by amplifying the sensor response to minute RI variations near the surface. Such enhanced field localization allows for the detection of ultralow concentrations of biomolecules, such as proteins, DNA, and disease biomarkers, with improved signal-to-noise ratios and exceptional sensitivity [33].

In practice, quasi-BICs are often employed to achieve tunable optical properties. Introducing a slight asymmetry into the otherwise symmetric structure (by modifying the geometry, refractive index contrast, or periodicity) permits controlled coupling to radiative modes, resulting in finite but adjustable Q-factors. For biosensing, this tunability allows fine optimization between strong field confinement and accessible optical coupling, providing a balance between sensitivity and practical operation [35].

In recent years, remarkable experimental progress has been made in the development of photonic crystal biosensors. Metasurface sensors utilizing bound states in the continuum have demonstrated detection of environmental pollutants and chemical vapors with substantially higher sensitivities compared to conventional resonant sensors [36][37]. In Section 2.5, the results of selected studies utilizing this optical sensor will be discussed to broaden the perspective.

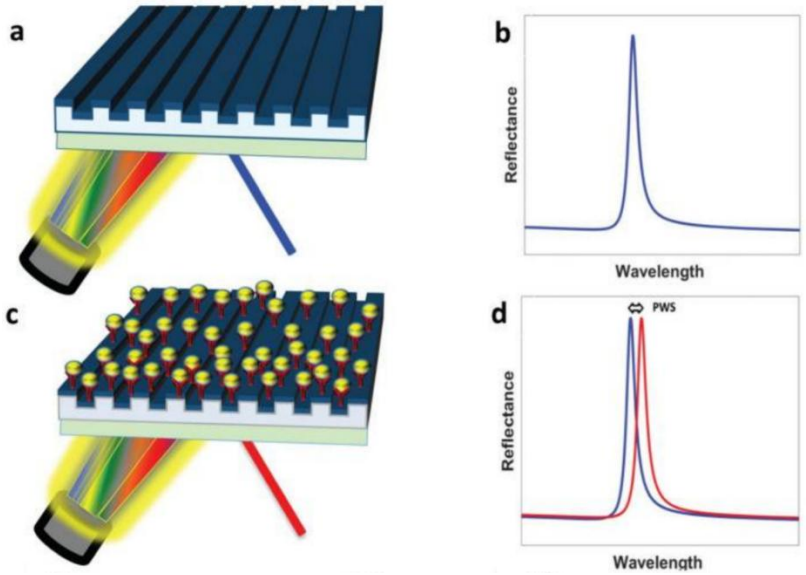

Figure 2.6: Schematic of the biosensing mechanism using photonic crystals. (a) Illustration of a one-dimensional (1-D) photonic crystal slab surface. (b) The associated resonance peak wavelength for this PC slab. (c) Functionalization of the slab surface followed by a biomolecular binding event through antigen-antibody interactions. (d) Resulting shift in the peak wavelength caused by the binding event [37].

2.4 Functionalization Strategies in Optical Biosensors

Before moving to specific biosensor studies, the attention is briefly focused on common sensor biofunctionalization strategies. Such term refers to the preparation and chemical modification of the sensor surface to enable the specific attachment of bioreceptors while preserving their biological activity and minimizing nonspecific adsorption [38][39][35]. This step is critical for label-free optical biosensors, as the biorecognition interface largely determines the reliability and accuracy of the assay. Two main aspects must be carefully optimized: the choice of biorecognition element, which ensures high affinity and specificity for the target analyte, and the immobilization strategy, which guarantees uniform coverage, correct biomolecule orientation, stability, and antifouling properties. Proper orientation maximizes target accessibility and detectability, stability allows repeated or flow-through measurements, and antifouling minimizes nonspecific adsorption from sample matrices, preventing false positives [38].

Functionalization strategies modify the sensor surface to immobilize bioreceptors using approaches such as physical adsorption, covalent binding, or nanomaterial-assisted methods. These techniques create a stable, efficient interface between the optical surface and the biological recognition element, such as an antibody, aptamer, or DNA probe, thereby enhancing the biosensor sensitivity, specificity, and stability.

In silicon-based photonic biosensors, the most commonly used waveguide materials are silicon oxide (SiO_2) and silicon nitride (Si_3N_4) [40]. Chemical modification of these surfaces is typically achieved through silanization [38]. Two widely adopted surface modification strategies, Silane-PEG-COOH and APTES-based amine functionalization, will be discussed in details in this section. Silanization generally relies on functional alkoxysilanes such as (3-aminopropyl)triethoxysilane (APTES) and COOH-PEG-silane, which react with surface hydroxyl groups (–OH) to form covalently bound and stable monolayers, providing an anchoring layer for bioreceptor immobilization [41]. The process typically involves three steps: First, surface activation, which generates reactive surface hydroxyls; Second, silane deposition, performed either in the liquid phase or in the vapor phase; and third, curing, which cross-links the silane molecules and stabilizes the monolayer [42].

2.4.1 Silane-PEG-COOH Functionalization

Silane-PEG-COOH functionalization represents a standard and robust approach for modifying silicon-based optical sensor surfaces such as SiO_2, Si_3N_4, and glass [43]. This strategy enables the introduction of terminal carboxylic acid (-COOH) groups on the surface, which are subsequently

used for covalent immobilization of biomolecules, typically through amine coupling reactions mediated by EDC/NHS chemistry [44]. The inclusion of a PEG spacer plays a crucial role in reducing non-specific adsorption of biomolecules and improving both the biocompatibility and stability of the functionalized surface [45].

In general, this functionalization strategy involves several steps. In the following, a typical example process is discussed, which usually begins with a thorough cleaning of the silicon-based substrate using organic solvents such as acetone and ethanol to remove surface contaminants, including dust, grease, and organic residues. A clean and pristine surface is essential for achieving a uniform and well-adhered silane layer. Following this initial cleaning, the sensor surface is subjected to plasma treatment, usually in an oxygen or air plasma environment. This step provides ultra-fine cleaning by oxidizing residual organic contaminants and, more importantly, activates the surface by generating hydroxyl (-OH) groups. These reactive sites serve as anchoring points for the subsequent silanization reaction, while the plasma exposure also increases surface energy and hydrophilicity, promoting better molecular coverage [46][47].

After plasma activation, the silicon-based substrate is immersed in a 15% nitric acid solution at 75 °C for 25 minutes. This treatment offers an additional oxidative cleaning and contributes to further hydroxylation of the surface, leading to the formation of a hydrophilic oxide layer rich in reactive -OH groups. The combination of plasma activation and nitric acid oxidation ensures a high density of surface hydroxyls, which is essential for efficient and stable silane coupling [46].

Next, the silanization step is carried out, where a solution of Silane-PEG-COOH in anhydrous dimethyl sulfoxide (DMSO) with a precise amount of water is applied to the surface and kept at 4 °C for about two hours. During this reaction, the silane group interacts with hydroxyl groups on the substrate, forming stable covalent Si-O-Si bonds that attach the silane to the surface. The PEG chain acts as a flexible hydrophilic spacer, effectively minimizing non-specific protein adsorption, while the terminal carboxylic acid (-COOH) groups provide functional handles for subsequent biomolecule conjugation. The presence of anhydrous DMSO is critical to prevent premature silane polymerization, whereas the controlled amount of water facilitates the necessary hydrolysis and condensation reactions [47]. The low reaction temperature promotes the controlled assembly of silane molecules, leading to the formation of a well-organized and uniform monolayer across the sensor surface [46].

Once the silanization is complete, the sensor surface is rinsed thoroughly with deionized water to remove unreacted silanes and by-products and is then dried before undergoing a curing step. The

curing process is typically performed in an autoclave at 121 °C for 90 minutes. This treatment promotes further condensation among residual silanol groups, enhances cross-linking within the silane network, and stabilizes the film, resulting in a dense and mechanically robust layer. The heat treatment also removes trapped solvents and ensures strong adhesion of the coating to the substrate.

After curing, the sensor is allowed to cool to room temperature and is then ready for integration into the optical setup. The resulting functionalized surface features a uniform layer of PEG-spaced carboxylic groups that can be activated by EDC/NHS chemistry for covalent attachment of biomolecules such as antibodies. This functionalization route provides a reliable and reproducible method for preparing silicon-based biosensor surfaces with high stability, excellent resistance to non-specific binding, and compatibility with a variety of optical biosensing applications [48].

2.4.2 APTES-Based Amine Functionalization

Surface functionalization using APTES is one of the most common strategies for introducing amine groups onto silicon-based photonic biosensors. This approach relies on the silanization of hydroxylated surfaces, where APTES molecules form covalent Si-O-Si bonds with the substrate, exposing terminal -NH_2 groups for subsequent bioconjugation. The amine-terminated layer thus serves as a versatile platform for covalent immobilization of biomolecules through crosslinkers such as BS^3 or via EDC/NHS-mediated coupling reactions [38][46].

The general workflow consists of three major stages, which are surface activation, silanization, and covalent linkage of biomolecules. The surface activation step ensures the formation of hydroxyl (-OH) groups that promote uniform silane attachment. This can be achieved by plasma or chemical oxidation treatments. For example, silicon-based substrate may undergo sequential cleaning with organic solvents such as acetone, ethanol, or hexane, followed by hydroxylation through plasma exposure or immersion in oxidizing solutions such as nitric acid or Piranha mixture (H_2SO_4:H_2O_2, 3:1 v/v) at elevated temperature. Additional treatments with alkaline and acidic solutions (NaOH and HCl) further activate the surface and ensure dense silanol formation [49].

Once activated, the substrates are immersed in anhydrous organic solvent solutions containing APTES, typically 1-5% (v/v) in dry ethanol or toluene. The silanization reaction proceeds at room temperature or slightly elevated temperatures, allowing the APTES molecules to form a uniform amine-terminated monolayer. After the reaction, the sensor surface is rinsed with organic solvents to remove unbound silanes and then subjected to a curing step (typically at 100-110 °C for 10-60 min) to promote condensation and stabilization of the silane network. The resulting surfaces exhibit stable -NH_2 terminations suitable for covalent coupling.

Two representative implementations of this method are discussed here. In the first approach, following plasma and nitric acid activation, the substrate is silanized in a toluene solution containing 1 vol.% APTES and 0.3 vol.% N,N-diisopropylethylamine (DIPEA). After curing at 110 °C, the surface is ready for subsequent biomolecule immobilization. Here, ligands can be pre-activated in solution using EDC/NHS chemistry, forming NHS-esters that readily react with the surface amines to create stable amide bonds. This indirect coupling strategy ensures efficient and oriented ligand attachment.

In the second implementation, the silicon-based substrate is activated using sequential Piranha and NaOH/HCl treatments, followed by silanization with 5% APTES in anhydrous toluene or ethanol. After curing at 100 °C, the surface is functionalized using the homobifunctional crosslinker BS^3, which reacts with the amine groups to generate NHS-activated esters. These groups enable subsequent immobilization of proteins via stable amide bond formation. Unreacted NHS sites are quenched with Tris-HCl buffer to minimize nonspecific adsorption, and the surface is then ready for biosensing measurements [50][51].

Although the two approaches differ slightly in solvent choice and activation conditions, both rely on the same fundamental chemistry: the introduction of surface amines via APTES silanization and subsequent covalent coupling through carbodiimide or NHS-ester crosslinking [52]. This well-established approach ensures a stable and durable surface, allows precise control over the density of reactive groups, and enables robust covalent immobilization of biomolecular probes, which enhances the long-term reliability and consistent performance of photonic biosensors [53].

2.4.3 Comparative assessment

Both Silane-PEG-COOH and APTES-based amine functionalization strategies are widely used for preparing silicon-based photonic biosensor surfaces. The Silane-PEG-COOH approach provides a PEGylated, carboxyl-terminated interface that effectively suppresses nonspecific adsorption and enables controlled biomolecule immobilization through EDC/NHS coupling, although its activation and coupling steps can be relatively time-consuming. In contrast, APTES-based amine functionalization generates an amine-terminated silane layer that supports versatile bioconjugation with carboxyl-containing ligands via crosslinkers such as BS^3 or through direct EDC/NHS chemistry. Although its antifouling properties are moderate and typically require a blocking step using agents like Tris-HCl buffer or non-fat dried milk, the APTES-based method offers several practical advantages, including straightforward implementation, strong covalent attachment, and stable surface chemistry. These attributes make it particularly suitable for robust and reproducible

biosensor interfaces. Table 2.1 summarizes the key comparative features of the two functionalization strategies.

Table 2.1: Comparative summary of Silane-PEG-COOH and APTES-based amine functionalization strategies used for surface modification of silicon-based photonic biosensors, highlighting their reactive groups, crosslinkers, antifouling behavior, and practical considerations.

Feature	Silane-PEG-COOH Functionalization	APTES-based Amine Functionalization
Functionalization Strategy	Silanization with PEG-linked carboxylic silane forming a COOH-terminated layer	Silanization with APTES forming an amine-terminated ($–NH_2$) layer
Reactive group	Carboxyl (–COOH)	Amine ($–NH_2$)
Crosslinker	EDC/NHS for coupling amine-containing biomolecules	BS^3 or EDC/NHS for coupling carboxyl-bearing ligands
Antifouling properties	Excellent, due to PEG spacer reducing nonspecific adsorption	Moderate; surface often requires blocking (such as Tris–HCl buffer or dried milk)
Comments	Produces uniform, hydrophilic, and low-fouling surfaces ideal for optical biosensing	Efficient covalent immobilization; blocking step needed for optimal reproducibility

2.5 Photonic Crystal: literature reviews

As anticipated, in recent years, extensive research has focused on employing photonic crystal platforms for label-free and highly sensitive biosensing applications. Leveraging their distinctive optical characteristics, these studies have achieved remarkable advancements in improving detection sensitivity, specificity, and compatibility with microfluidic integration. Among the most notable contributions, Romano et al. [50] developed a label-free optical biosensor utilizing a silicon nitride photonic crystal metasurface supporting bound states in the continuum for highly sensitive protein-protein interaction detection. The PhC, featuring a square lattice of air holes, was optimized to excite a symmetry-protected BIC resonance around 760 nm. This platform was applied to detect the interaction between p53 and MDM2 proteins, critical in cancer research. Surface functionalization involved immobilizing MDM2, causing a 1.6 nm red-shift in resonance, followed by p53 binding, which induced an additional 2.4 nm red-shift (Figure 2.7). These shifts, monitored via transmission spectra, directly correlated with protein surface density, enabling label-free detection with a limit of 66 nM for p53.

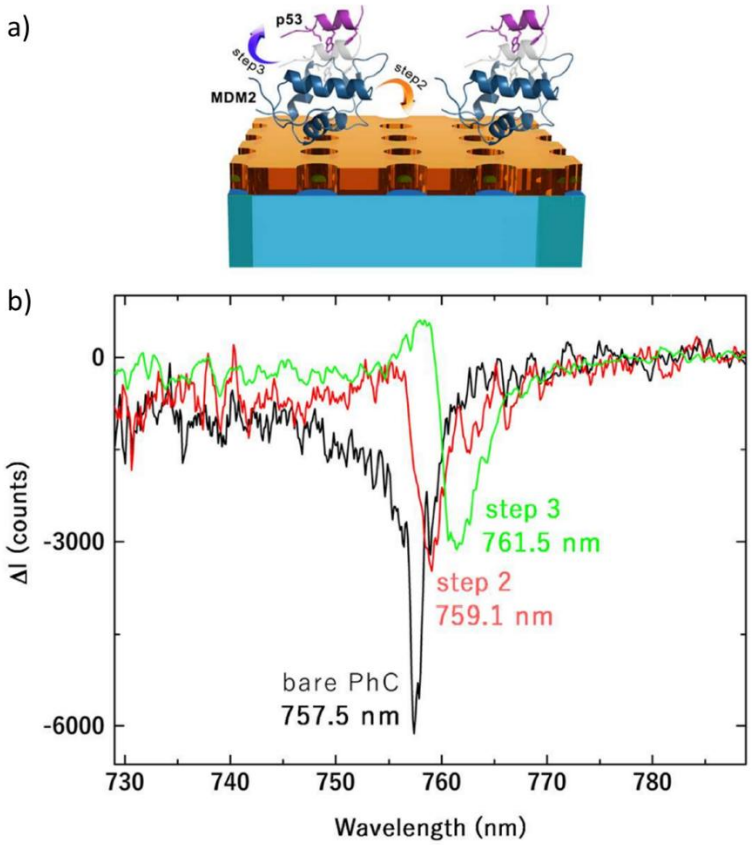

Figure 2.7: a) Schematic representation of the two-dimensional square photonic crystal with the MDM2 protein uniformly distributed across the sample surface and its subsequent interaction with the p53 protein. b) Measured transmission spectra obtained from the sensor device corresponding to the bare PhC (black curve), after MDM2 deposition (red curve), and following interaction with p53 (green curve). Negative intensity values result from background subtraction [50].

The same group also further demonstrated the possibility of detecting ultralow molecular weight molecules (186 Da) using the same sensor integration [54]. Integrating a microfluidic chamber, the sensor exhibited a bulk refractive index sensitivity of 178 nm/RIU and a high FOM of 445 due to its narrow resonance linewidth. A self-assembled monolayer of biphenyl-4-thiol (BPT), less than 1 nm thick, induced a 6 nm red-shift of the BIC resonance (Figure 2.8). This sensitivity for a minute, low molecular weight layer, corroborated by the high Q-factor (around 2000), surpasses the detection limits of traditional plasmonic sensors for small analytes.

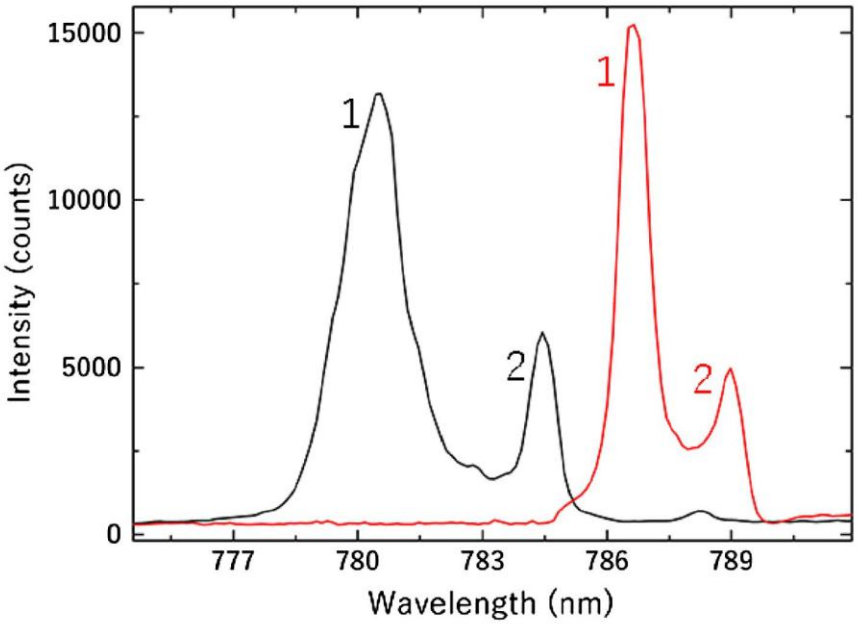

Figure 2.8: Cross-polarized transmission spectra of the PhCM-based sensor before (black curve) and after functionalization with a self-assembled BPT monolayer (red curve). The formation of the BPT monolayer induces a redshift at resonance wavelengths 1 and 2. A wavelength shift of 6 nm was measured following monolayer formation [54].

In another study, Romano et al. [55] also investigated the evanescent-field sensing mechanism enabled by the same sensor. This sensor, based on a transparent, subwavelength-thick silicon nitride photonic crystal slab, exhibits topology-induced field confinement normal to the slab, with an exponentially decaying evanescent tail extending into the surrounding medium. In contrast, the field remains delocalized in the plane of the slab, allowing for versatile and multiplexed sensing configurations. By infiltrating liquids of varying refractive indices (1.33–1.45) into a microfluidic chamber bonded to the metasurface, the researchers observed an exponential dependence of the resonance wavelength shift on the refractive index. This effect yielded differential sensitivities up to 226 nm/RIU with a high figure of merit. Numerical analyses confirmed that the enhanced sensitivity originates from the increased overlap between the BIC electromagnetic field and the analyte. Furthermore, theoretical optimization of the optical design predicted sensitivities as high as 4000 nm/RIU for molecular adsorption scenarios.

In another work, Zito et al. [56] developed a photonic crystal biosensor leveraging topologically confined quasi-BIC states in an ultrathin silicon nitride slab for label-free, real-time DNA detection. The sensor was designed to detect the binding interactions between immobilized PNA probes and their complementary DNA strands, demonstrating high sensitivity for low surface mass detection. Its 50 nm thick PhC slab supported high-Q modes, ensuring strong light-matter interaction, and

when integrated with a microfluidic system, enabled the detection of DNA concentrations as low as 0.05 nM. This corresponded to a sensitivity of 20 molecules per μm² (0.011 pg), indicating the sensor ability to reliably detect only a few tens of target DNA strands within each square micron. The experiments showed clear, stepwise red-shifts in resonance peaks upon c-DNA introduction, with negligible response to non-complementary strands, confirming both high sensitivity and selectivity.

In 2022, Schiattarella et al. [57] developed a high-Q photonic aptasensor for the trace detection of ochratoxin A (OTA), utilizing an avoided-crossing bound state in the continuum in a photonic crystal nanoslab. This design allowed for a high quality factor (Q ~ 1000) and a flat dispersion band over a range of interrogation angles, simplifying readout and reducing angle-sensitivity. The sensor employed a sandwich assay: an OTA-specific aptamer was immobilized on the PhC surface to capture OTA, followed by the binding of a large anti-OTA antibody which significantly amplified the refractive index change. This method achieved a limit of detection of 2.3 pg/mL and a high figure of merit (>160 RIU^{-1}), Moreover, the system robustness was significantly enhanced by utilizing the spectral separation between two distinct modes as a self-referenced signal. This differential measurement effectively cancels out common noise sources, by monitoring the difference in how these modes respond.

2.6 References

[1] P. Damborský, J. Švitel, and J. Katrlík, "Optical biosensors," *Essays Biochem*, vol. 60, no. 1, pp. 91–100, Jun. 2016, doi: 10.1042/EBC20150010.

[2] K. Fotiadis *et al.*, "Theoretical and Experimental Analysis of Single-Arm Bimodal Plasmo-Photonic Refractive Index Sensors," *Sensors*, vol. 24, no. 12, p. 3705, Jun. 2024, doi: 10.3390/s24123705.

[3] A. V. Kabashin, V. G. Kravets, and A. N. Grigorenko, "Label-free optical biosensing: going beyond the limits," *Chem Soc Rev*, vol. 52, no. 18, pp. 6554–6585, 2023, doi: 10.1039/D3CS00155E.

[4] G. Zanchetta, R. Lanfranco, F. Giavazzi, T. Bellini, and M. Buscaglia, "Emerging applications of label-free optical biosensors," *Nanophotonics*, vol. 6, no. 4, pp. 627–645, Jan. 2017, doi: 10.1515/nanoph-2016-0158.

[5] S. N. Khonina, G. S. Voronkov, E. P. Grakhova, N. L. Kazanskiy, R. V. Kutluyarov, and M. A. Butt, “Polymer Waveguide-Based Optical Sensors—Interest in Bio, Gas, Temperature, and Mechanical Sensing Applications,” *Coatings*, vol. 13, no. 3, p. 549, Mar. 2023, doi: 10.3390/coatings13030549.

[6] S. Mostufa *et al.*, “Advancements and Perspectives in Optical Biosensors,” *ACS Omega*, vol. 9, no. 23, pp. 24181–24202, Jun. 2024, doi: 10.1021/acsomega.4c01872.

[7] J. Slabý and J. Homola, “Performance of label-free optical biosensors: What is figure of merit (not) telling us?,” *Biosens Bioelectron*, vol. 212, p. 114426, Sep. 2022, doi: 10.1016/j.bios.2022.114426.

[8] S. Hosseini, F. Ibrahim, I. Djordjevic, and L. H. Koole, “Recent advances in surface functionalization techniques on polymethacrylate materials for optical biosensor applications,” *Analyst*, vol. 139, no. 12, p. 2933, 2014, doi: 10.1039/c3an01789c.

[9] B. Miranda, I. Rea, P. Dardano, L. De Stefano, and C. Forestiere, “Recent Advances in the Fabrication and Functionalization of Flexible Optical Biosensors: Toward Smart Life-Sciences Applications,” *Biosensors (Basel)*, vol. 11, no. 4, p. 107, Apr. 2021, doi: 10.3390/bios11040107.

[10] A. L. Hernandez, S. P. Pujari, M. F. Laguna, B. Santamaría, H. Zuilhof, and M. Holgado, “Efficient Chemical Surface Modification Protocol on SiO2 Transducers Applied to MMP9 Biosensing,” *Sensors*, vol. 21, no. 23, p. 8156, Dec. 2021, doi: 10.3390/s21238156.

[11] C. E. Soteropulos and H. K. Hunt, “Attaching Biological Probes to Silica Optical Biosensors Using Silane Coupling Agents,” *Journal of Visualized Experiments*, no. 63, May 2012, doi: 10.3791/3866.

[12] C. Ciminelli, F. Dell’Olio, D. Conteduca, and M. N. Armenise, “Silicon photonic biosensors,” *IET Optoelectronics*, vol. 13, no. 2, pp. 48–54, Apr. 2019, doi: 10.1049/iet-opt.2018.5082.

[13] M. A. Butt, “Surface Plasmon Resonance-Based Biodetection Systems: Principles, Progress and Applications—A Comprehensive Review,” *Biosensors (Basel)*, vol. 15, no. 1, p. 35, Jan. 2025, doi: 10.3390/bios15010035.

[14] Q. Wang *et al.*, “Research advances on surface plasmon resonance biosensors,” *Nanoscale*, vol. 14, no. 3, pp. 564–591, 2022, doi: 10.1039/D1NR05400G.

[15] M. Piliarik, H. Vaisocherová, and J. Homola, “Surface Plasmon Resonance Biosensing,” 2009, pp. 65–88. doi: 10.1007/978-1-60327-567-5_5.

[16] A. Paul, C. Musetti, R. Nanjunda, and W. D. Wilson, “Biosensor-Surface Plasmon Resonance: Label-Free Method for Investigation of Small Molecule-Quadruplex Nucleic Acid Interactions,” 2019, pp. 63–85. doi: 10.1007/978-1-4939-9666-7_4.

[17] C.-V. Topor, M. Puiu, and C. Bala, “Strategies for Surface Design in Surface Plasmon Resonance (SPR) Sensing,” *Biosensors (Basel)*, vol. 13, no. 4, p. 465, Apr. 2023, doi: 10.3390/bios13040465.

[18] J. Zhou, Y. Wang, and G.-J. Zhang, “State-of-the-art strategies of surface plasmon resonance biosensors in clinical analysis: A comprehensive review,” *Coord Chem Rev*, vol. 520, p. 216149, Dec. 2024, doi: 10.1016/j.ccr.2024.216149.

[19] R. B. M. Schasfoort, Ed., *Handbook of Surface Plasmon Resonance*. The Royal Society of Chemistry, 2017. doi: 10.1039/9781788010283.

[20] T. Špringer, M. Bocková, J. Slabý, F. Sohrabi, M. Čapková, and J. Homola, “Surface plasmon resonance biosensors and their medical applications,” *Biosens Bioelectron*, vol. 278, p. 117308, Jun. 2025, doi: 10.1016/j.bios.2025.117308.

[21] N. L. Kazanskiy, S. N. Khonina, and M. A. Butt, “A Review of Photonic Sensors Based on Ring Resonator Structures: Three Widely Used Platforms and Implications of Sensing Applications,” *Micromachines (Basel)*, vol. 14, no. 5, p. 1080, May 2023, doi: 10.3390/mi14051080.

[22] M. A. Butt, “Beyond the detection limit: A review of high-Q optical ring resonator sensors,” *Materials Today Physics*, vol. 58, p. 101873, Oct. 2025, doi: 10.1016/j.mtphys.2025.101873.

[23] A. Tsianaka *et al.*, “Sensitivity Enhancement of a Micro Ring Resonator-Based Photonic Sensor by Using a Gelatin Methacryloyl Functional Coating for the Detection of Metoprolol,” *ACS Applied Optical Materials*, vol. 3, no. 7, pp. 1556–1566, Jul. 2025, doi: 10.1021/acsaom.5c00149.

[24] A. Sarkaleh, B. Lahijani, H. Saberkari, and A. Esmaeeli, “Optical Ring Resonators: A Platform for Biological Sensing Applications,” *J Med Signals Sens*, vol. 7, no. 3, p. 185, 2017, doi: 10.4103/jmss.JMSS_9_17.

[25] M. A. Khalil *et al.*, “Highly sensitive split ring resonator-based sensor for quality monitoring of edible oils,” *Sci Rep*, vol. 15, no. 1, p. 2283, Jan. 2025, doi: 10.1038/s41598-025-85800-x.

[26] L. Milgrave, J. Alnis, and A. Bundulis, “Integrated polymer ring resonator sensor for environmental monitoring,” in *Optical Sensors 2025*, R. A. Lieberman, F. Baldini, and J. Homola, Eds., SPIE, May 2025, p. 67. doi: 10.1117/12.3056628.

[27] M. C. Cardenosa-Rubio, H. M. Robison, and R. C. Bailey, “Recent advances in environmental and clinical analysis using microring resonator–based sensors,” *Curr Opin Environ Sci Health*, vol. 10, pp. 38–46, Aug. 2019, doi: 10.1016/j.coesh.2019.09.001.

[28] Y. Sun and X. Fan, “Optical ring resonators for biochemical and chemical sensing,” *Anal Bioanal Chem*, vol. 399, no. 1, pp. 205–211, Jan. 2011, doi: 10.1007/s00216-010-4237-z.

[29] B. J. Luff, J. S. Wilkinson, J. Piehler, U. Hollenbach, J. Ingenhoff, and N. Fabricius, “Integrated optical Mach-Zehnder biosensor,” *Journal of Lightwave Technology*, vol. 16, no. 4, pp. 583–592, Apr. 1998, doi: 10.1109/50.664067.

[30] D. Martens and P. Bienstman, “Study on the limit of detection in MZI-based biosensor systems,” *Sci Rep*, vol. 9, no. 1, p. 5767, Apr. 2019, doi: 10.1038/s41598-019-42305-8.

[31] X. Li *et al.*, “A review of specialty fiber biosensors based on interferometer configuration,” *J Biophotonics*, vol. 14, no. 6, Jun. 2021, doi: 10.1002/jbio.202100068.

[32] S. Herranz, A. F. Gavela, and L. M. Lechuga, “Label-Free Biosensors Based on Bimodal Waveguide (BiMW) Interferometers,” 2017, pp. 161–185. doi: 10.1007/978-1-4939-6848-0_11.

[33] B. T. Cunningham, M. Zhang, Y. Zhuo, L. Kwon, and C. Race, “Recent Advances in Biosensing With Photonic Crystal Surfaces: A Review,” *IEEE Sens J*, vol. 16, no. 10, pp. 3349–3366, May 2016, doi: 10.1109/JSEN.2015.2429738.

[34] H. Zhong, T. He, Y. Meng, and Q. Xiao, “Photonic Bound States in the Continuum in Nanostructures,” *Materials*, vol. 16, no. 22, p. 7112, Nov. 2023, doi: 10.3390/ma16227112.

[35] F. Dell’Olio, “Metasurface-Enabled Microphotonic Biosensors via BIC Modes,” *Photonics*, vol. 12, no. 1, p. 48, Jan. 2025, doi: 10.3390/photonics12010048.

[36] Z. Jing, W. Jiaxian, G. Lizhen, and Q. Weibin, “High-Sensitivity Sensing in All-Dielectric Metasurface Driven by Quasi-Bound States in the Continuum,” *Nanomaterials*, vol. 13, no. 3, p. 505, Jan. 2023, doi: 10.3390/nano13030505.

[37] H. Inan *et al.*, “Photonic crystals: emerging biosensors and their promise for point-of-care applications,” *Chem Soc Rev*, vol. 46, no. 2, pp. 366–388, 2017, doi: 10.1039/C6CS00206D.

[38] M. Soler and L. M. Lechuga, “Biochemistry strategies for label-free optical sensor biofunctionalization: advances towards real applicability,” *Anal Bioanal Chem*, vol. 414, no. 18, pp. 5071–5085, Jul. 2022, doi: 10.1007/s00216-021-03751-4.

[39] F. Wang, Y. Xie, W. Zhu, and T. Wei, “Recent Advances in Functionalization Strategies for Biosensor Interfaces, Especially the Emerging Electro-Click: A Review,” *Chemosensors*, vol. 11, no. 9, p. 481, Sep. 2023, doi: 10.3390/chemosensors11090481.

[40] M.-J. Bañuls, R. Puchades, and Á. Maquieira, "Chemical surface modifications for the development of silicon-based label-free integrated optical (IO) biosensors: A review," *Anal Chim Acta*, vol. 777, pp. 1–16, May 2013, doi: 10.1016/j.aca.2013.01.025.

[41] L. Giraud *et al.*, "Amino-functionalized monolayers covalently grafted to silica-based substrates as a robust primer anchorage in aqueous media," *Appl Surf Sci*, vol. 370, pp. 476–485, May 2016, doi: 10.1016/j.apsusc.2016.02.141.

[42] F. Zhang *et al.*, "Chemical Vapor Deposition of Three Aminosilanes on Silicon Dioxide: Surface Characterization, Stability, Effects of Silane Concentration, and Cyanine Dye Adsorption," *Langmuir*, vol. 26, no. 18, pp. 14648–14654, Sep. 2010, doi: 10.1021/la102447y.

[43] M. J. Sweetman, C. J. Shearer, J. G. Shapter, and N. H. Voelcker, "Dual Silane Surface Functionalization for the Selective Attachment of Human Neuronal Cells to Porous Silicon," *Langmuir*, vol. 27, no. 15, pp. 9497–9503, Aug. 2011, doi: 10.1021/la201760w.

[44] M. J. E. Fischer, "Amine Coupling Through EDC/NHS: A Practical Approach," 2010, pp. 55–73. doi: 10.1007/978-1-60761-670-2_3.

[45] A. S. Anderson *et al.*, "Functional PEG-Modified Thin Films for Biological Detection," *Langmuir*, vol. 24, no. 5, pp. 2240–2247, Mar. 2008, doi: 10.1021/la7033438.

[46] L. Torrijos-Morán, B. D. Lisboa, M. Soler, L. M. Lechuga, and J. García-Rupérez, "Integrated optical bimodal waveguide biosensors: Principles and applications," *Results in Optics*, vol. 9, p. 100285, Dec. 2022, doi: 10.1016/j.rio.2022.100285.

[47] J. Maldonado, M.-C. Estévez, A. Fernández-Gavela, J. J. González-López, A. B. González-Guerrero, and L. M. Lechuga, "Label-free detection of nosocomial bacteria using a nanophotonic interferometric biosensor," *Analyst*, vol. 145, no. 2, pp. 497–506, 2020, doi: 10.1039/C9AN01485C.

[48] L. S. Puumala *et al.*, "Biofunctionalization of Multiplexed Silicon Photonic Biosensors," *Biosensors (Basel)*, vol. 13, no. 1, p. 53, Dec. 2022, doi: 10.3390/bios13010053.

[49] A. B. González-Guerrero, M. Alvarez, A. G. Castaño, C. Domínguez, and L. M. Lechuga, "A comparative study of in-flow and micro-patterning biofunctionalization protocols for nanophotonic silicon-based biosensors," *J Colloid Interface Sci*, vol. 393, pp. 402–410, Mar. 2013, doi: 10.1016/j.jcis.2012.10.040.

[50] S. Romano *et al.*, "Optical Biosensors Based on Photonic Crystals Supporting Bound States in the Continuum," *Materials*, vol. 11, no. 4, p. 526, Mar. 2018, doi: 10.3390/ma11040526.

[51] M. Sypabekova, A. Hagemann, D. Rho, and S. Kim, "Review: 3-Aminopropyltriethoxysilane (APTES) Deposition Methods on Oxide Surfaces in Solution and Vapor Phases for

Biosensing Applications," *Biosensors (Basel)*, vol. 13, no. 1, p. 36, Dec. 2022, doi: 10.3390/bios13010036.

[52] M. E. Marques, A. A. P. Mansur, and H. S. Mansur, "Chemical functionalization of surfaces for building three-dimensional engineered biosensors," *Appl Surf Sci*, vol. 275, pp. 347–360, Jun. 2013, doi: 10.1016/j.apsusc.2012.12.099.

[53] A. Chiadò *et al.*, "Optimization and characterization of a homogeneous carboxylic surface functionalization for silicon-based biosensing," *Colloids Surf B Biointerfaces*, vol. 143, pp. 252–259, Jul. 2016, doi: 10.1016/j.colsurfb.2016.03.048.

[54] S. Romano *et al.*, "Label-free sensing of ultralow-weight molecules with all-dielectric metasurfaces supporting bound states in the continuum," *Photonics Res*, vol. 6, no. 7, p. 726, Jul. 2018, doi: 10.1364/PRJ.6.000726.

[55] S. Romano *et al.*, "Tuning the exponential sensitivity of a bound-state-in-continuum optical sensor," *Opt Express*, vol. 27, no. 13, p. 18776, Jun. 2019, doi: 10.1364/OE.27.018776.

[56] G. Zito *et al.*, "Label-free DNA biosensing by topological light confinement," *Nanophotonics*, vol. 10, no. 17, pp. 4279–4287, Nov. 2021, doi: 10.1515/nanoph-2021-0396.

[57] C. Schiattarella *et al.*, "High-Q photonic aptasensor based on avoided crossing bound states in the continuum and trace detection of ochratoxin A," *Biosens Bioelectron X*, vol. 12, p. 100262, Dec. 2022, doi: 10.1016/j.biosx.2022.100262.

Chapter 3: A Molecularly Imprinted Polymer (MIP) Sensor Empowered by Bound States in the Continuum for Selective Trace-Detection of TGF-β

3.1. Introduction

This chapter presents the results of the development and testing of a photonic biosensor based on bound states in the continuum, integrated with a molecularly imprinted polymer (MIP), for the detection of the Transforming growth factor-beta (TGF-β) biomarker. The work was carried out within a collaboration between ISASI-CNR, CNR NANOTEC Institute of Nanotechnology and Molecular Foundry. The results have been published in Advanced Science [1] and presented at several international conferences [2].

TGF-β is a cytokine involved in many biological and disease processes, including cancer. Elevated salivary TGF-β is linked to oral cancer progression, making its rapid, sensitive detection clinically important. Traditional assays like ELISA are sensitive but require costly reagents, large samples, and complex procedures, limiting point-of-care use. While electrochemical biosensors improve sensitivity, they often depend on biological recognition elements and intricate surface treatments. There is a strong need for a label-free, highly sensitive, and simple TGF-β sensor suitable for real-time detection in minimally processed samples, capable of detecting concentrations in the picomolar range [3][4].

3.1.1 Motivation and Chapter Objective

Given the need for a point-of-care TGF-β assay, the integration of a photonic BIC transducer [5][6][7] with a synthetic MIP receptor represents a compelling strategy. MIPs are low-cost, robust synthetic receptors that mimic antibody recognition by forming binding sites complementary to a target molecule [8][9]. Polydopamine (PDA) is an ideal MIP material due to its self-polymerization in mild conditions, biocompatibility, and suitability for protein imprinting. PDA-based MIPs have shown strong affinity, stability, and reusability for various biomolecules, offering high selectivity without the need for biological components, making them well-suited for practical sensing applications [10][11]. The BIC resonator provides an ultrahigh-Q optical mode highly sensitive to refractive index perturbations at the sensor surface, where the bound state in the continuum (BIC)

refers to a non-radiative optical mode that remains strongly confined despite being embedded within the radiation continuum. By localizing the evanescent field in the immediate vicinity of the surface, any binding of target biomolecules that changes the local refractive index will produce a measurable spectral shift in the resonance. This offers a label-free detection mechanism that is real-time and scalable over large sensing areas [12][13]. Meanwhile, the MIP layer can selectively capture TGF-β from a complex sample due to its imprinted binding sites, ensuring specificity of the sensor response. Importantly, the MIP can be directly polymerized on the photonic structure without complicated conjugation protocols, simplifying sensor preparation compared to antibody functionalization. The synergy of the two components (the MIP-based biomimetic recognition that operates without biological receptors and the BIC-amplified transduction) is expected to enable detection of TGF-β at ultralow concentrations with high selectivity.

The combined use of a BIC-based PhC slab and a PDA MIP is justified by the way their strengths complement each other. The confined optical field of the BIC is maximized exactly where the MIP layer resides, thus any TGF-β binding within the polymer cavities induces an enhanced optical perturbation. In fact, the BIC senses the molecular binding as a refractive index change, and its extreme sensitivity translates that into a significant optical signal (a resonance wavelength shift). On the other hand, the MIP provides molecular selectivity to the otherwise non-specific photonic sensor, enabling it to distinguish the target molecule from other interfering substances in the sample. This combination allows femtomolar-level sensitivity to be achieved for TGF-β without the need for enzymatic amplification or labeled secondary reactions (as required in ELISA or sandwich assays). The approach thus addresses the key challenges: attaining a LOD well below clinically relevant TGF-β levels (which are on the order of picomolar in saliva), and ensuring specificity in a complex biological matrix.

This chapter presents the design, fabrication, and validation of a hybrid MIP-BIC sensor for selective, sub-picomolar detection of TGF-β, benchmarked against state-of-the-art biosensors. Section 3.2 details the photonic crystal slab design for high-Q quasi-BIC resonance, the molecular imprinting method for TGF-β selectivity, and device assembly with microfluidics and optical readout. Section 3.3 covers sensor performance, including refractometric transduction, dual-mode readout (spectral and angular shifts), sensitivity, and specificity through cross-reactivity tests versus controls. Detection in a saliva simulant is also demonstrated. Section 3.4 compares the sensor to existing methods and summarizes findings. References are listed in Section 3.5.

3.2. Sensor Design, Fabrication, and Experimental Setup

3.2.1 Photonic Crystal Slab Design for BIC Resonance

3.2.1.1 Theoretical and Numerical Simulations

A spectral refractometric sensor detects analyte concentration changes by monitoring the shift of its resonant wavelength. A narrow resonance allows quantifying the analyte concentration accurately [13][14]. A greater spectral shift corresponds to a higher concentration of the target analyte, provided the measurement remains within the non-saturated regime. For a fixed analyte concentration, a larger spectral shift reflects higher sensor sensitivity. Figure 3.1a illustrates the selective binding principle of TGF-β through the MIP. The PhCS design followed a specific strategy. Initially, resonances were designed in the near-infrared spectral range, exploiting the sensitivity increase with the wavelength (λ) [15]. For a sufficiently small thickness of the patterned silicon nitride slab (i.e., t = 70 nm when a = 540 nm, which defines the Dirac cone condition), the three principal dispersion curves are degenerate at the Γ point in momentum space. In this work, t = 90 nm is deliberately chosen to break this degeneracy and obtain quasi-BICs [12]. In Figure 3.1b, the evolution of the bands with increasing slab thickness t is presented. Instead of typical reflectance spectra R_s (s polarization, TE-like modes), we depict absorptance in logarithmic scale, $\log_{10}[A(\lambda)] = \log_{10}[1 - T_s(\lambda) - R_s(\lambda)]$ (with T_s as the associated transmittance). This representation better reflects the real position of the maximum field of generally asymmetric Fano-shaped resonances and simultaneously provides an estimate of the local field intensity (proportional to $A(\lambda)$), crucial for enhancing sensing capabilities.

As evidenced from Figure 3.1c, even under significant perturbation of the refractive index of the MIP imprinting layer, the Dirac cone degeneracy remains stable as the spectral position of the modes is minimally affected (left inset). Only with a larger imprinting thickness of δt = 25 nm does significant spectral mode splitting occur (right inset). Deliberately breaking the Dirac cone with increasing t results in two emerging BICs at λ_2 and λ_3, situated at lower energies than the dipole lossy band at λ_1 (Figure 3.1d,e). This yields two resonant peaks with an ultra-high Q_r-factor.

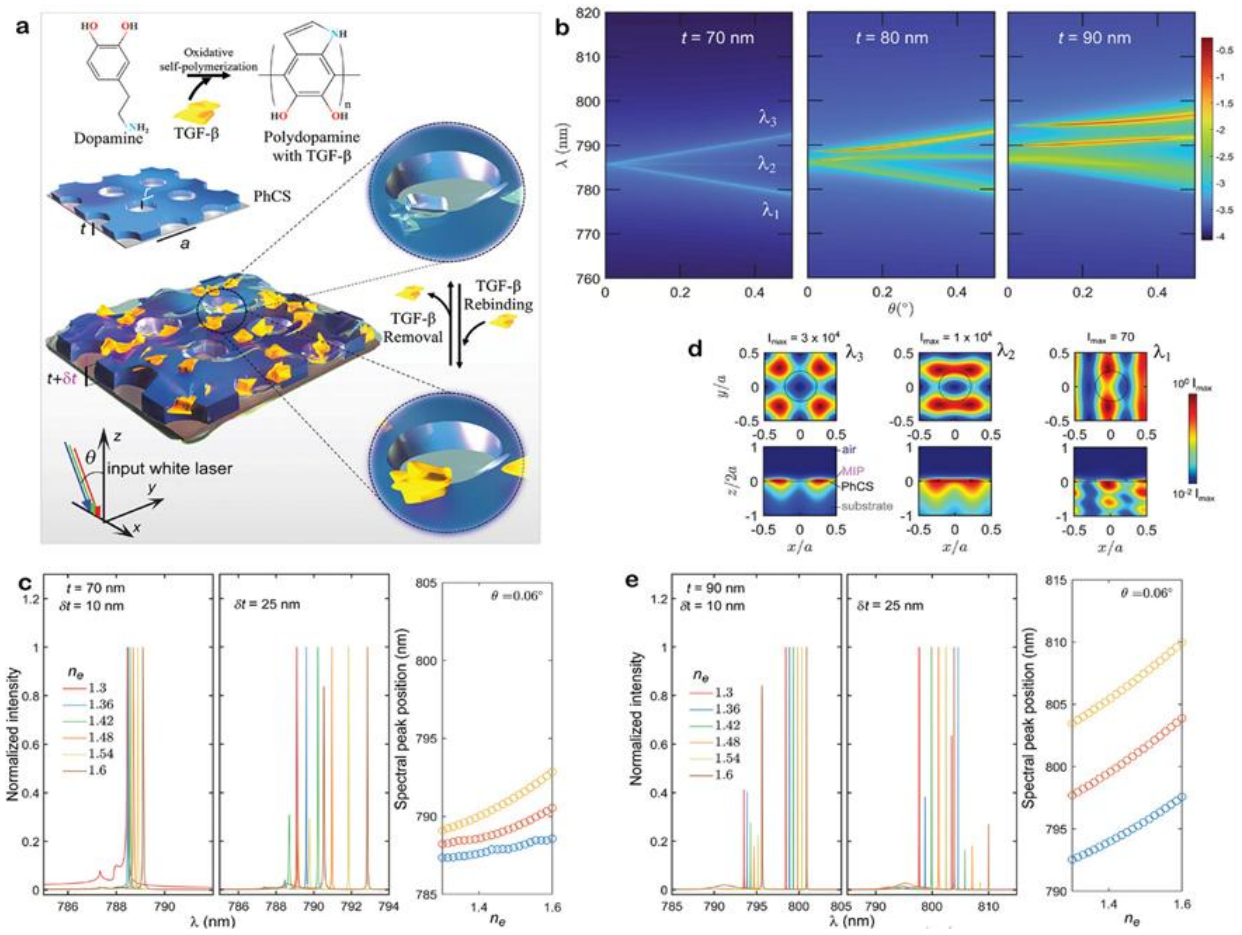

Figure 3.1: a) Scheme of MIP-BIC sensor for TGF-β detection, the incidence angle θ lies in the xz-plane. b) Evolution of the principal dispersion absorptance curves $\log_{10}A(\theta)$ (colorbar log scale) with the thickness of the slab t. c) Simulated spectra for δt = 10 nm and 25 nm, with correspondent peak evolution as a function of the cladding effective refractive index n_e for the three modes λ_1 (cyan), λ_2 (red), λ_3 (orange), estimated considering an incident angle close to the normal (θ = 0.06°). d) Near field intensity cross sections for the modes λ_1, λ_2, and λ_3 simulated for t = 90 nm (experimental case) at the xy-plane: z/a = 0, and xz-plane: y/a = 0.25. (e) Same as in (c) for t = 90 nm, corresponding to the experimental structure actually used [1].

To predict the sensor response to TGF-β binding, the MIP coating and its refractive index change upon analyte uptake has been modeled. The investigation into the dependence of the BIC sensor on the refractive index of the MIP layer was conducted as follows. The refractive index of the MIP under conditions of high density and uniformity is denoted as n_{MIP}=1.74 [16]. A Langmuir isotherm, representing the surface binding process with a maximal filling fraction of 0.6x (equivalent to a 60% filling fraction in random close packing), is considered. This filling fraction is proportional to the molecule concentration C in the solvent and is expressed as:

$$x = \frac{KC}{(1 + KC)} \tag{3-1}$$

where k is the dissociation constant [17]. To model the binding of analyte molecules, an effective refractive index $n_e(C)$ is introduced to account for the conformal MIP layer. A MIP film with voids, created by template molecules, is envisaged. These voids are expected to be filled with TGF-β upon subsequent resorption.

The asymptotic adsorption level is described by the MIP being fully filled with molecules, forming an approximate monolayer. An upper limit for the TGF-β-MIP filling fraction of 60% is anticipated, as mentioned earlier. Consequently, the resorption of TGF-β into MIP is simulated by varying the effective refractive index of the cladding, denoted as ne, in the range from 1.3 (corresponding to a MIP matrix with 60% voids) to 1.6. This upper limit corresponds to a MIP matrix with 60% filled with TGF-β of refractive index n_{tgf} = 1.5. The relationship is given by:

$$n_e = (1 - 0.6)n_{MIP} + 0.6\big(n_{TGF}x + (1 - x)\big) \tag{3-2}$$

which can be further expressed, using Eq. (3.1), as a function of the concentration C and parameterized based on the actual value of k. Figure 3.2 illustrates the evolution of ne(C) with TGF-β concentration.

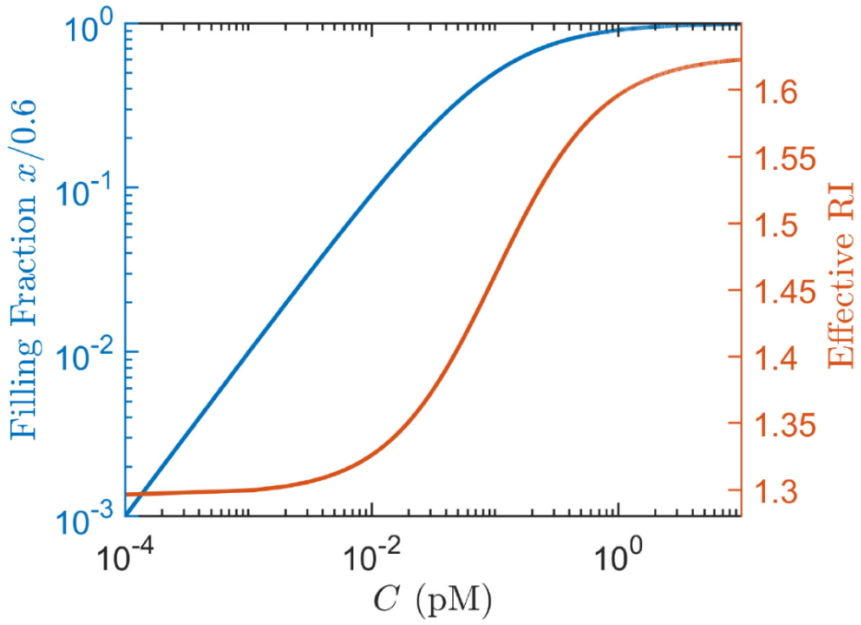

Figure 3.2: Langmuir isotherm (blue solid line) and retrieved behavior of the effective refractive index as function of analyte concentration [1].

3D finite-difference time-domain (FDTD) and rigorous coupled-wave analysis (RCWA) simulations to quantify how the BIC resonance shifts with changes in n_e and MIP thickness δt were carried out. The results indicated an approximately exponential dependence of the resonant wavelength on n_e, meaning the sensor sensitivity (wavelength shift per RI change) is higher at lower concentrations where n_e is closer to the base value. This is advantageous for detecting trace levels. For example, increasing n_e from 1.30 to 1.33 (corresponding to going from 0 to 10 fM TGF-β, roughly) produces a relatively large fraction of the total shift. It was also observed that the resonance shift increases with MIP layer thickness up to approximately 100 nm, after which further thickness yields minimal additional effect. Given the actual MIP thickness of 20 nm, simulations predicted a maximum spectral shift of 5-6 nm upon saturating the MIP with TGF-β, consistent with the 4-5 nm shift observed in experiments. This validates that the effective index model and chosen structural parameters should allow detectable shifts even for very low surface coverages of target.

3.2.1.2 Engineering High Q-factor Resonances

A key design goal was to maximize the resonant Q-factor, since higher Q yields narrower linewidth and thus improved resolution for small wavelength shifts. In a real device, the infinite Q of an ideal BIC is degraded to a finite but high Q due to perturbations like fabrication imperfections, finite size, and material absorption. The PhC geometry is engineered to achieve a radiative Q_r as high as possible while maintaining a robust resonance. By choosing symmetric unit cells (circular holes in a square lattice), it is ensured that the modes remain symmetry-protected with respect to out-of-plane radiation at normal incidence. The slight off-normal angle interrogation that is used (to couple light in) means the BIC converts to a very narrow Fano resonance (since true BIC occurs strictly at $\theta = 0$). The simulations predicted Q_r on the order of 10^4–10^5 for angles within 0.1° of normal, primarily limited by the finite resolution of the computational grid and the idealized assumption of an infinitely periodic structure.

In practice, the total measured Q-factor also accounts for non-radiative losses, including contributions from material absorption and scattering (Q_a). Several measures are taken to keep these losses minimal. First, the Si_3N_4 film was deposited by plasma-enhanced chemical vapor deposition (PECVD) with optimized conditions to reduce optical absorption; ellipsometric characterization confirmed that absorption in the near-IR region is minimal, with the imaginary part of the refractive index around 10^{-6}. Second, high-resolution electron-beam lithography [14] and careful etching were employed to fabricate smooth, well-defined nanoholes, thereby minimizing scattering losses from sidewall roughness. As a result, the fabricated PhC shows extremely low optical losses, meaning the Q-factor is primarily governed by radiative coupling, which is desirable for achieving a BIC with

minimal radiation loss. At the optimum coupling condition (where radiative loss equals absorptive loss, $Q_r = Q_a$) [18][19], the intensity of the resonant field in the slab reaches a maximum (critical coupling), which corresponds to an incidence angle θ=0.03°, as shown by simulations and confirmed by experiment. The near-field intensity at that angle is orders of magnitude higher than that of a typical dipolar resonance (Figure 3.1d inset), indicating the unique field confinement of the BIC.

Any analyte-induced perturbation (such as refractive index change in the MIP) will inevitably break some symmetry and thus couple the quasi-BIC mode slightly more to radiation, reducing its Q [20]. Paradoxically, this can be beneficial to maintain a visible resonance peak even as conditions change. It is observed that as TGF-β concentration increases, the resonance redshifts and broadens (Q decreases), but the overall detectability remains high, as the wavelength shift increases faster than the linewidth broadening, maintaining a high signal-to-noise ratio.

3.2.1.3 Fabrication Process

The PhC slab was fabricated on a silicon nitride film deposited on a transparent quartz substrate. A 70 nm thick Si_3N_4 layer was first deposited via PECVD on a 500 μm thick SiO_2 wafer. Standard electron-beam lithography (100 keV) was used to define a square lattice of circular holes with period a=540 nm [14]. The pattern was transferred into the Si_3N_4 layer by reactive ion etching, achieving hole radius r =144 nm (27% of the period) as designed. The final Si_3N_4 slab thickness measured by ellipsometry was t = 90 nm, slightly thicker than the Dirac point thickness, a deliberate choice that moves the device into the quasi-BIC regime while preserving high-Q modes, as previously discussed [13]. The fabricated photonic crystal areas were large (on the order of square millimeters) to allow optical probing and integration with a fluidic chamber [21]. The MIP-BIC sensor interrogation is schematically represented in Figure 3.3.

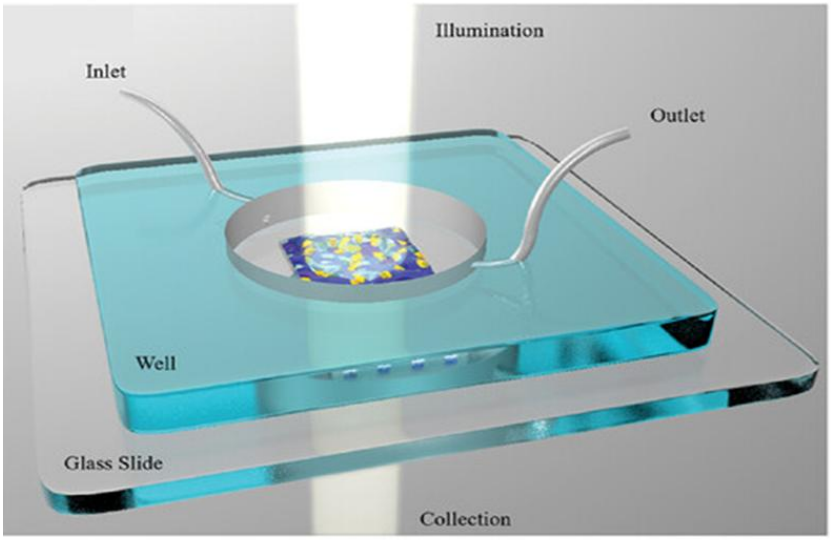

Figure 3.3: Scheme of MIP-BIC sensor interrogation [1].

3.2.2 Synthesis and Integration of the Molecularly Imprinted Polymer (MIP)

3.2.2.1 MIP Synthesis Protocol

To provide selectivity for TGF-β, a thin film of molecularly imprinted polydopamine was synthesized directly on the PhC slab. TGF-β was used as a template in a surface imprinting method during the polymerization of dopamine. The PhC chip was immersed in a Tris-HCl solution (pH 8.5) containing 0.1 mg/mL dopamine hydrochloride (monomer) and 1 µg/mL TGF-β (template protein), a concentration many orders of magnitude higher than the detectable levels in the final assay, as is typical for molecularly imprinted polymers (MIPs). Under these mildly basic conditions, dopamine undergoes auto-oxidation and subsequent polymerization, resulting in a uniform polydopamine coating on both Si_3N_4 and glass surfaces. Polymerization was carried out overnight (12 h) at room temperature to achieve adequate film thickness for effective imprinting [11]. The catechol and amine functionalities of polydopamine facilitate non-covalent interactions with the template proteins during film formation, enabling the creation of molecularly imprinted binding sites [22].

After polymerization, the template TGF-β molecules were removed to create the imprinted cavities. The chip was rinsed thoroughly with an ethanol/water mixture, then treated with 0.25 M NaOH solution, which helps disrupt any remaining protein-polymer interactions and washes out the TGF-β [22]. This established the MIP, a PDA network containing nanocavities complementary to TGF-β in size, shape, and functional groups [11]. The MIP fabrication process is summarized in Figure 3.4a,

which schematically illustrates dopamine polymer deposition, template entrapment, and subsequent template removal.

Importantly, polydopamine exhibits strong adhesion to Si_3N_4, glass, and metal surfaces, enabling imprinting not only on the photonic sensor but also on a reference electrode used for characterization. The simple, one-step dip-coating approach using a dopamine–template solution enhances both the reproducibility and scalability of the fabrication process. There is no need for surface silanization or linker molecules, as the polydopamine film forms spontaneously and adheres to the substrate through a combination of covalent and noncovalent interactions, similar to those employed by mussel adhesive proteins. By following the same polymerization conditions each time, consistent MIP coatings on multiple PhC chips is achieved.

3.2.2.2 Deposition and Functionalization

The deposition of the MIP on the PhC was confirmed by a slight visible coloration of the chip (PDA typically yields a brownish coating) and by optical measurements of the resonance (initial redshift and slight broadening after polymerization due to the added layer) [11]. The thickness of the PDA film on the PhC was estimated to be on the order of 10–25 nm from ellipsometry and AFM. This thickness is advantageous: it is thin enough that the evanescent field of the BIC still penetrates through the entire polymer (maximizing overlap with any bound analyte), yet thick enough to capture a significant amount of template and provide a lot of binding sites.

During polymerization, some TGF-β likely became trapped near the PDA film outer surface, while some may have diffused slightly into the matrix. The washing steps were optimized to effectively eliminate the template. A gentle basic wash (NaOH) was used to effectively remove the protein without harming the polymer. Following this step, the imprinted cavities are preserved. Functionalization occurs naturally during polymerization, as dopamine polycatechol structure forms hydrogen bonds and aromatic ring interactions with the protein, resulting in imprints that maintain complementary binding sites [22].

To verify that the imprinting process proceeded correctly, a non-imprinted polymer (NIP) control was prepared by depositing a PDA film on a separate PhC chip under the same conditions but without TGF-β in the solution. This produced a polymer with comparable thickness and composition but without the specific binding cavities. The NIP serves as a control to test non-specific binding in later experiments (Section 3.3.4).

3.2.2.3 MIP Characterization

To verify the effectiveness of the molecular imprinting process and to characterize the MIP film, both electrochemical and microscopic analyses were performed. Electrochemical characterization was first carried out using differential pulse voltammetry (DPV) on a separate platinum electrode [23]. The electrode was coated with a polydopamine layer in the presence of TGF-β, allowing the imprinting process to occur. Cyclic DPV measurements were recorded in a ferricyanide redox probe after each fabrication stage: following polymerization (when the template was still embedded in the film), after template removal, and after TGF-β rebinding. As shown in Figure 3.4b, the bare platinum electrode initially exhibited a distinct redox peak current. Once the PDA layer was deposited, the current decreased noticeably, indicating that the insulating polymer hindered electron transfer. After the template molecules were removed, the current partially recovered, suggesting that the newly formed cavities allowed redox ions to reach the electrode surface more easily. When the MIP was subsequently exposed to TGF-β (10 ng/mL), the current again decreased as the protein reoccupied the cavities, obstructing electron flow. This sequence of DPV responses confirmed that the PDA film was successfully deposited, that template removal created functional cavities, and that TGF-β could specifically rebind to these sites. Although this test was conducted off-chip, the results validated that the MIP synthesis protocol produced a functional, selectively imprinted polymer.

The film morphology was further examined using atomic force microscopy (AFM) in non-contact mode [24]. AFM scans of the MIP-coated photonic crystal surface, shown in Figure 3.5, revealed that the PDA layer uniformly covered both the top surface and the inner walls of the nanoholes. The images (Figure 3.5a,b) displayed a smooth surface with nanoscale granularity typical of polymerized dopamine. A cross-sectional profile taken across a hole boundary (Figure 3.5c) showed that the hole depth decreased by approximately 20 nm after coating, indicating a polymer thickness of about 15 nm on average, with variations between 10 and 25 nm. This result aligns with the design target and supports the DPV findings, confirming that the film is thin enough to retain porous cavities for analyte binding. Importantly, AFM measurements also showed that the nanohole structure of the PhC remained largely intact, with an average residual depth of around 65 nm compared to the original 70 nm. This demonstrates that the MIP layer was successfully integrated without compromising the optical resonance properties of the photonic crystal, providing both selectivity and structural compatibility essential for effective sensing.

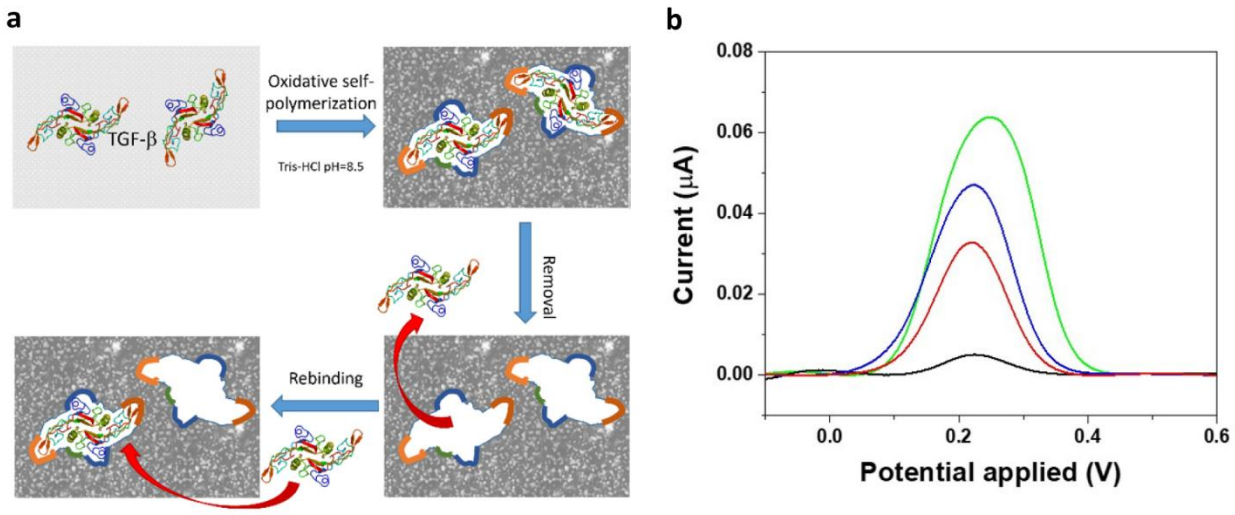

Figure 3.4: MIP fabrication and electrochemical characterization. a) Schematic illustration of the MIP synthesis on the photonic crystal: (i) Dopamine monomer (DA) and TGF-β template molecules in solution; (ii) self-polymerization of DA deposits a PDA film on the PhC, entrapping TGF-β in the forming matrix (adsorption); (iii) removal of TGF-β leaves behind imprinted cavities complementary to the target (resorption); these cavities can later rebind TGF-β. b) DPV curves (current I vs. voltage E) from a Pt electrode undergoing the same MIP formation steps. Black: after PDA deposition (with TGF-β), the oxidation peak current decreases due to the insulating polymer blocking the electrode. Blue: after template removal, the current increases as cavities allow partial redox probe access. Red: after rebinding TGF-β (10 ng/mL), current decreases again, indicating TGF-β molecules occupying cavities and hindering probe diffusion. These changes confirm the successful imprinting of cavities and rebinding of target [1].

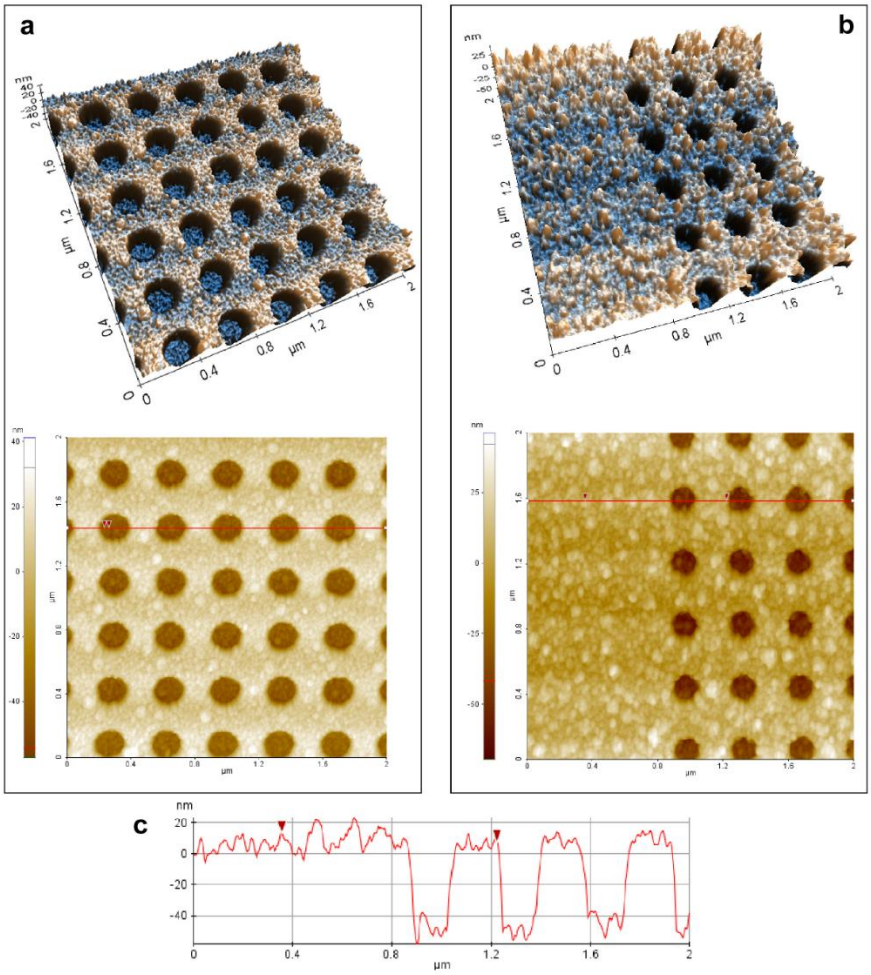

Figure 3.5: Morphology of the MIP-coated photonic crystal. a) Atomic force microscopy (AFM) topography of the PDA MIP layer on the PhC (2 µm × 2 µm scan). The polymer uniformly coats the surface, following the periodic hole pattern. b) Zoomed-in AFM image at the boundary of a photonic crystal hole. The MIP film covers the top and partially the sidewall of the hole. c) Cross-sectional profile of the MIP across a hole (along the line in (b)). The measured depth indicates a PDA film thickness of about 10–25 nm on the surface. This thin coating contains the imprinted binding sites for TGF-β while preserving the PhC optical function [1].

3.2.3 Final Device Assembly and Optical Interrogation System

Following imprinting, the MIP-functionalized PhC sensor chip was incorporated into a microfluidic flow cell for sample delivery and positioned within an optical readout setup [21]. A PDMS chamber was bonded to the chip to confine liquid samples over the photonic crystal and enable controlled analyte exposure. The PDMS structure included an opening (well) of approximately 1 mm², aligned with the PhC sensor area, and featured inlet and outlet ports for solution delivery. This configuration creates a miniaturized flow cell over the sensor, requiring only 60 µL of sample to fully cover the active region. A sketch of the assembled device and a photograph are shown in

Figure 3.6a and 3.6b respectively. The PDMS chamber (transparent) allows optical access from the top. The simple and cost-effective integration approach enables the chip to function as a reusable sensing unit.

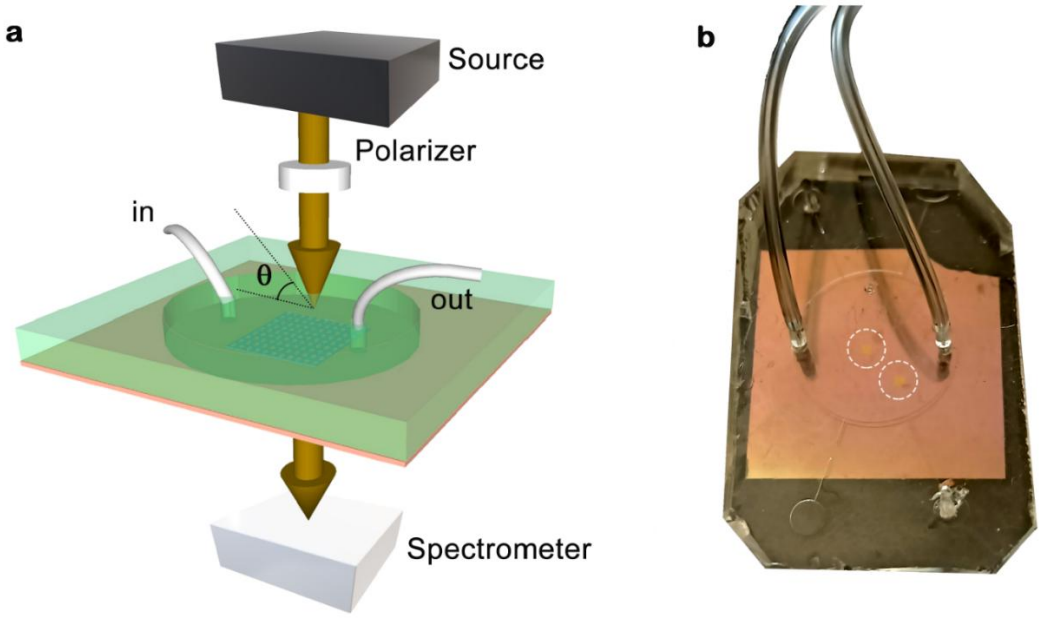

Figure 3.6: Device assembly and optical measurement setup. a) Schematic layout of the PhCS integrated in the microfluidic chamber and basic characterization setup. θ is the incident angle. b) Image of the final device, dotted circles indicate the PhCS areas [1].

For optical interrogation, an angle-resolved spectroscopy system is utilized. The chip (with PDMS cell) was placed on a computer-controlled rotation stage (goniometer) that can vary the incident angle θ of a collimated light beam with 0.01° precision [12]. The sensor with a broadband supercontinuum laser (NKT SuperK EXTREME) covering 400–2400 nm was illuminated. The beam was polarized in s-polarization to efficiently excite the quasi-BIC modes. The light transmitted through the PhC was fiber-coupled into a spectrometer (Ocean Optics HR4000, 0.25 nm resolution). By scanning the incident angle θ and recording spectra, a 2D map of intensity vs. wavelength and angle was obtained, essentially the dispersion band diagram of the device. In each measurement, the signature of the BIC resonance appears as a sharp dip in transmission (or peak in reflection) that shifts in wavelength when TGF-β is bound.

For practical sensing experiments, it is unnecessary to map the entire band diagram; instead, the incident angle is typically fixed near the resonance, and the shift in the resonant peak wavelength is monitored over time. The goniometer and spectrometer were synchronized and automated via a custom MATLAB program.

All measurements were done at room temperature. Before introducing any analyte, the sensor was stabilized in pure buffer and a baseline spectrum recorded. Then, known concentrations of TGF-β (in PBS or artificial saliva) were injected into the chamber sequentially. Following each exposure, which typically lasted about 30 minutes to reach binding equilibrium, the solution was left undisturbed during incubation, after which the chamber was rinsed with clean buffer to remove unbound molecules before measuring the resonance position. The PDMS well was reusable after cleaning, and the MIP layer demonstrated stability and reusability over numerous binding and elution cycles.

The interrogation angle was selected so that, under baseline conditions (without analyte), the resonance was slightly off normal incidence, producing a distinct peak. For the devices, an incidence angle of approximately 0.3° was optimal. At this angle, the resonance quality factor (Q) remained very high, on the order of several thousand. The baseline resonance wavelength was near 800 nm. Upon TGF-β binding, the resonance wavelength redshifted, and this shift ($\Delta\lambda$) was monitored as the sensor response.

This experimental setup offered two complementary measurement approaches. The first one was spectral shift readout, tracking the change in resonance wavelength ($\Delta\lambda$) at a fixed incident angle following each incubation. The second one was angular shift readout, where, at a fixed wavelength, the change in incidence angle ($\Delta\theta$) required to maximize the resonance peak is monitored. This method is similar to optical lever detection and can provide higher sensitivity under certain conditions.

3.3. Results and Discussion: Performance and Validation of the MIP-BIC Sensor

3.3.1 Transduction Mechanism and Sensing Principle

The MIP-BIC sensor converts TGF-β binding into an optical signal by shifting a high-Q photonic resonance. As target molecules fill cavities in the MIP layer, the local refractive index increases, causing a redshift ($\Delta\lambda$) proportional to the bound concentration [25][26]. This label-free refractometric approach enables quantitative detection, with the narrow resonance [27].

To illustrate the sensing principle, Figure 3.7 shows the optical response of the sensor before and after exposure to a low TGF-β concentration (100 fM). In this example, the reflectance intensity is plotted as a function of wavelength and angle around the resonance region. Initially (pristine MIP, no analyte), the quasi-BIC modes appear as characteristic Fano line-shapes in the 2D dispersion (Figure 3.7a, blue regions indicate low reflectance at the resonant wavelengths). After incubating

the sensor with 100 fM TGF-β, the resonances shift to slightly longer wavelengths (Figure 3.7a). By subtracting the pristine from the exposed spectra, a clear difference band diagram is obtained, highlighting the changes. This confirms that even at 100 fM (0.1 pM), there is a measurable spectral shift of the high-Q modes due to analyte binding.

To more rigorously capture the tiny resonance shift, the spectrum was sampled over multiple incidence angles near normal, and the peak positions were statistically analyzed. Figure 3.7b shows the distribution of measured peak wavelength shifts at 100 fM, compiled from N = 1200 angular spectra in the range –10° to +10° (around Γ). The distribution is centered at an average shift $\Delta\lambda_\mu$ = 2.8 nm with a standard deviation σ = 0.7 nm. This indicates the resonance redshift is consistently around 3 nm at 100 fM. Notably, averaging over a wide angular range significantly reduces noise, improving shift accuracy. By fitting multiple spectra simultaneously, the full band diagram provides a reliable determination of $\Delta\lambda$.

TGF-β binding not only shifts the resonance wavelength but also alters its angular dispersion. The added mass slightly changes the band curvature, shifting the resonance angle at a fixed wavelength. This serves as an angular transduction mechanism, similar to an optical lever. Figure 3.7c demonstrates this: at 797 nm wavelength, the reflectance peak occurred at a certain angle before exposure (black points) and at a shifted angle after exposure to 100 fM (red points). The angular shift here was $\Delta\theta$ = 0.26°, corresponding to roughly 50 times the goniometer positioning accuracy of 0.005°. While a fraction of a degree may seem small, modern position-sensitive goniometers can detect changes on the order of 10^{-5}–10^{-4} radians (0.001°–0.006°), so a shift of 0.26° is significant.

Therefore, the MIP-BIC sensor detects binding events via two mechanisms: The first one is spectral Domain: Binding shifts the resonance wavelength ($\Delta\lambda$). Narrow linewidths allow detection of even small shifts, enhancing sensitivity. The second one is angular Domain: Binding also causes an angular shift ($\Delta\theta$) at fixed wavelength. This complementary method enables high-resolution detection using precise angle measurements [24].

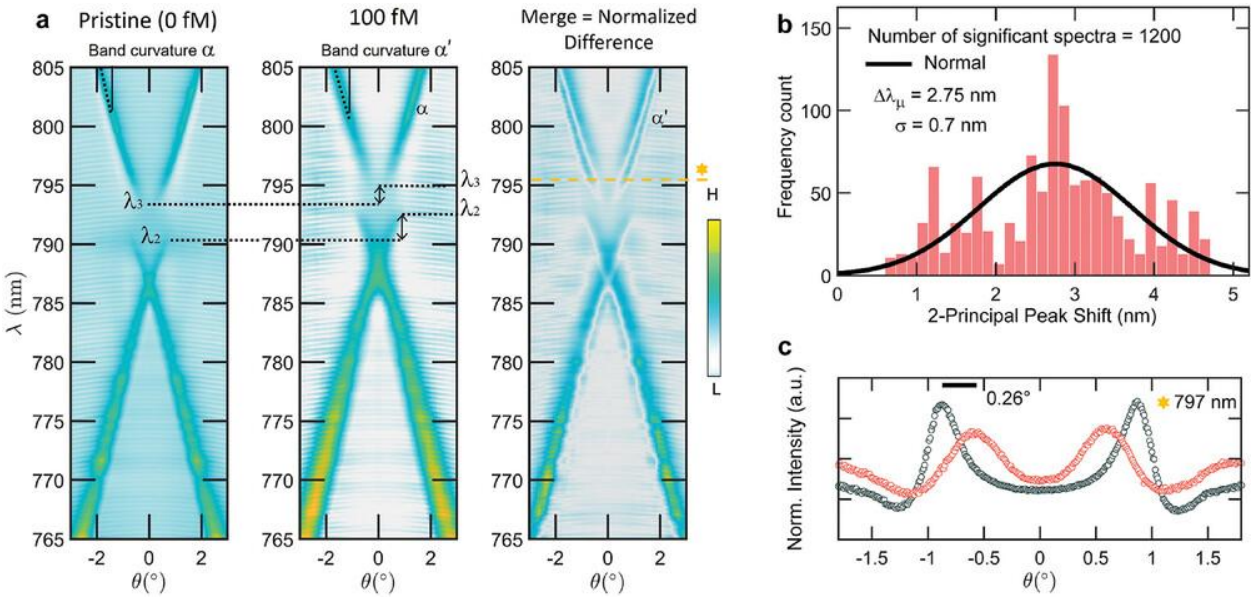

Figure 3.7: a) Comparison of the reflectance bands before (pristine) and after incubation with TGF-*β* concentration C = 100 fM, and normalized difference band diagram indicated as merge. b) Representative distribution of the peak shift obtained for C = 100 fM for the high-Q factor modes, evaluated for the experimental angles selected as relevant (N = 1200 out of 2001 total, range (− 10°, 10°), resolution 0.01°. c) Representative comparison of the angular peak shift before (black dots) and after (red dots) incubation at C = 100 fM: the spectral redshift of the modes with the molecular adsorption implies also a shift of the angle at which the spectrum is peaked at a fixed probed wavelength (here 797 nm) [1].

3.3.2 Evolution of the Resonance at Trace TGF-β Concentrations

With an angle-resolved optical system, changes in the photonic resonance upon exposure of the sensor to extremely low concentrations of TGF-β was observed. Figure 3.8 presents detailed data after incubating the MIP-coated PhC with 1 pM TGF-β. A pronounced redshift of the quasi-BIC resonance is observed in the reflectance spectra, indicating that binding of TGF-β increases the effective refractive index of the MIP layer. The resonance dip shifts toward longer wavelengths by several nanometers (as seen by the peak shift in Figure 3.8a) and experiences slight broadening due to the perturbation. Correspondingly, the quality factor decreases from its ideal value to approximately 262 at 1 pM, which is about a one-order-of-magnitude drop compared to the pristine quasi-BIC, yet still clearly resolvable. This reduction in Q is anticipated, as increased analyte loading introduces optical losses and scattering, for example, through polymer inhomogeneities and molecular absorption, which broaden the resonance linewidth. Nevertheless, a Q factor in the several hundreds remains relatively high, ensuring that the resonance stays sharp and clearly detectable even at 1 pM. The angle-resolved band diagram (Figure 3.8b) reveals a redshift in the high-Q mode dispersion upon TGF-β binding. In practical terms, TGF-β binding causes the resonance peak to redshift at a fixed angle and shift in angle at a fixed wavelength, similar to a

slight beam deflection. As shown in Figure 3.8c, after binding, the resonance appears at a slightly different angle, indicating a measurable angular detuning. Figures 3.8d and 3.8e zoom into a single resonance peak and a single angular scan, respectively, to highlight these changes: the resonance peak in Figure 3.8d is slightly broader and red-shifted under 1 pM TGF-β, and the angular reflectance profile in Figure 3.8e shows the peak position has shifted away from the center compared to the blank. These results show that even at picomolar TGF-β levels, the MIP-BIC sensor delivers a clear optical response, with a narrow resonance enabling high signal-to-noise detection, which is crucial for trace detection.

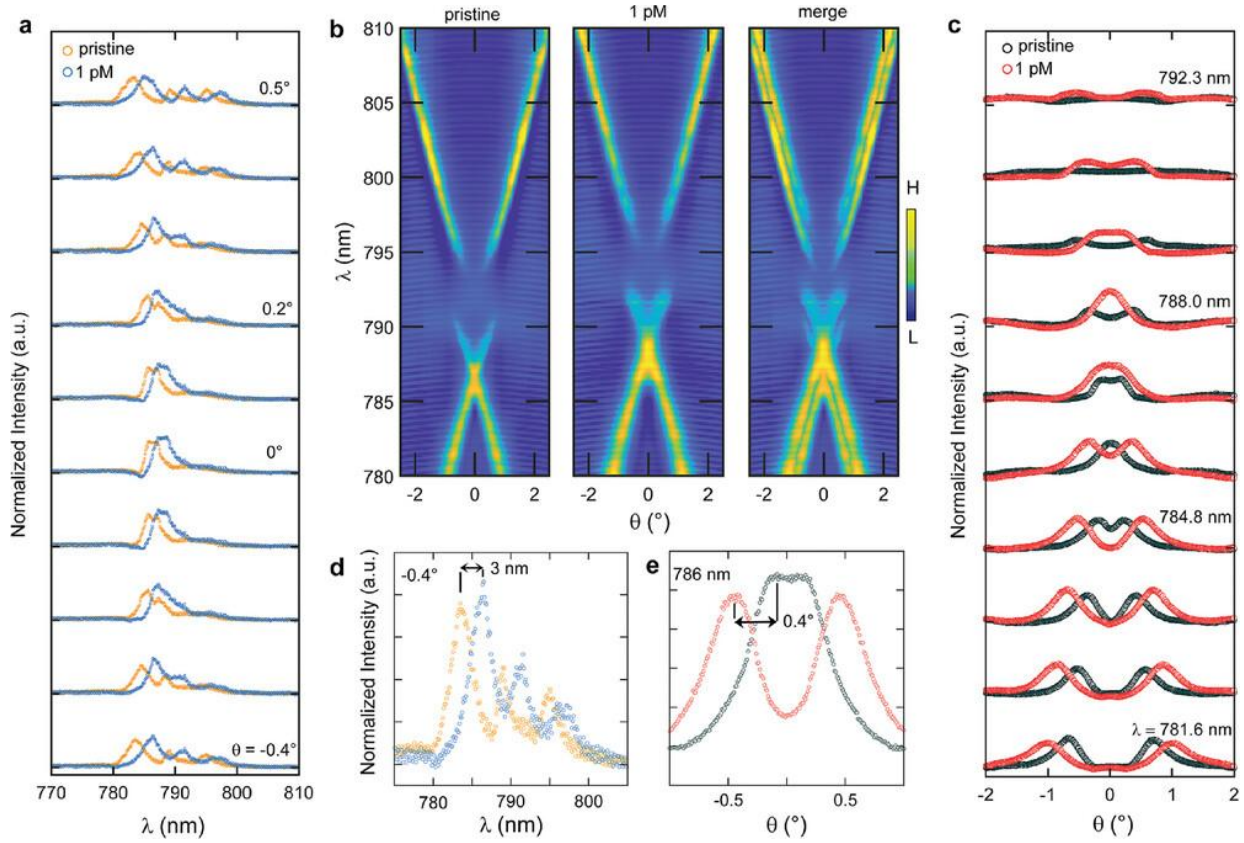

Figure 3.8: a) Comparison of the evolution of the reflectance spectra (vertical cross-section of the band diagram) at representative angles near normal incidence at C = 1pM. b) Comparison of the full experimental band diagrams highlighting the large variation detected with TGF-β absorption. c) Horizontal cross-sections of the band diagram at fixed wavelengths, denoting the angular shift of the peak resonance as a result of the redshift of the resonant modes. d) Zoom of a reflectance spectrum from (a). e) Zoom of a horizontal angular cross-section from (c) [1].

Figure 3.9 explores even lower TGF-β concentrations (50 fM and 10 fM), testing the sensor limits. At 50 fM, where binding causes minimal perturbation, the resonance remains detectable and

slightly red-shifted (Figure 3.9a). Fitting the reflectance dip to a Fano lineshape yields an experimental Q of 610, sharper than at 1 pM due to lower damping. This high-Q, narrow linewidth enables precise measurement of small wavelength shifts. Indeed, Figures 3.9b and 3.9c show that even the slight refractive index change from 50 fM TGF-β causes a measurable spectral shift across various angles, thanks to the steep slopes of the high-Q resonance peak. The sensor noise baseline was measured to verify its detection limits. The system wavelength noise is 0.1 nm, and the angular noise is 0.01°, resulting from instrument resolution and fitting uncertainties. At 50 fM TGF-β, the spectral shift is on the order of tenths of a nanometer (just above the wavelength noise) while the angular shift is approximately 0.03° (Figure 3.9d), about three times the angular noise, defining the detection limit for the angle-based readout. Despite this, the spectral shift remains reliable, as the high-Q resonance produces a distinct, measurable change. This demonstrates the BIC sensor exceptional sensitivity, enabling label-free detection down to 50 fM.

At 10 fM TGF-β, the sensor approaches its detection limit. Figure 3.9e shows the resonance barely shifts from the blank but remains extremely sharp, with a Q-factor of 980, close to the device ideal. This is expected, as so few molecules are bound that the optical properties stay nearly unchanged. Still, even a tiny refractive index increase leads to a detectable spectral shift. At a fixed angle, a 0.3 nm redshift is observed, which exceeds the wavelength noise level of 0.1 nm (Figure 3.9f), confirming the spectral limit of detection at 10 fM.

In contrast, the angular shift (0.01°, Figure 3.9g) is equivalent to the system angular noise, making angle-based detection unreliable at this level. This limitation stems from the readout method, not the sensor itself. With higher-resolution techniques such as optical lever tracking, angular shifts of 0.01° or smaller could be confidently resolved. Nonetheless, the spectral data establish 10 fM as the LOD for TGF-β without any biochemical amplification. This underscores the powerful synergy between the MIP selective binding and the BIC sharp optical resonance.

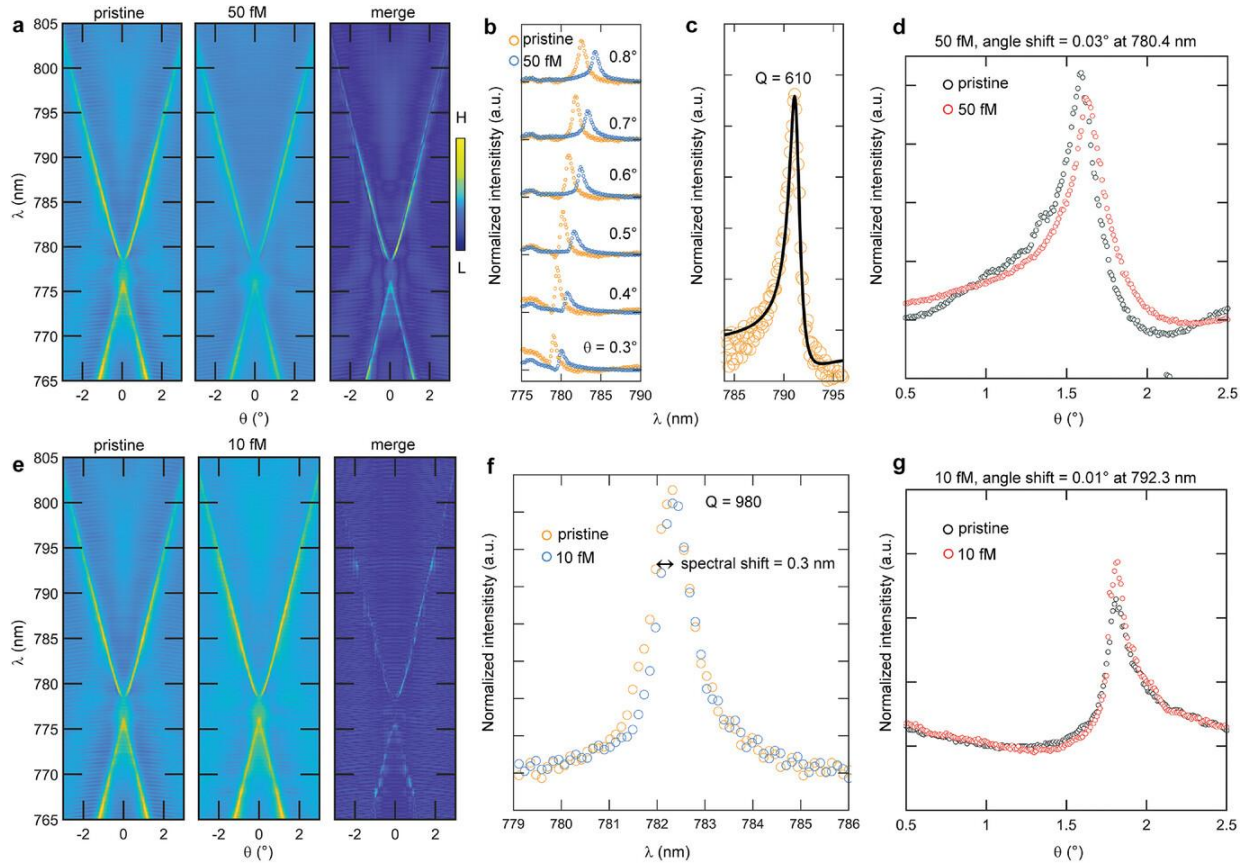

Figure 3.9: a) Full reflectance TE band diagram comparison at C = 50 fM. b) Comparison at representative spectra at fixed angle for C = 50 fM, and experimental Q-factor evaluation in (c) fitted as a Fano resonance (black line). d) Representative horizontal angular cross-section denoting a limited angular peak shift of 0.03°. e) Full reflectance TE band diagram comparison at C = 10 fM. f) Comparison of more representative spectra at a fixed angle for C = 10 fM, having large experimental Q-factor as less perturbed by the molecular layer, and also pointing out the LOD of the sensor. g) Representative horizontal angular cross-section denoting the attainment of the LOD also in the angular peak shift, 0.01° [1].

3.3.3 Sensor Performance Evaluation using Dual Readout Strategies

Sensor performance (sensitivity, detection limit, and dynamic range) was assessed using two readout methods which are resonance wavelength shifts (spectral readout) and angular shifts at fixed wavelength (angular readout). Both exploit the same principle but offer different practical benefits.

3.3.3.1 Refractometric Spectral Shift Readout

For the spectral readout, the resonance peak wavelength was recorded as a function of TGF-β concentration C. Measurements were conducted in phosphate-buffered saline (PBS) as a simple matrix for initial calibration. Figure 3.10a shows the calibration curve: each point represents the mean resonance shift Δλ (from baseline) after exposing the sensor to a given TGF-β concentration.

The square points are data in PBS; the diamond points are data for spiked artificial saliva. It is clear that they lie on the same curve, indicating consistent response even in saliva.

At the lowest tested concentration (1 fM), the spectral shift observed was on the order of the noise level, but by 10 fM a clear positive shift (0.3 nm) was measurable above the baseline noise. The response increases steadily with concentration, reaching about 5 nm shift at 10 pM. Crucially, the sensor limit of detection via spectral shift was determined to be 10 fM. The LOD is defined as the concentration that produces a signal equal to 3× the standard deviation of the blank (noise) [15]. The blank noise was measured by performing repeated baseline readings; it corresponds to about 0.1 nm in wavelength fluctuation (due to instrument resolution and any drift). A 10 fM TGF-β exposure yielded a shift of 0.3 nm, which is roughly 3× the noise, thus confidently detectable above noise threshold. Indeed, in Figure 3.10a, 10 fM is the lowest point clearly above the error bars.

The sensor resolution in concentration (smallest step discernible) is even better in certain ranges. By focusing on the steep portion of the calibration curve (around 0.1–1 pM, where the slope is highest), one can resolve changes on the order of 0.01–0.1 pM. The local sensitivity at 100 fM was estimated as $s = 1.4 \times 10^{-2}$ nm/fM. The spectral mode of the sensor supports a dynamic range from 0.01 pM to around 10 pM, effectively covering more than three orders of magnitude. Above 10 pM, the response curve flattens as the MIP approaches saturation. This upper range is still well above physiological TGF-β levels, so it suffices for biomarker detection purposes. If needed, diluting samples could extend the dynamic range on the high end.

It is noteworthy that at a concentration of C = 0.1 pM (0.004 ng/mL), the sensor already achieves a substantial portion of its maximum signal, demonstrating an exceptionally sensitive detection range. This level is approximately 1000 times lower than the clinically relevant threshold of 5 ng/mL [28]. In practical terms, the proposed sensor could be used to screen for oral cancer risk by detecting subtle increases in TGF-β well before they reach pathological threshold, or to monitor treatment by measuring reductions from elevated levels with high precision. Moreover, because only a very small volume (60 µL) is required per measurement and no reagents are consumed (label-free), multiple biomarkers could be sequentially detected from the same sample. The high sensitivity also allows for significant sample dilution if needed to mitigate matrix effects.

3.3.3.2 High-Resolution Angular Shift Readout (Optical Lever Analogue)

The sensor performance using the angular readout method are examined next. Instead of looking at wavelength shifts, the detection wavelength is fixed and the resonance angle shifts with concentration are measured. The motivation for this approach is that angular changes can, in

principle, be measured with extremely fine precision. For the device, the angular readout is implemented by scanning the goniometer at a set wavelength and noting the angle at which maximum transmission (or minimum reflection) occurs for the resonance.

Figure 3.10c presents the angular peak shift versus TGF-β concentration in PBS medium. It is clear that in the most relevant range of around 10–100 pM (where clinical samples would lie), the angular readout provides a highly sensitive response: the curve is steep in that region, indicating that small concentration differences produce measurable angle changes. In fact, the sensor shows an exponentially sensitive angular response in the tens of pM range, which is crucial for distinguishing normal vs. cancer patient levels (typically 15 pM vs. 25 pM) [28].

One remarkable aspect of the angular readout is the fine resolution achieved. The error bars in Figure 3.10c are around 0.01°, which corresponds to the step accuracy of the goniometer. In the current setup, a concentration resolution of approximately 0.5 pM was demonstrated using the angular method, within the range of maximum slope in Figure 3.10c. This estimation is based on an angular resolution of 0.05°, corresponding to the sensor exponential response. The angular readout thus provides around a two-order-of-magnitude improvement in resolution relative to clinical requirements, outperforming the spectral readout at higher concentrations where the spectral response tends to plateau.

At very low concentrations (below 1 pM), the angular shift becomes minimal, around 0.01° or less at 10 fM, which approaches the goniometer noise threshold. In this range, the spectral method proved more effective for detecting changes. In fact, depending only on angular detuning at very low concentrations (such as 10 fM) was unreliable given the current angular resolution. The spectral method, by contrast, clearly identified 10 fM. The dual-readout strategy, therefore, enables full-range coverage: spectral shifts detect ultra-low concentrations, while angular shifts provide precise measurements at higher levels.

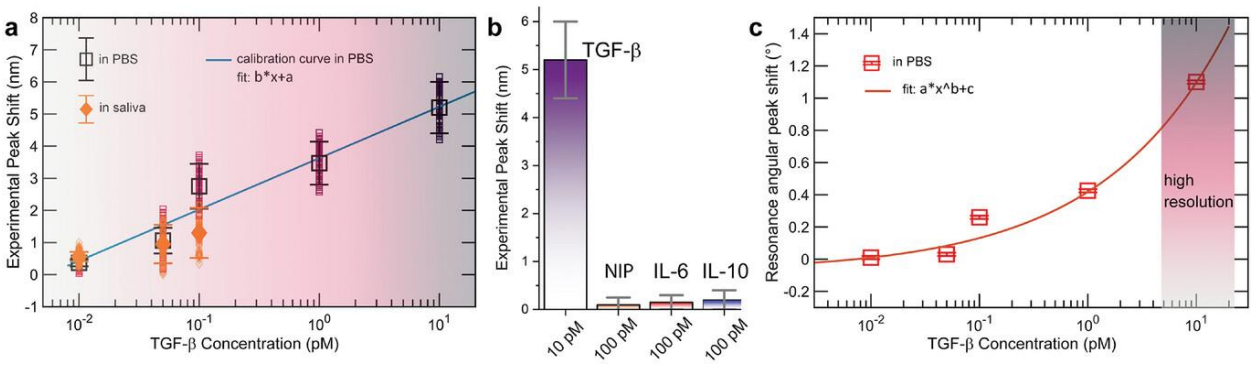

Figure 3.10: Sensor calibration and performance with dual readouts. a) Calibration of the spectral peak response versus analyte concentration. Square points represent experimental data for TGF-β in PBS, while

diamond points show measurements from spiked saliva projected onto the calibration curve. For each concentration, spectral data from 1200 sampled angles are presented along with the mean and standard deviation. Error bars indicate the standard deviation of peak shift distributions. The solid line shows the linear fit of the calibration. b) Specificity of the MIP-BIC response: a positive shift above the LOD is observed at the physiological TGF-β level of 10 pM in saliva. In contrast, no signal is detected for 100 pM of competing molecules (IL-6 and IL-10). The control NIP-BIC platform, which is insensitive to TGF-β, also shows no response when exposed to 100 pM TGF-β. Error bars represent the standard deviation of MIP TGF-β measurements, while for controls (NIP, IL-6, IL-10) they indicate the maximum instrument error, assumed as the spectrometer resolution of 0.25 nm. c) Calibration of angular peak shift with analyte concentration in PBS: the angular peak shift shows an exponential sensitivity with high resolution across physiological concentration ranges, enabling precise discrimination of TGF-β levels. Error bars of 0.01° correspond to twice the goniometer positioning accuracy (0.005°), as specified by the manufacturer [1].

3.3.4 Selectivity and Specificity Analysis

Selectivity, the capability to accurately identify the target analyte despite the presence of interfering substances, is a key performance metric for any biosensor. In the case of proposed MIP-BIC sensor, this selectivity is achieved through the molecularly imprinted polymer precise recognition of TGF-β. Multiple tests were performed to confirm that the sensor signal results from specific TGF-β binding to the MIP sites, rather than from non-specific adsorption or other interferences.

3.3.4.1 Cross-Reactivity Study

Initially, the sensor reaction to other biomolecules that might be found in saliva and could cause cross-reactivity was evaluated. Interleukin-6 (IL-6) and interleukin-10 (IL-10) were selected as representative interfering cytokines, as they are of similar size to TGF-β and might coexist in oral fluids. The MIP-coated sensor was exposed to IL-6 and IL-10 (separately) at a high concentration of 100 pM (which is 10× higher than the highest TGF-β level tested). The sensor exhibited no notable spectral shift for IL-6 or IL-10, with reflectance spectra after incubation remaining nearly identical to the baseline. In contrast, exposure to 10 pM TGF-β on the same sensor caused a distinct shift.

This outcome is illustrated in Figure 3.10b: the bars for IL-6 and IL-10 remain near baseline, indicating cross-reactivity below 5% (Cross-reactivity is calculated as the ratio of the non-specific shift to the specific TGF-β shift at the same concentration). This negligible response suggests that the MIP binding sites have a strong preference for TGF-β shape and functionality, and do not appreciably bind these other cytokines even at higher concentrations. In practical terms, this means the sensor would not give false positives if, for example, IL-6 levels were elevated in patient saliva.

3.3.4.2 Negative Control Validation

To further confirm that the sensor optical response is indeed due to the imprinting effect, control experiments were performed using a non-imprinted polymer under identical conditions. A Si_3N_4 PhC chip was coated with a polydopamine film in the absence of TGF-β template (same thickness 20 nm), creating a polymer that should lack the specific cavities for TGF-β. The NIP-coated sensor was then exposed to 100 pM TGF-β, and the resonance was monitored. The NIP sensor exhibited no measurable peak shift upon TGF-β injection. Essentially, the resonance remained at the same wavelength as before, indicating that TGF-β did not specifically bind or induce a refractive index change in the non-imprinted PDA. Physical adsorption of TGF-β on the NIP was minimal and did not shift the high-Q mode, highlighting that specific binding to the MIP templated cavities enables detection.

The magnitude of the sensor response on MIP vs. NIP was also compared by calculating the imprinting factor, determined by comparing the wavelength shift induced on the MIP to that on a corresponding NIP for the same concentration. Using 10 pM TGF-β as a benchmark, the imprinting factor came out to be extremely high (52). Essentially, the MIP sensor response was 52 times greater than the NIP. This highlights the effectiveness of the molecular imprinting in conferring selectivity.

3.3.5 Validation in a Complex Biological Matrix: TGF-β Detection in Saliva

After the sensor sensitivity and specificity were established under controlled conditions, its performance was validated in human saliva, a complex and clinically relevant medium. Saliva, particularly in oral cancer patients, is known to contain TGF-β along with various proteins, enzymes, and electrolytes, and is considered a challenging, non-Newtonian matrix. For testing, artificial saliva was used and spiked with known concentrations of TGF-β to simulate real conditions.

The MIP-coated sensor chip was exposed to artificial saliva samples spiked with varying concentrations of TGF-β, ranging from 10 fM to 100 fM, sequentially, with thorough rinsing between each exposure. The optical interrogation was done in the same manner as with PBS. The resonance shifts observed in saliva were then compared to the PBS calibration curve.

The results, plotted as diamond points in Figure 3.10a, show that the saliva data points lie on the same calibration curve as the PBS data. In other words, the sensor response in the saliva matrix was consistent with that in buffer. It can also be observed that the presence of other saliva constituents

did not significantly alter the sensor sensitivity or baseline. This stability is likely due to minimal non-specific adsorption on the MIP surface, attributed to the hydrophilic and relatively inert nature of PDA, as well as the effective removal of loosely bound species during the polymer blocking and washing steps. To assess whether saliva caused additional noise or measurement uncertainty, error bars have been analyzed, which were similar to those observed in PBS. This indicates that the presence of saliva did not affect the measurement precision.

The sensor detected TGF-β in saliva down to 10 fM (0.004 ng/mL), far below typical levels in healthy (5–30 ng/mL) and patient saliva (7–88 ng/mL) [28]. In fact, A limit of detection of 10 fM in spiked saliva was demonstrated using spectral readout, surpassing the best reported immunosensors for TGF-β in saliva, which had a detection limit of around 20 fM by electrochemical immunoassay. Reaching this sensitivity without any sample pretreatment or amplification strongly validates the proposed approach. Additionally, with high-resolution angular readout, the sensor was able to detect differences as small as 0.5 pM (0.025 ng/mL) at physiological levels. This precision enables reliable distinction between TGF-β levels typical of healthy and diseased individuals, such as 15 ng/mL versus 25 ng/mL, a key diagnostic threshold [28].

The sensor demonstrated strong stability in saliva, with the PDA MIP layer staying intact after repeated exposures. Fouling was effectively reduced by rinsing, allowing the baseline to be consistently regained, which supports both repeatability and potential sensor reuse. Having demonstrated the sensor performance in a realistic context, a comparison with current state-of-the-art TGF-β biosensors will be made in the next section.

3.4. Comparative Analysis, Conclusions, and Future Outlook

3.4.1 Benchmarking Against State-of-the-Art TGF-β Biosensors

It is instructive to compare the performance of the MIP-BIC sensor with existing TGF-β detection technologies reported in the literature. Table 3.1 summarizes key metrics of various TGF-β biosensors, including the MIP-BIC sensor (last row). The table covers conventional immunoassays (ELISA), electrochemical and optical sensors, detailing their limits of detection, dynamic ranges, detection techniques, biorecognition elements, and sample types.

The MIP-BIC sensor clearly outperforms most existing methods in terms of sensitivity. The LOD of 10 fM (0.48 pg/mL) is over an order of magnitude lower than the best immunosensors (0.95 pg/mL by Sanchez-Tirado et al. using an ELISA-based amperometric assay), and significantly lower than other optical or electrochemical sensors (which are generally in the pM range). Notably, the MIP-

BIC sensor achieved this without any labeling or signal amplification, whereas many others require enzyme labels, fluorescent tags, or nanoparticles. This highlights the power of combining the BIC transducer with MIP recognition [29].

Table 3.1: Comparison between the MIP-BIC sensor and other biosensors for TGF-β detection. Values of LOD and range are as reported in respective references [1].

Reference	LOD	Detection Range	Detection Method	Biorecognition Element	Sample Matrix
Sanchez-Tirado et al. (2017) [29]	0.95 pg/mL	2.5–1000 pg/mL	Amperometry	Antibodies	Saliva
Son et al. (2017) [30]	211 pM	0–300 pM	Fluorescence	Antibodies	culture medium
Yao et al. (2016) [31]	0.570 ng/mL	1–1000 ng/mL	Impedance	Antibodies	clinical Serum
Siciliano et al. (2023) [23]	0.09 ng/mL	0.5–20 ng/mL	Voltammetry	MIP	Saliva
Sanchez-Tirado et al. (2017) [32]	10 pg/mL	15–3000 pg/mL	Amperometry	Antibodies	Urine
Dai et al. (2019) [33]	0.2 nM	1–50 nM	Electrochemical	Cas12a crRNA	Protein sample
Park et al. (2021) [34]	1.3 pM	0.1–10000 ng/mL	Optical	Gold Nanoprobe	Cell culture medium
Fang et al. (2022) [21]	–	0–20 ng/mL	Optical	PDMS sheet	Breast cancer cell
This work (MIP-BIC)	10 fM (0.48 pg/mL)	0.001–10 pM	Optical	MIP	Saliva

Some methods, like Park et al. LSPR nanoprobe, offer a broader dynamic range up to nM levels but lose sensitivity at the low end. In contrast, the MIP-BIC sensor range targets ultra-low

concentrations, which is suitable for diagnostics focused on threshold detection [28]. The dual angular readout also allows detection in the range of 10 pM with high precision [34].

Another key advantage is the simplicity and speed of the detection method. Unlike ELISA, which is time-consuming and relies on costly antibodies and labels, this sensor provides label-free, real-time results within minutes. It requires only 60 µL of sample, compared to the much larger volumes needed for ELISA. On-chip integration also allows for potential multiplexing without significantly increasing sample volume [23].

Cost and reusability are also important factors. The robust MIP layer can be regenerated by simple washing, unlike antibodies which tend to degrade or hold onto antigens. The MIP-BIC sensor maintained stable performance over repeated use, highlighting its potential as a low-cost, reusable chip for practical applications.

Proposed approach aligns with the trend of label-free optical biosensors like SPR, which also offer real-time detection and kinetic analysis. However, SPR typically has higher LODs (high pM to nM), requires metal coatings, and is sensitive to bulk refractive index changes. In contrast, the dielectric BIC sensor avoids metal losses and, with the MIP layer, selectively responds to specific binding. It also addresses SPR limitations, offering better reproducibility without complex regeneration and higher sensitivity due to the BIC higher Q-factor [18][19].

Electrochemical biosensors provide excellent sensitivity and portability, with leading TGF-β sensors achieving LODs around 20 fM. However, they typically require intricate nanostructured electrodes or antibody labels, increasing fabrication complexity. Conversely, this sensor employs scalable lithography and simple polymerization, concentrating complexity in the initial fabrication instead of the assay preparation [33].

Currently, the readout uses a spectrometer and rotation stage, suitable for labs but requiring miniaturization for point-of-care use. However, this is feasible with modern photonics, such as fixed-angle incidence and fringe imaging or intensity-based detection.

3.4.2 Conclusion and Summary of Major Findings

This chapter presents a novel biosensing platform that integrates a high-Q photonic crystal slab with a molecularly imprinted polymer for the selective detection of TGF-β. The developed MIP-BIC hybrid sensor demonstrates several significant advances in both sensitivity and practicality.

The sensor achieved ultrasensitive, femtomolar-level detection of TGF-β, with a limit of detection around 10 fM, the lowest reported to date for a label-free TGF-β biosensor. This exceptional performance stems from the ultranarrow quasi-BIC resonance in the photonic crystal slab, which enhances light–matter interaction.

High specificity was attained through the use of a polydopamine-based molecularly imprinted polymer, which provided high-affinity binding to TGF-β without the need for biological receptors [17]. The MIP layer exhibited minimal cross-reactivity, and results from non-imprinted controls confirmed the selective recognition of the target molecule. This receptor-free approach simplifies surface chemistry, enhances stability, and allows sensor reusability.

A dual-readout mechanism was also introduced, enabling simultaneous measurement of spectral and angular shifts in the BIC resonance. The wavelength shift showed a linear response at ultralow concentrations, while the angular shift improved precision at higher concentrations. Together, these modes extended the sensor dynamic range and leveraged the unique dispersion characteristics of the BIC resonance for superior performance.

The sensor effectiveness was further validated in a real-matrix test using artificial saliva, where it maintained a detection limit of 10 fM consistent with buffer measurements. This confirms the platform potential for non-invasive diagnostics, particularly in early oral cancer detection, as its sensitivity far surpasses clinically relevant thresholds [28].

The MIP-BIC hybrid sensor outperformed existing TGF-β biosensors by achieving femtomolar detection without labels or complex assay steps. Its integrated design combines optical transduction and molecular recognition within a single platform, eliminating the need for antibodies or sandwich configurations. By uniting a nanostructured photonic slab with a synthetic polymer layer, the sensor offers a scalable, robust, and compact solution for next-generation biosensing applications.

3.5. References

[1] G. Zito *et al.*, “Molecularly Imprinted Polymer Sensor Empowered by Bound States in the Continuum for Selective Trace-Detection of TGF-beta,” *Advanced Science*, vol. 11, no. 41, Nov. 2024, doi: 10.1002/advs.202401843.

[2] B. Miranda *et al.*, “All-dielectric optical biosensors based on bound states in the continuum: a new paradigm in healthcare and food quality assessment,” in *Metamaterials, Metadevices,*

and Metasystems 2024, N. Engheta, M. A. Noginov, and N. I. Zheludev, Eds., SPIE, Oct. 2024, p. 69. doi: 10.1117/12.3028102.

[3] J. Ferlay *et al.*, "Cancer incidence and mortality worldwide: Sources, methods and major patterns in GLOBOCAN 2012," *Int J Cancer*, vol. 136, no. 5, Mar. 2015, doi: 10.1002/ijc.29210.

[4] Y. Guo, T. Xu, Y. Chai, and F. Chen, "TGF-β Signaling in Progression of Oral Cancer," *Int J Mol Sci*, vol. 24, no. 12, p. 10263, Jun. 2023, doi: 10.3390/ijms241210263.

[5] E. N. Bulgakov and A. F. Sadreev, "Bound states in the continuum in photonic waveguides inspired by defects," *Phys Rev B*, vol. 78, no. 7, p. 075105, Aug. 2008, doi: 10.1103/PhysRevB.78.075105.

[6] V. Mocella and S. Romano, "Giant field enhancement in photonic resonant lattices," *Phys Rev B*, vol. 92, no. 15, p. 155117, Oct. 2015, doi: 10.1103/PhysRevB.92.155117.

[7] G. Zito *et al.*, "Observation of spin-polarized directive coupling of light at bound states in the continuum," *Optica*, vol. 6, no. 10, p. 1305, Oct. 2019, doi: 10.1364/OPTICA.6.001305.

[8] G. K. Ali and K. M. Omer, "Molecular imprinted polymer combined with aptamer (MIP-aptamer) as a hybrid dual recognition element for bio(chemical) sensing applications. Review," *Talanta*, vol. 236, p. 122878, Jan. 2022, doi: 10.1016/j.talanta.2021.122878.

[9] L. Wang, M. Pagett, and W. Zhang, "Molecularly imprinted polymer (MIP) based electrochemical sensors and their recent advances in health applications," *Sensors and Actuators Reports*, vol. 5, p. 100153, Jun. 2023, doi: 10.1016/j.snr.2023.100153.

[10] G. Siciliano *et al.*, "Polydopamine-Coated Magnetic Iron Oxide Nanoparticles: From Design to Applications," *Nanomaterials*, vol. 12, no. 7, p. 1145, Mar. 2022, doi: 10.3390/nano12071145.

[11] W.-H. Zhou, C.-H. Lu, X.-C. Guo, F.-R. Chen, H.-H. Yang, and X.-R. Wang, "Mussel-inspired molecularly imprinted polymer coating superparamagnetic nanoparticles for protein recognition," *J. Mater. Chem.*, vol. 20, no. 5, pp. 880–883, 2010, doi: 10.1039/B916619J.

[12] S. Romano *et al.*, "Ultrasensitive Surface Refractive Index Imaging Based on Quasi-Bound States in the Continuum," *ACS Nano*, vol. 14, no. 11, pp. 15417–15427, Nov. 2020, doi: 10.1021/acsnano.0c06050.

[13] G. Zito *et al.*, "Label-free DNA biosensing by topological light confinement," *Nanophotonics*, vol. 10, no. 17, pp. 4279–4287, Nov. 2021, doi: 10.1515/nanoph-2021-0396.

[14] C. Schiattarella *et al.*, "High-Q photonic aptasensor based on avoided crossing bound states in the continuum and trace detection of ochratoxin A," *Biosens Bioelectron X*, vol. 12, p. 100262, Dec. 2022, doi: 10.1016/j.biosx.2022.100262.

[15] S. Romano *et al.*, “Tuning the exponential sensitivity of a bound-state-in-continuum optical sensor,” *Opt Express*, vol. 27, no. 13, p. 18776, Jun. 2019, doi: 10.1364/OE.27.018776.

[16] M. Kohri, “Progress in polydopamine-based melanin mimetic materials for structural color generation,” *Sci Technol Adv Mater*, vol. 21, no. 1, pp. 833–848, Jan. 2020, doi: 10.1080/14686996.2020.1852057.

[17] H. Zhao, M. L. Mayer, and P. Schuck, “Analysis of Protein Interactions with Picomolar Binding Affinity by Fluorescence-Detected Sedimentation Velocity,” *Anal Chem*, vol. 86, no. 6, pp. 3181–3187, Mar. 2014, doi: 10.1021/ac500093m.

[18] A. Aigner *et al.*, “Plasmonic bound states in the continuum to tailor light-matter coupling,” *Sci Adv*, vol. 8, no. 49, Dec. 2022, doi: 10.1126/sciadv.add4816.

[19] J. Wang, T. Weber, A. Aigner, S. A. Maier, and A. Tittl, “Mirror-Coupled Plasmonic Bound States in the Continuum for Tunable Perfect Absorption,” *Laser Photon Rev*, vol. 17, no. 11, Nov. 2023, doi: 10.1002/lpor.202300294.

[20] K. Koshelev, A. Bogdanov, and Y. Kivshar, “Meta-optics and bound states in the continuum,” *Sci Bull (Beijing)*, vol. 64, no. 12, pp. 836–842, Jun. 2019, doi: 10.1016/j.scib.2018.12.003.

[21] W. Fang, X. Lv, Z. Ma, J. Liu, W. Pei, and Z. Geng, “A Flexible Terahertz Metamaterial Biosensor for Cancer Cell Growth and Migration Detection,” *Micromachines (Basel)*, vol. 13, no. 4, p. 631, Apr. 2022, doi: 10.3390/mi13040631.

[22] G. Siciliano *et al.*, “Synthesis and Characterization of SPIONs Encapsulating Polydopamine Nanoparticles and Their Test for Aqueous Cu2+ Ion Removal,” *Materials*, vol. 16, no. 4, p. 1697, Feb. 2023, doi: 10.3390/ma16041697.

[23] G. Siciliano *et al.*, “Development of an MIP based electrochemical sensor for TGF-β1 detection and its application in liquid biopsy,” *Analyst*, vol. 148, no. 18, pp. 4447–4455, 2023, doi: 10.1039/D3AN00958K.

[24] M. J. Higgins *et al.*, “Noninvasive determination of optical lever sensitivity in atomic force microscopy,” *Review of Scientific Instruments*, vol. 77, no. 1, Jan. 2006, doi: 10.1063/1.2162455.

[25] E. De Tommasi *et al.*, “Frontiers of light manipulation in natural, metallic, and dielectric nanostructures,” *La Rivista del Nuovo Cimento*, vol. 44, no. 1, pp. 1–68, Jan. 2021, doi: 10.1007/s40766-021-00015-w.

[26] R. Gansch *et al.*, “Measurement of bound states in the continuum by a detector embedded in a photonic crystal,” *Light Sci Appl*, vol. 5, no. 9, pp. e16147–e16147, Apr. 2016, doi: 10.1038/lsa.2016.147.

[27] J. Gomis-Bresco, D. Artigas, and L. Torner, “Anisotropy-induced photonic bound states in the continuum,” *Nat Photonics*, vol. 11, no. 4, pp. 232–236, Apr. 2017, doi: 10.1038/nphoton.2017.31.

[28] M. Polz-Dacewicz, M. Strycharz-Dudziak, J. Dworzański, A. Stec, and J. Kocot, “Salivary and serum IL-10, TNF-α, TGF-β, VEGF levels in oropharyngeal squamous cell carcinoma and correlation with HPV and EBV infections,” *Infect Agent Cancer*, vol. 11, no. 1, p. 45, Dec. 2016, doi: 10.1186/s13027-016-0093-6.

[29] E. Sánchez-Tirado, L. M. Arellano, A. González-Cortés, P. Yáñez-Sedeño, F. Langa, and J. M. Pingarrón, “Viologen-functionalized single-walled carbon nanotubes as carrier nanotags for electrochemical immunosensing. Application to TGF-β1 cytokine,” *Biosens Bioelectron*, vol. 98, pp. 240–247, Dec. 2017, doi: 10.1016/j.bios.2017.06.063.

[30] K. J. Son, P. Gheibi, G. Stybayeva, A. Rahimian, and A. Revzin, “Detecting cell-secreted growth factors in microfluidic devices using bead-based biosensors,” *Microsyst Nanoeng*, vol. 3, no. 1, p. 17025, Jul. 2017, doi: 10.1038/micronano.2017.25.

[31] Y. Yao *et al.*, “Biomarkers of liver fibrosis detecting with electrochemical immunosensor on clinical serum,” *Sens Actuators B Chem*, vol. 222, pp. 127–132, Jan. 2016, doi: 10.1016/j.snb.2015.08.064.

[32] E. Sánchez-Tirado, G. Martínez-García, A. González-Cortés, P. Yáñez-Sedeño, and J. M. Pingarrón, “Electrochemical immunosensor for sensitive determination of transforming growth factor (TGF) - β1 in urine,” *Biosens Bioelectron*, vol. 88, pp. 9–14, Feb. 2017, doi: 10.1016/j.bios.2016.05.093.

[33] Y. Dai *et al.*, “Exploring the Trans-Cleavage Activity of CRISPR-Cas12a (cpf1) for the Development of a Universal Electrochemical Biosensor,” *Angewandte Chemie*, vol. 131, no. 48, pp. 17560–17566, Nov. 2019, doi: 10.1002/ange.201910772.

[34] J. Park, S. Lee, J. Choi, and I. Choi, “Extra- and Intracellular Monitoring of TGF-β Using Single Immunoplasmonic Nanoprobes,” *ACS Sens*, vol. 6, no. 5, pp. 1823–1830, May 2021, doi: 10.1021/acssensors.0c02723.

Chapter 4: Resolving SPARC–HSA Binding Kinetics with an Ultrasensitive Photonic Sensor Based on Bound States in the Continuum

4.1 Introduction

This chapter reports on the development and evaluation of an ultrasensitive photonic sensor based on bound states in the continuum for investigating Secreted Protein Acidic and Rich in Cysteine (SPARC)–Human Serum Albumin (HSA) binding kinetics. Consequently, here the BIC sensor is used to resolve the binding kinetics of a high-affinity complex in real time, unlike Chapter 3 which focused on the detection limit. The study was conducted through a collaborative effort between ISASI-CNR, the Department of Molecular Medicine and Medical Biotechnology at the University of Naples Federico II, and the Molecular Foundry at Lawrence Berkeley National Laboratory. The results have been published in Biosensors and Bioelectronics journal [1].

SPARC, also known as osteonectin, is a matricellular protein highly involved in cell–matrix interactions and tissue remodeling [2]. SPARC is widely expressed in remodeling tissues (bone, skin) and in various solid tumors, where its level often correlates with tumor progression and severity [3]. In cancer biology, SPARC modulates the extracellular matrix and influences angiogenesis and cell signaling, making it a key player in tumor microenvironment dynamics [4]. A notable aspect of SPARC role in oncology is its high-affinity binding to HSA [5][6]. HSA is the most abundant plasma protein and a critical transporter of nutrients, hormones, and drugs [7]. The SPARC–HSA interaction underpins the mechanism of albumin-bound drug delivery systems, such as nanoparticle albumin-bound (nab) paclitaxel, which preferentially accumulate in SPARC-expressing tumors [6]. Understanding this interaction has broad implications for improving drug delivery in cancer therapy and for unraveling how tumors exploit albumin as a nutrient source.

4.1.1 Motivation

SPARC serves not only as a biomarker for certain cancers but also actively influences tumor biology through its binding with albumin [8]. The ability of SPARC-rich tumors to bind to albumin impacts the distribution of albumin-bound chemotherapeutics in the body [9]. Thus, measuring SPARC levels has diagnostic value (such as in lung cancer [10]) and therapeutic significance.

However, beyond static expression levels, it is the dynamics of SPARC–HSA binding that govern how effectively a tumor can capture albumin. A strong binding affinity (quantified by a low dissociation constant K_D) means SPARC can retain albumin for longer durations, potentially enhancing drug uptake in the tumor stroma [8][9]. Traditional biomarker assays like ELISA provide endpoint concentrations but do not capture real-time interaction kinetics. The aim of this chapter is to move from merely detecting the presence of SPARC or HSA towards monitoring their interaction in real time. By doing so, insights are gained into how rapidly and tightly SPARC binds albumin under physiological conditions. Such knowledge could inform the design of albumin-based drug carriers and help predict a tumor response to albumin-bound chemotherapies.

4.1.2 Problem Statement and Chapter Objective

Characterizing SPARC–HSA binding kinetics is technically challenging due to the high affinity of the interaction and the correspondingly low K_D (in the nanomolar range or below) [11]. High-affinity interactions exhibit very slow dissociation, so detecting the minute changes during unbinding requires exceptional sensitivity [12]. Traditional SPR techniques can measure protein–protein kinetics, but for ultra-strong affinities like SPARC–HSA, SPR may struggle due to baseline drift and limited sensitivity at low analyte concentrations [8]. Moreover, SPARC and HSA binding is highly specific and rapid, meaning one must capture fast association phases that occur when sub-nanomolar HSA is introduced. Conventional assays often rely on higher analyte concentrations or labeling strategies, which can perturb molecular interactions or fail to provide sufficient temporal resolution. The key challenge is to detect real-time binding events at concentrations as low as 10^{-10} M, requiring a sensor that offers both high sensitivity and rapid response to resolve the fast association and slow dissociation kinetics characteristic of high-affinity complexes [12]. Achieving this demands an ultrasensitive, low-noise transducer combined with a robust immobilization approach that preserves the binding functionality of one interacting molecule.

A photonic crystal sensor supporting BICs is proposed to meet these requirements[13][14], offering the necessary sensitivity and temporal resolution to quantify SPARC–HSA binding kinetics in real time, even at sub-nanomolar concentrations. The aim of this chapter is to demonstrate an enhanced level of kinetic analysis for high-affinity protein interactions, bridging the gap between biomarker detection and dynamic interaction monitoring. The chapter is structured to cover the sensor design and experimental methods (Section 4.2), the results and analysis of SPARC–HSA binding experiments (Section 4.3), and a comparative discussion of the findings in the context of existing techniques and biological implications (Section 4.4).

4.2 Sensor Design and Experimental Methods

4.2.1 BIC Sensor Design and RCWA Simulations

The schematic of the proposed device is shown in Figure 4.1a, featuring a silicon nitride PhCS on a quartz substrate, enclosed within a PDMS-based microfluidic chamber that is optically transparent in the visible range. The geometric configuration was carefully designed based on a targeted strategy. Three key parameters including hole radius r, slab thickness t, and lattice constant a (as shown in Figure 4.1b) were systematically varied in simulations to predict the experimental transmittance band diagram. By tracking the peak wavelengths of the three primary modes, labeled λ_1, λ_2, and λ_3, as functions of r, t and a, the formation of two BIC at the Γ point was identified. These BIC modes correspond to λ_2 and λ_3, whose linewidths diminish as the angle of incidence approaches normal (Γ point), reflecting the characteristic diverging Q-factor associated with BICs (Figure 4.1c).

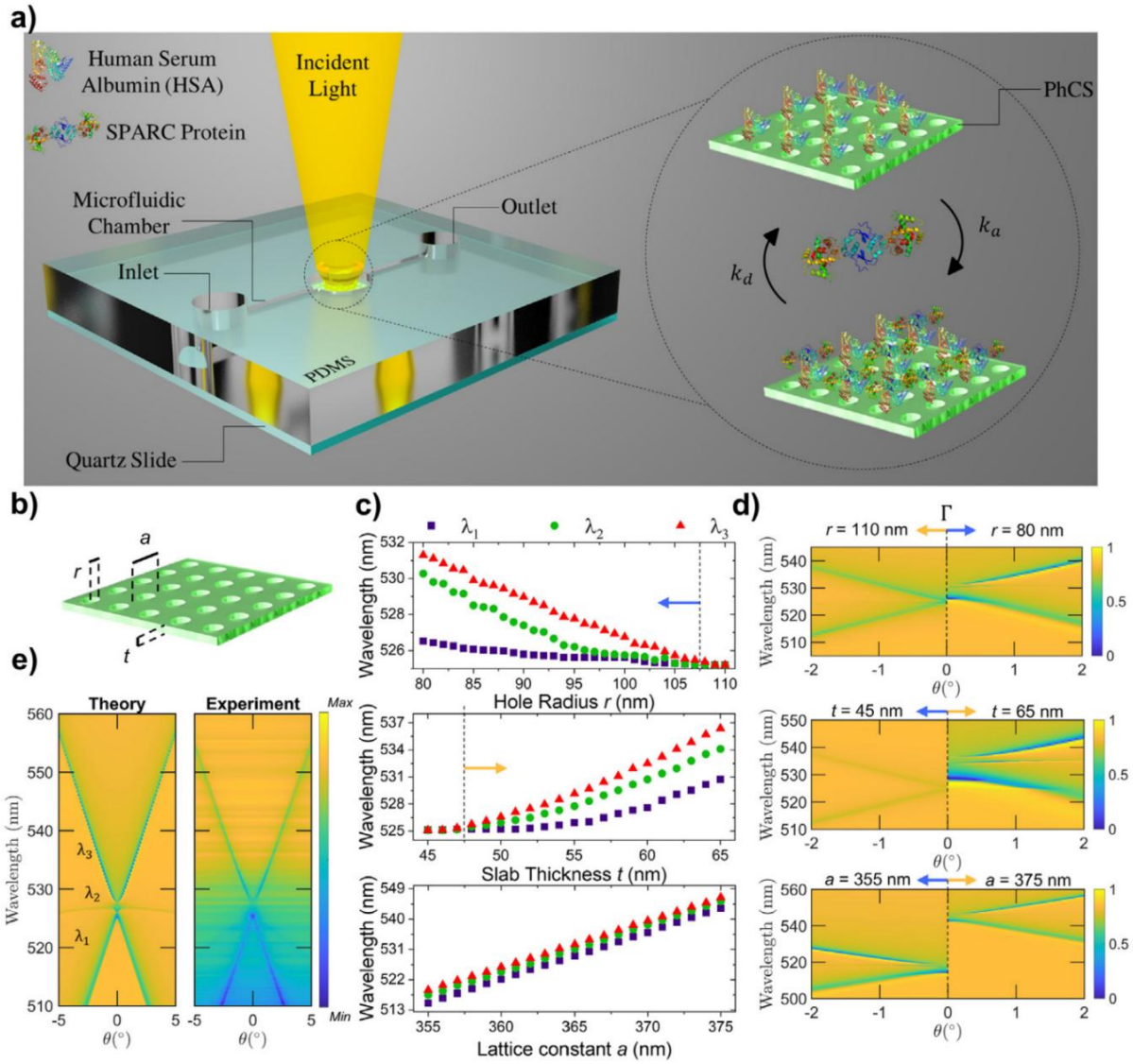

Figure 4.1: (a) A schematic illustration of the microfluidic-integrated optical system designed for the precise measurement of the SPARC/HSA dissociation constant. (b) PhCS sketch showing a Si_3N_4 slab having thickness t, and patterned with a square lattice (lattice constant a) of holes with radius r. (c) Parametric tuning of the PhCS modes position λ_1, λ_2 and λ_3 as a function of the structural parameters r, t, and a at the Γ point (θ=0°). The arrows denote Dirac cone splitting as a function of the decreasing r and increasing t. (d) Comparison of the simulated band diagrams for TE-like modes (s-polarization) as a function of the incidence angle θ obtained as a function of r (r = 110 nm, on the left, and r = 80 nm, on the right), t (t = 45 nm, on the left, and t = 65 nm, on the right), and a (a = 355 nm, on the left, and a = 375 nm, on the right). (e) Simulated transmittance band diagrams (r = 95 nm, t = 56 nm, and a = 363 nm) compared with experimental band diagram of the PhCS for TE-like modes (s-polarization) as a function of the incidence angle θ [1].

When the hole radius r is sufficiently large and the slab thickness t is relatively small (specifically, r>107nm for a=363 nm and t=56 nm, or t<48 nm for a=363 nm and r=86 nm), the modes become degenerate at the Γ point in momentum space, enabling the formation of a Dirac cone [15][16]. As shown in Figure 4.1c, the evolution of the modes with respect to r and t reveals that the Dirac cone becomes gapped below certain r values and above certain t values, accompanied by the appearance of two non-degenerated modes. Simultaneously, the spectral positions of modes λ_2 and λ_3 can be tuned by varying the lattice constant a. The spectral separation among the three modes can also be tuned by adjusting the r/t ratio, regardless of a. Figure 4.1d presents representative band diagrams as functions of the geometric parameters, providing further insight into the behavior of the dispersion curves. Notably, increasing the slab thickness t, while keeping a and r constant, has a pronounced impact on the linewidths of modes λ_1 and λ_3.

Figure 4.1e presents both the predicted and experimentally measured transmittance spectra for s-polarization (TE-like modes). A strong correlation between the theoretical model and experimental data is observed for the parameters r=95nm, t=56nm, and a=363nm, which were identified through RCWA simulations as an optimized geometry for the PhCS supporting BIC resonances. The narrow linewidth of mode λ_2 was experimentally resolved only after incubation in the buffer solution, due to a reduction in the Q-factor caused by surface radiative losses, consistent with previous findings [16].

Further Numerical simulations were performed to estimate the refractometric sensitivity of modes λ_2 and λ_3 with respect to changes in both the refractive index n and the thickness δt of the surface layer. To more accurately model the sensor ability to detect SPARC/HSA interactions, two different cladding environments were considered: one with a refractive index n_{cladding}=1.0, representing

measurements taken after the sample had dried, and another with n_{cladding}=1.33, simulating measurements conducted in PBS buffer during real-time spectral monitoring.

Figure 4.2a presents the transmittance band diagrams (s-polarization) calculated for r=95 nm, t=56 nm, and a=363 nm, using a cladding refractive index of n_{cladding} =1.0. Simulations include a surface layer with a refractive index of 1.42 and varying thicknesses δt =0, 4, and 7 nm. These thickness values were selected based on the hydrodynamic radii of SPARC and HSA, which are 4 nm and 7 nm, respectively. The refractive index of the thin layer approximates the optical properties of the biomolecular layer formed by the immobilization of SPARC and HSA on the PhCS surface [17]. Both modes, λ_2 and λ_3 , exhibit a redshift with increasing δt across all incident angles θ. Remarkably, the redshift of λ_3 becomes less pronounced at higher incident angles.

The peak wavelength shift, $\Delta\lambda$, for both BIC modes was analyzed at a fixed incidence angle of 3° by varying the refractive index and thickness of the biolayer, assuming an air cladding environment (Figures 4.2b–4.2c). When the biolayer thickness was 7 nm, both $\Delta\lambda_2$ and $\Delta\lambda_3$ showed an exponential increase with the refractive index. In contrast, for δt =4 nm, mode λ_2 exhibited an approximately linear trend, while mode λ_3 continued to follow an exponential response. At a fixed biolayer refractive index of n=1.42, the wavelength shifts were $\Delta\lambda_2$ =0.9nm and 1.5 nm for δt =4 and 7 nm, respectively, while $\Delta\lambda_3$= 0.3nm and 0.7 nm for the same thicknesses. Due to the varying response of mode λ_2 in air depending on layer thickness, mode λ_3 was selected as the primary mode for all functionalization and kinetic measurements, as it exhibits a more regular and linear response to thickness and refractive index under the operating conditions, ensuring consistency in spectral shift analysis.

Figure 4.2d displays the transmittance band diagrams (s-polarization) for the same PhCS, this time with a cladding refractive index of n_{cladding}=1.33. In this configuration, both modes λ_2 and λ_3 continue to exhibit a redshift as the surface layer thickness δt increases. Notably, the redshift of λ_3 remains nearly unvaried across varying incident angles θ.

The two BIC modes demonstrate even greater sensitivity to changes in refractive index, as shown in Figures 4.2e–4.2f. Both $\Delta\lambda_2$ and $\Delta\lambda_3$ show more pronounced shifts within the lower refractive index range of 1.33–1.60. This indicates improved surface sensitivity under wet conditions, consistent with the increased evanescent field penetration depth, which is beneficial for continuous monitoring applications. In this refractive index range, both modes display a linear response, with sensitivity increasing as the surface layer thickness δt grows, as expected. Consistent with earlier analyses, mode λ_3 was again selected for real-time experiments.

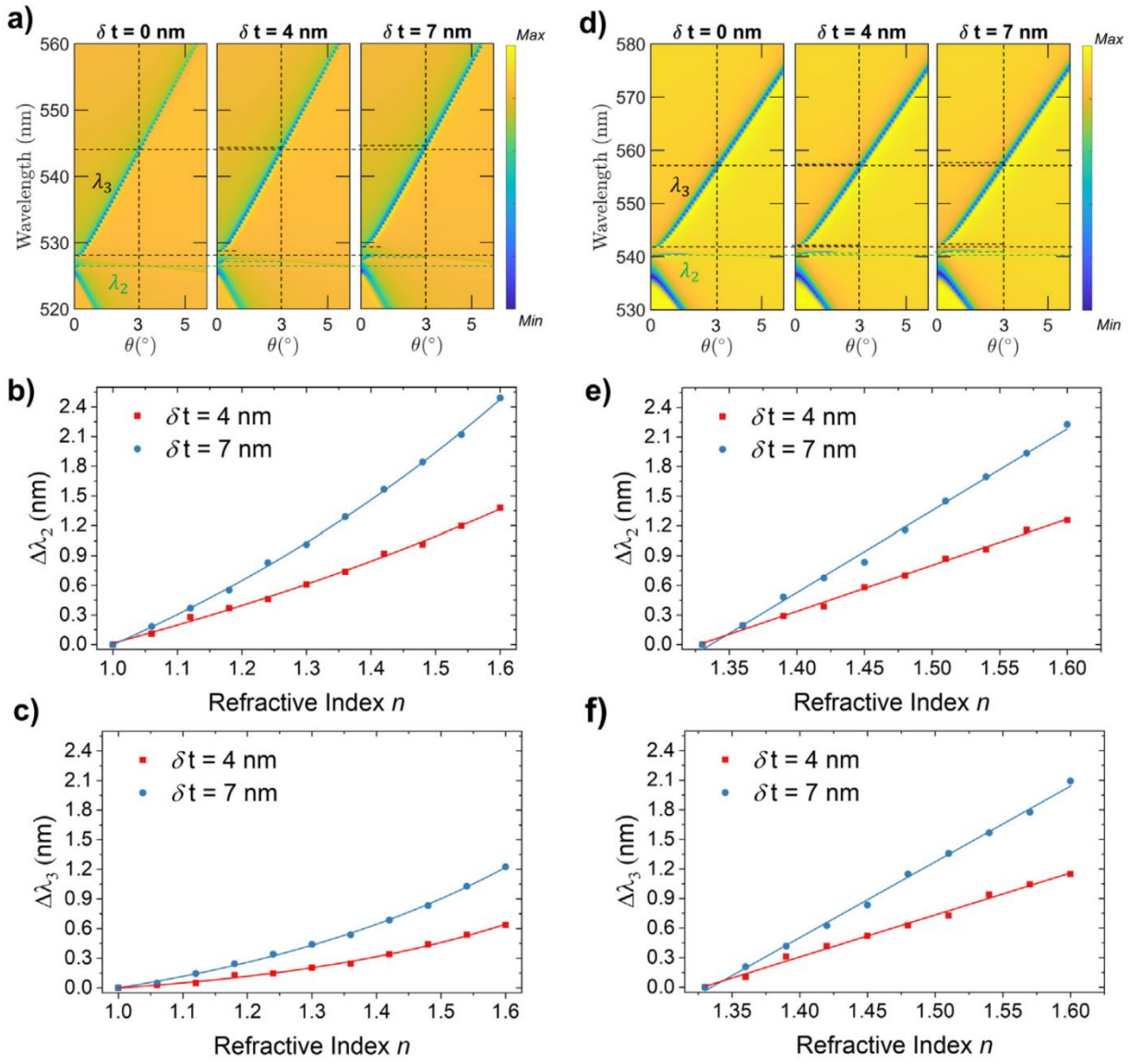

Figure 4.2: (a) Simulated transmittance (s-pol) band diagrams of a PhCS (r = 95 nm, t = 56 nm, and a = 363 nm) in air (cladding refractive index n_{cladding} = 1.0) with a biorecognition layer with refractive index of 1.42 and thickness δt = 0, 4, 7 nm. Theoretical wavelength shifts $\Delta\lambda(3^{\circ})$ of modes (b) λ_2 and (c) λ_3 as a function of the bio-film with increasing refractive index (from 1.0 to 1.6) with δt = 4 nm (red) and 7 nm (blue) with n_{cladding} = 1.0. (d) Simulated transmittance (s-pol) band diagrams of a PhCS (r = 95 nm, t = 56 nm, and a = 363 nm) in buffer (cladding refractive index = 1.33) with a biorecognition layer with refractive index of 1.42 and thickness δt = 0, 4, 7 nm. Theoretical wavelength shifts $\Delta\lambda(3^{\circ})$ of modes (e) λ_2 and (f) λ_3 as a function of the bio-film with increasing refractive index (from 1.33 to 1.60) with δt = 4 nm (red) and 7 nm (blue) with n_{cladding} = 1.33 [1].

Here, the photonic crystal design provides two sensing resonances; by choosing appropriate geometry and angle approximately 3° off-normal for measurements, a stable resonance (λ_3) with

high surface sensitivity and minimal radiative losses is achieved, making it ideal for kinetic experiments.

4.2.2 Surface Functionalization Strategy

The functionalization of Si_3N_4 PhCS was carried out using a standard procedure for silicon-based substrates. First, the PhCS were washed three times with absolute ethanol, followed by three rinses with double-distilled water (ddH_2O) for 5 minutes at room temperature (RT). To generate silanol groups (Si–OH) on the silicon nitride surface, the crystals were sequentially immersed in hexane (5 min, RT), ddH_2O (5 min, RT), and Piranha solution (H_2SO_4:H_2O_2, 3:1 v/v) for 30 minutes at 90 °C. This was followed by immersion in 0.5 M NaOH and 0.1 M HCl aqueous solutions. The samples were then rinsed again with ddH_2O (5 min, RT).

For silanization and introduction of amino groups ($–NH_2$), the PhCSs were incubated in a 5% v/v APTES (3-aminopropyl-triethoxysilane) solution prepared in anhydrous toluene for 120 minutes at 37 °C. Afterward, the crystals were washed three times with toluene (2 min, RT) and cured at 100 °C for 10 minutes. Next, surface functionalization with BS^3 (bis(sulfosuccinimidyl)suberate, 10 mM in 20 mM HEPES buffer, pH 7.5) was performed for 5 hours at 4 °C. The PhCSs were then washed three times with 20 mM HEPES buffer (pH 7.5) and ddH_2O (5 min, RT), and incubated overnight at 4 °C with either SPARC (14 μM, 5 μL) or rHSA (7 μM, 5 μL) in PBS 1×.

Prior to incubation with the analyte proteins (rHSA or SPARC), any unreacted N-hydroxysuccinimide (NHS) groups of BS^3 were quenched with 200 mM Tris–HCl buffer (pH 7.5) for 30 minutes at RT. This passivation step ensured that, during subsequent binding experiments, the sensor surface did not retain nonspecific reactive groups that could otherwise capture analyte molecules or other proteins indiscriminately. Finally, the PhCSs were rinsed three times with PBS 1× (5 min, RT).

4.2.3 Optofluidic Setup and Spectroscopy

To enable real-time monitoring of binding interactions, the PhCS chip was integrated into an optofluidic flow cell. A polydimethylsiloxane (PDMS) microfluidic chamber was bonded onto the PhCS, aligning the channel region precisely over the nanohole array (Figure 4.1a). Using this integrated microfluidic–PhCS setup and the optimized functionalization strategy, the dissociation constant between SPARC and HSA was determined under dynamic flow conditions.

The microfluidic chamber was fabricated by soft lithography using a PDMS prepolymer mixture prepared at a 10:1 (w/w) ratio. The mixture was poured into a Petri dish, degassed under vacuum to

remove air bubbles, and cured for 3.5 h at 60 °C. The resulting microfluidic chip comprised an incubation chamber connected to an inlet and an outlet through a 0.5 mm-wide microchannel. The incubation chamber was a cylindrical cavity with a radius of 1.5 mm, and the total device height was 0.2 mm. Two holes were punched to enable fluid inflow and outflow, and bent needles were used to connect the syringe tubing to the microchannel for solution delivery.

The chamber was bonded to the PhCS surface by oxygen plasma treatment followed by thermal curing at 50 °C for 5 min. Fluid flow was controlled using a KD Scientific syringe infusion pump, allowing accurate regulation of the total infused volume. Association and dissociation experiments were conducted for 30 min each at a constant flow rate of 10 μL/min in PBS. During association, SPARC solutions at concentrations of 0.25, 0.5, 1, 2, 4, 8, and 16 nM were injected, while during dissociation, the SPARC solution was replaced with PBS to reestablish equilibrium and remove bound molecules. A blank measurement (0 nM SPARC) was performed by flowing PBS under identical conditions. Each experiment was repeated at least three times ($n \geq 3$).

Spectral measurements were performed using a dedicated optical setup. PhCS samples were illuminated with a collimated broadband supercontinuum laser (NKT Photonics, SuperK EXTREME) and the transmitted light was collected with a fiber-coupled spectrometer (Ocean Optics USB4000) with a wavelength resolution of 0.25 nm, sufficient to track sub-nanometer shifts. Collimated light was incident on the PhCS at a small angle (3° off-normal) to excite the quasi-BIC resonances, which are symmetry-protected at normal incidence (0°). By selecting s-polarization (electric field in-plane, corresponding to the TE-like PhCS modes), the two target resonances (λ_2 and λ_3) were specifically excited.

Angle-resolved transmission band diagrams were reconstructed by acquiring spectra at different incidence angles using a computer-controlled rotational stage, which provided an angular resolution of 0.01° for precise identification of the resonance positions [15]. Band diagrams were reconstructed using a custom MATLAB routine, which included a fast Fourier transform-based filtering step to remove background noise [14].

4.3 Results and Discussion

4.3.1 Sensor Characterization and Functionalization Validation

The fabricated PhCS device was experimentally validated to exhibit the expected photonic band structure and to sustain the high-Q resonances required for sensing applications. Angle-resolved transmission spectra revealed two distinct Fano resonances (modes λ_2 and λ_3) whose wavelengths

varied with the incidence angle, forming dispersion branches consistent with the RCWA-simulated band diagram (Figure 4.1e). At normal incidence, the two modes merged into a Dirac-like point, and upon increasing θ, they split apart, with λ_3 exhibiting a stronger red-shift than λ_2 [18]. The measured resonance positions agreed well with the simulations, confirming that the device operated in the BIC regime characterized by a very high Q-factor [19].

To evaluate the dissociation constant, the functionalization protocol was optimized to enable reversible interactions between SPARC and HSA. Two groups of PhCSs were prepared: one functionalized with SPARC as the bioprobe and the other with HSA. Both followed the same immobilization workflow (Figure 4.3a): Piranha cleaning, APTES silanization, and BS^3 crosslinking, followed by incubation with either SPARC (14 μM) or HSA (7 μM). After covalent attachment of the bioprobe, a passivation step with Tris–HCl buffer was performed to neutralize residual BS^3 reactivity.

To test binding reversibility, HSA (0.3 nM) and SPARC (1.0 nM) in PBS (pH 7.4) were drop-cast on SPARC- and HSA-functionalized PhCSs, respectively. Dissociation of the analyte from the immobilized bioprobe was induced by lowering the pH, achieved by incubating the samples in HEPES buffer at pH 5.0. After each step, transmittance band diagrams were recorded, and normalized difference bands were generated as indicated in Figure 4.3b and 4.3d. The variation of the third mode (λ_3) at the BIC was tracked across functionalization stages for $\theta \in 2°–4°$, with peak shifts ($\Delta\lambda(\theta)$) relative to pristine PhCSs reported as mean ± standard deviation (SD), as summarized in the histograms of Figure 4.3c and 4.3e.

For SPARC-immobilized PhCS, $\Delta\lambda = 2.45 \pm 0.12$ nm was observed after silanization, with a further 0.4 nm redshift ($\Delta\lambda = 2.85 \pm 0.12$ nm) following SPARC immobilization (14 μM). The Tris–HCl passivation step caused no significant spectral change. Interaction with HSA produced an additional 0.3 nm redshift ($\Delta\lambda = 3.15 \pm 0.13$ nm). However, after the HEPES pH 5 wash, the resonance only partially shifted back (Figure 4.3c), showing that HSA was not fully removed from the SPARC-coated surface. This irreversible adsorption confirmed that using SPARC as the immobilized ligand does not support repeatable kinetic cycles.

For HSA-immobilized PhCS (Figure 4.3e), silanization produced a $\Delta\lambda = 2.45 \pm 0.12$ nm, which increased to $\Delta\lambda = 2.97 \pm 0.12$ nm after HSA immobilization (7 μM). The larger shift compared to SPARC is attributed to HSA higher molecular weight, which increases the effective refractive index at the sensor surface. Passivation with Tris–HCl again caused no significant spectral change. Subsequent binding of SPARC induced a 0.3 nm redshift ($\Delta\lambda = 3.35 \pm 0.13$ nm). In this case, the

HEPES pH 5 wash produced a 0.3 nm blueshift, effectively restoring the resonance nearly to its pre-binding position. This demonstrated that HSA-coated surfaces can be regenerated between successive analyte-binding cycles using HEPES buffer, enabling continuous monitoring applications. These results demonstrate that there is a specific, reversible SPARC–HSA interaction; however, HSA also exhibits strong nonspecific adsorption typical of albumin, so when SPARC is immobilized on the surface, the observed binding reflects a combination of specific and nonspecific contributions. This highlights the need to carefully select the immobilized protein to ensure reliable assay performance, particularly for continuous measurements.

Nonspecific binding considerations further reinforce the choice of HSA as the immobilized ligand. Albumins, including HSA, are well known for their strong surface affinity and are commonly employed as "blocking" agents in bioassays because they effectively occupy available sites and prevent undesired protein adsorption [20]. In this system, HSA played two roles by offering specific binding sites for SPARC while also passivating the surface to prevent nonspecific fouling. As a result, immobilizing HSA rather than SPARC produces a more controlled and stable interface, minimizing background interference and enhancing detection specificity. In contrast, immobilizing SPARC can lead to unpredictable interactions with HSA, compromising assay reliability. Furthermore, the natural role of HSA as a biomolecule carrier enables it to maintain structural and functional integrity upon immobilization, creating an optimal environment for SPARC capture. This strategic design improves both the sensitivity and reproducibility of the sensing platform.

Figure 4.3 compiles these findings: part (a) illustrates the two functionalization approaches compared; parts (b) and (d) show transmittance bands before (pristine) and after incubation with SPARC (14 μM) and HSA (7 μM), respectively, with normalized difference bands indicated as "merge"; parts (c) and (e) summarize $\Delta\lambda(\theta)$ of the third mode λ_3 as a function of the functionalization step for $\theta \in 2°–4°$ with SPARC or HSA as bioprobes. The data confirm two key points: (1) The sensor BIC resonance is highly sensitive to molecular layer buildup, with sub-nanometer films producing measurable shifts. (2) Using HSA as the surface-attached molecule yields a reversible sensor, whereas SPARC on the surface leads to nonspecific HSA adsorption that cannot be fully reversed [20]. These observations are consistent with the previous experimental results: SPARC-coated surfaces exhibit irreversible binding, while HSA-coated surfaces allow efficient regeneration after each analyte-binding cycle. In the context of high-affinity interactions, ensuring reversibility is crucial for accurate kinetic analysis, as cumulative residual binding would distort successive measurements. By using HSA as the immobilized ligand, our BIC sensor meets

this requirement, providing a stable, passivated interface that supports reliable SPARC detection and repeated kinetic measurements.

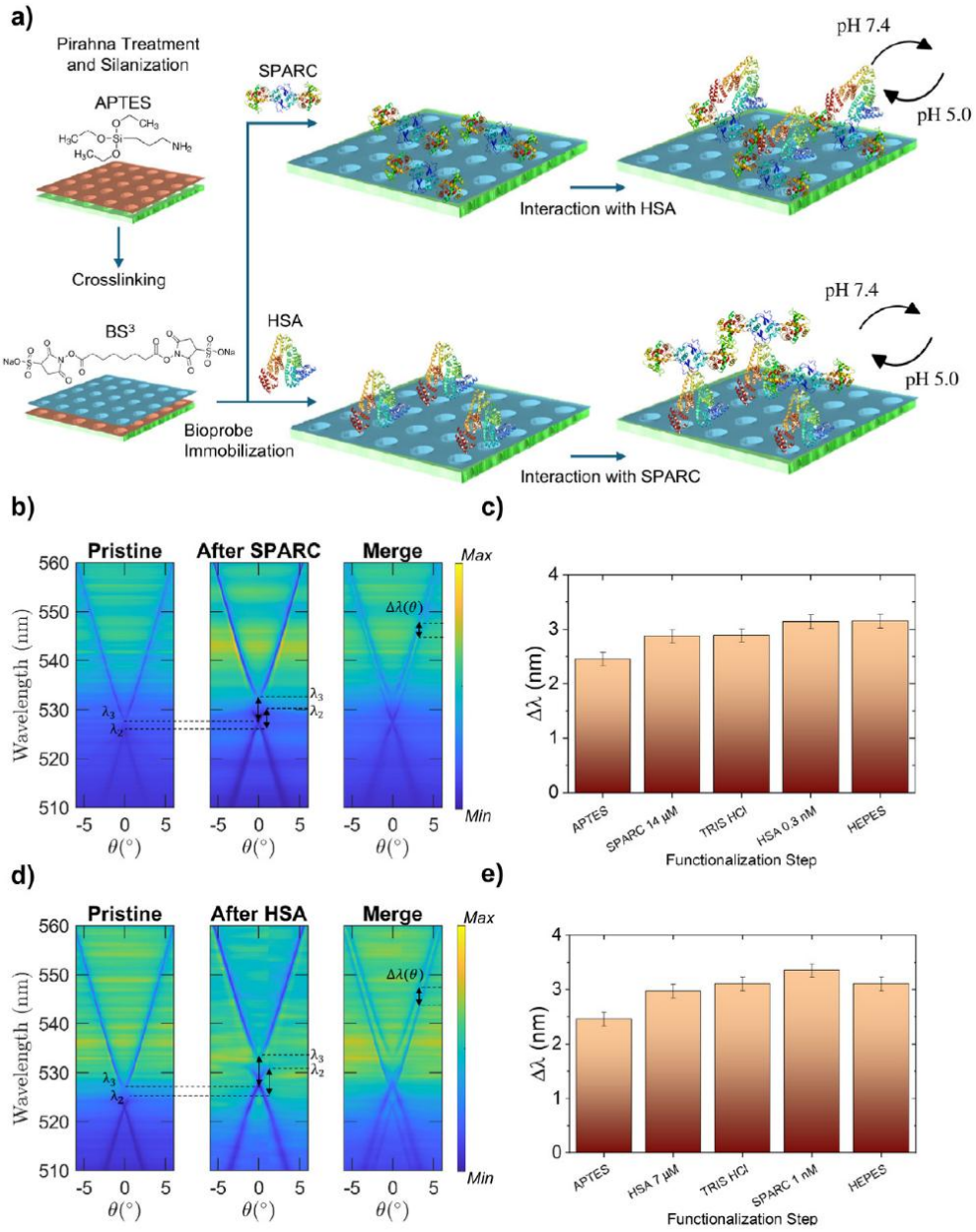

Figure 4.3: (a) Schematic representation of the adopted functionalization strategies. (b) Comparison of the transmittance bands before (pristine) and after incubation with SPARC (concentration C = 14 μM), and normalized difference band diagram indicated as merge. (c) Histogram of the $\Delta\lambda(\theta)$ of the third mode λ_3 as a function of the functionalization step with SPARC as a bioprobe (14 μM) for $\theta \in (2^\circ, 4^\circ)$. (d) Comparison of the transmittance bands before (pristine) and after incubation with HSA (concentration C = 7 μM), and normalized difference band diagram indicated as merge. (e) Histogram of the $\Delta\lambda(\theta)$ of the third mode λ_3 as a function of the functionalization step with HSA as a bioprobe (7 μM) for $\theta \in (2^\circ, 4^\circ)$ [1].

4.3.2 Real-Time Interaction Monitoring

The interaction between the immobilized ligand (HSA) and the analyte (SPARC) follows pseudo-first-order kinetics. During the association phase, the concentration of the [HSA–SPARC] complex increases over time according to the following kinetic equation:

$$\frac{d[HSA-SPARC]}{dt} = k_a[HSA][SPARC] - k_d[HSA-SPARC] \quad (4\text{-}1)$$

Here, the association rate constant k_a represents the rate of complex formation, i.e., the number of HSA–SPARC complexes formed per second in a 1 M solution of both species (k_a= [$M^{-1}s^{-1}$]). The dissociation rate constant k_d quantifies the complex stability, corresponding to the fraction of complexes that dissociate per second (k_d=[s^{-1}]).

The above kinetic equation can be transformed into a so-called integrated rate equation, which can be used to fit the experimental data:

$$R(t) = R_{eq} \cdot \left(1 - e^{-(k_a \cdot C_{SPARC} + k_a)(t-t_0)}\right) \quad (4\text{-}2)$$

where R and R_{eq} are the physical readout parameters defining the binding transduction over time in the sensor, such as the shift of Fano peak of the resonance tracked over time $\Delta\lambda(t)$ and its equilibrium condition $\Delta\lambda_{eq}$, respectively.

When the analyte solution flowing over the sensor is replaced by buffer, the free analyte concentration rapidly decreases to zero, initiating the dissociation of the complex. By neglecting the rebinding of the released analyte, dissociation can be described by the rate equation:

$$\frac{dR}{dt} = -k_d . R \quad (4\text{-}3)$$

The dissociation rate constant (k_d) can be reliably measured by dissociating the analyte from the ligand after the buffer replaces the analyte solution. Also in this case, it is possible to fit the integrated rate equation to the experimental data:

$$R(t) = R_0 \cdot e^{-k_d(t-t_0)} + R_{(t\to\infty)} \quad (4\text{-}4)$$

where $R_0 = \Delta\lambda(t = 0)$ and $R_{(t\to\infty)}$ is the offset to be considered when at $t \to \infty$ the sensogram has not returned to zero.

Figure 4.4a presents the typical redshift of the Fano resonance peak upon molecular binding in the transmittance spectrum. The profile can be fitted to:

$$\frac{I(\lambda)}{I_0} = 1 - \frac{\left(q + \frac{2(\lambda - \lambda_0)}{\sigma}\right)^2}{1 + \left(\frac{2(\lambda - \lambda_0)}{\sigma}\right)^2} \tag{4-5}$$

with peak λ_0, linewidth σ and asymmetry parameter q. Instead of analyzing only the peak shift, the full spectral evolution was evaluated by tracking temporal variations in σ and q, and consequently in the quality factor Q. Typically, Q decreases upon molecular binding [16].

This analysis enabled the definition of a more sensitive readout parameter, the tracking parameter η, which monitors the maximum derivative position. Because resonance broadening amplifies changes in η, this metric provides enhanced sensitivity. In the example shown, η shifts by 0.25 nm, compared to a peak shift of only 0.1 nm. Figure 4.4b illustrates the temporal evolution of the Fano profile following analyte release at t=0, while Figure 4.4c presents the corresponding change in the resonance quality factor. After an initial increase, once binding stabilizes, the resonator losses rise accordingly. By combining these parameters, precise quantification of binding kinetics was achieved while minimizing the effects of misalignment or other experimental drifts during long acquisition periods (30–60 min).

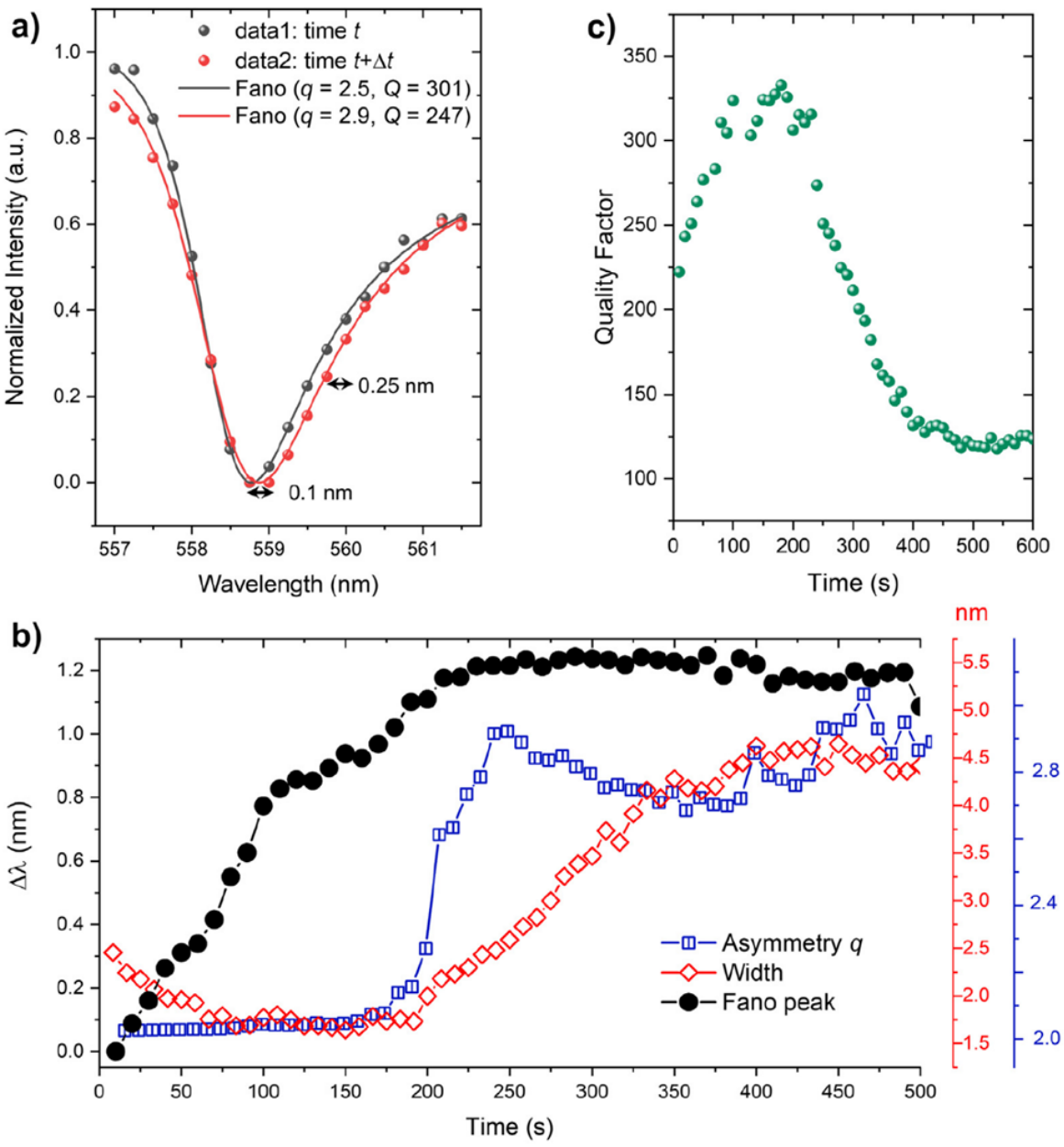

Figure 4.4: (a) Example of Fano-shaped peak evolution upon binding: Fano asymmetry and quality factor change with the spectral shape, so that the tracking parameter η, i.e., the spectral position of derivative maximum, shifts more than the peak position, 0.25 nm vs. 0.1 nm in this case. (b) Typical evolution over time of the resonance spectral profile upon analyte binding. (c) Related evolution of the quality factor, with its characteristic drop upon molecular binding [1].

Equations (4-2)–(4-4) were used to fit the experimental data and to extract the association and dissociation rate constants describing the interaction between SPARC and HSA. Figure 4.5a shows the experimental band diagrams of the HSA-functionalized PhCS within the microfluidic chamber, recorded before and after incubation with SPARC at a concentration of 1 nM. As predicted by simulations, the BIC mode, denoted as λ_3, exhibits a pronounced red shift of approximately 14 nm

upon immersion in PBS, reflecting the high bulk sensitivity of the PhCS. Following incubation with SPARC, an additional red shift (up to 0.8 nm at 16 nM) is observed, confirming the occurrence of specific molecular interactions at the functionalized surface.

To quantify these interactions, the response of λ_3 was monitored across a range of SPARC concentrations. As shown in Figure 4.5b, the wavelength shift increases with concentration and saturates at 8 nM, indicating that all available HSA binding sites are occupied and equilibrium has been reached. The association phase was carried out at a constant flow rate of 10 μL/min to minimize mass transport limitations and ensure reliable kinetic evaluation. After each association step, band diagrams were recorded to monitor the real-time binding events. These data were further analyzed to construct the dose–response curve in Figure 4.5c, which illustrates the dependence of the resonance wavelength shift ($\Delta\lambda$) on SPARC concentration. The response was determined by averaging λ_3 over the angular range $\theta \in (2°, 4°)$ to enhance measurement precision. Control measurements (PBS 1x, pH 7.4) confirmed no significant shifts during incubation, as shown in Figure 4.5c.

The dose–response curve was fitted using a Michaelis–Menten model, a standard approach for describing biomolecular binding kinetics. The fitting results confirmed a 1:1 binding stoichiometry between HSA and SPARC, validating the specificity of the interaction. The extracted kinetic parameters provided valuable insights into both the kinetic and thermodynamic behavior of the SPARC–HSA complex, relevant for future biosensing applications. In this study, the LOD was not considered a critical parameter, since the primary objective was to achieve stable signals and accurate, real-time kinetic measurements rather than to detect trace concentrations in complex samples.

Figure 4.5d presents the sensograms showing the temporal evolution of the tracking parameter $\eta(\lambda_3)$ at an incident angle of $\theta = 0.5°$, measured for SPARC concentrations of 1.0 and 2.0 nM. To establish a stable baseline, the sensor was equilibrated in PBS for 60 s before introducing the SPARC solution into the microfluidic channel using a syringe pump. The spectral evolution was then continuously monitored to capture the association phase of SPARC binding to the HSA-functionalized PhCS. Once equilibrium was reached, the SPARC solution was replaced with PBS to initiate dissociation. The subsequent decrease in the resonance wavelength confirmed the detachment of SPARC molecules from the sensor surface. Data acquisition continued until the signal stabilized at baseline level. To ensure reproducibility and remove any residual bound molecules, the sensor surface was regenerated with HEPES buffer, and the experiments were

repeated at progressively higher SPARC concentrations. A maximum of two to three regeneration cycles was performed, as further reuse led to gradual sensor degradation.

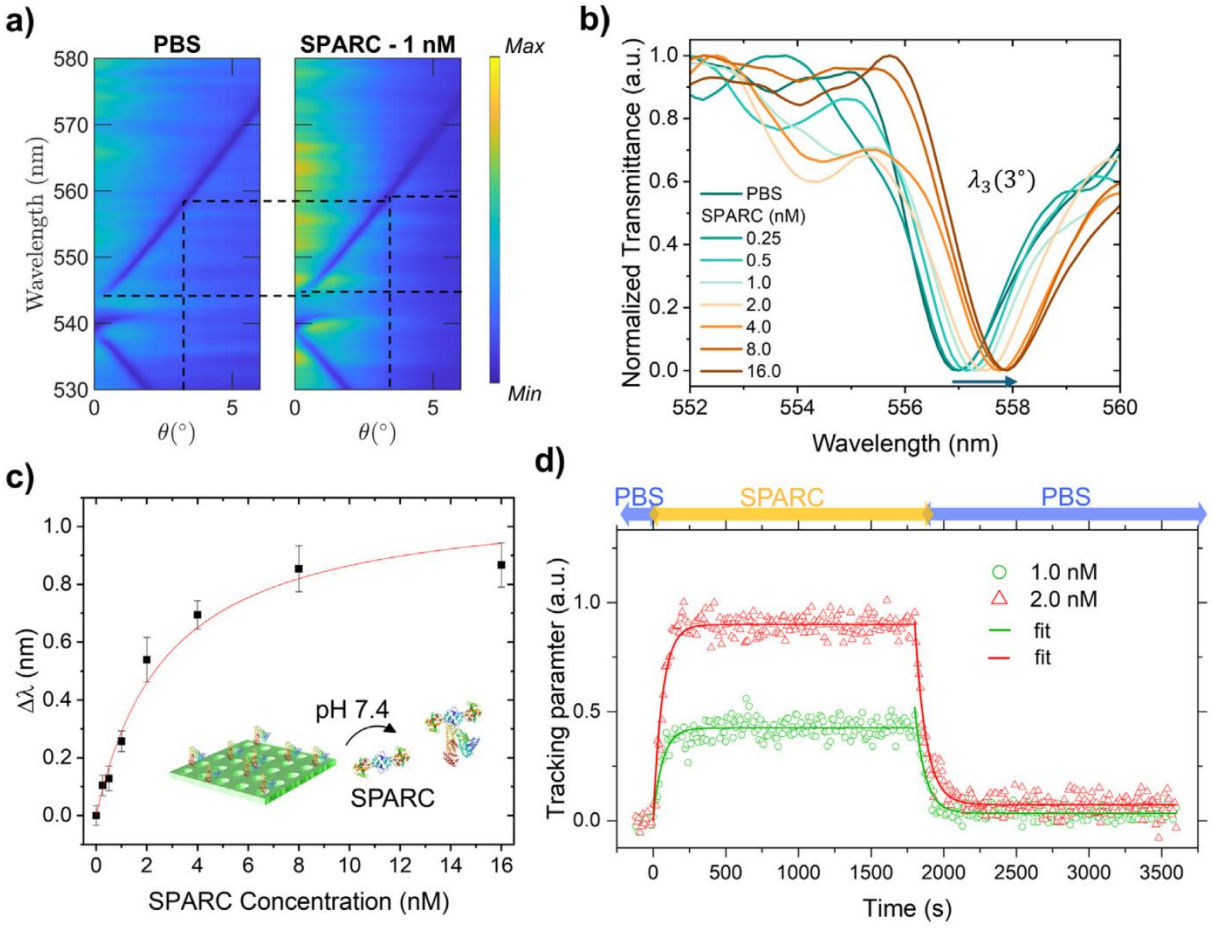

Figure 4.5: (a) Transmittance bands before (PBS) and after incubation with SPARC (C = 1 nM). (b) Normalized transmittance spectra of the third mode λ_3 as a function of the SPARC concentration after the equilibrium (PBS, 0.25, 0.5, 1.0, 2.0, 4.0, 8.0, and 16.0 nM) at θ = 3°. (c) Mean $\Delta\lambda$ (over the incidence angle θ) of λ_3 after incubation with SPARC at different concentrations (0.25, 0.5, 1.0, 2.0, 4.0, 8.0, and 16.0 nM). Curve fitting was performed using the Michaelis Menten equation. The reaction has been carried out at pH 7.4 in PBS buffer. Vertical bars denote the SD obtained for an incidence angle range spanning from ±2◦ to ±4◦ with a step of 0.01◦. (d) Sensorgram showing the evolution of the tracking parameter after incubation with SPARC protein at 1.0 nM (green), and 2.0 nM (red). Before each SPARC incubation (indicated with yellow arrow), the HSA-functionalized PhCS was initialized in PBS (pH 7.4 - blue arrow). The dissociation phase was carried out after SPARC association in the same buffer (PBS pH 7.4 - blue arrow). The association kinetics fitting curves were obtained by using Eq. (4-2). The dissociation kinetics fitting curves were obtained by using Eq. (4-4) [1].

The experimental data were analyzed by fitting the sensogram curves using Eqs. (4-2)–(4-4), and the extracted kinetic parameters are summarized in Table 4.1. By averaging the results across the

three tested SPARC concentrations, an association rate constant of $k_a=(1.7\pm0.2)\times10^6\,M^{-1}s^{-1}$ and a dissociation rate constant of $k_d=(1.4\pm0.1)\times10^{-2}\,s^{-1}$ were determined. The equilibrium dissociation constant, calculated as $K_D=k_d/k_a$, was found to be 8.2±0.8 nM. This value aligns well with the broad range of reported K_D values for SPARC–HSA interactions in the literature, which span from approximately 1 nM to 100 μM. However, while specific values for the SPARC-HSA complex dissociation constant are poorly available, several studies have demonstrated a significant binding affinity between these two proteins [21][22][23][24]. These studies confirm a meaningful binding affinity between SPARC and HSA and highlight the need for more quantitative studies to determine the exact dissociation constant for this interaction.

The obtained kinetic and equilibrium constants are in good agreement with the recent findings of Cini et al. [25] for HSA immobilized on solid substrates. The results confirm the strong affinity and specific interaction between SPARC and HSA, validating the robustness and accuracy of the PhCS-based biosensing platform for real-time kinetic measurements.

Table 4.1: Kinetic parameters for SPARC binding at different concentrations [1].

SPARC C (nM)	**k_a ($M^{-1}s^{-1}$)**	**k_d (s^{-1})**	**K_D (nM)**
1.0	1.8×10^6	1.4×10^{-2}	7.71
2.0	1.5×10^6	1.3×10^{-2}	8.82
Average	$1.7 \pm 0.2 \times 10^6$	$1.4 \pm 0.1 \times 10^{-2}$	8.2 ± 0.8

4.4 Comparative Analysis and Implications

4.4.1 Validation Against Literature

The findings of this study can be benchmarked against prior studies that attempted to quantify SPARC–HSA binding. As mentioned, Chlenski et al. reported a K_D of approximately 18.9 μM using SPR [8], which is three orders of magnitude weaker than the value obtained here (8.2 nM). That SPR result was likely influenced by limitations such as mass transport effects or unfavorable surface orientation. In the study by Chlenski, SPARC was immobilized on the SPR chip while albumin was introduced in flow, a configuration known to be problematic because of the inherently adhesive properties of albumin [8]. In practice, tests revealed that HSA binding to SPARC-coated surfaces was largely irreversible, which could lead to overestimation of K_D (if one measures an apparent low affinity because HSA does not fully dissociate). In contrast, the configuration with

HSA immobilized and improved surface regeneration enabled a more accurate determination of the binding parameters, yielding a value closer to the true affinity. An ELISA-based measurement by Cini et al. reported K_D = 10 nM [25], which is in excellent agreement with the 8 nM value obtained in this study. ELISA, however, is an equilibrium assay and does not provide k_a or k_d; in contrast, the photonic sensor yields the kinetic constants directly, offering a more detailed understanding of the interaction dynamics.

Other literature reports include qualitative evidence that SPARC binds albumin strongly. For example, a study by Park et al. demonstrated in vivo that SPARC-expressing tumors accumulated albumin-based contrast agents to a significant extent, implying high affinity [21]. The present results quantitatively confirm this interaction. Additionally, Knauer et al. identified SPARC albumin-binding domains [22], indicating that the C-terminus contains the albumin-binding site, although no K_D value was reported in that conference abstract. The kinetic findings presented here can be interpreted within that structural context: a single site on SPARC likely mediates the interaction with albumin, consistent with the observed single-phase binding curves.

The accuracy of the BIC sensor was further validated by confirming that the K_D values obtained from kinetic and equilibrium analyses were consistent. This self-consistency strengthens confidence in the reliability of the methodology. Furthermore, the sensor enabled simultaneous determination of k_a and k_d within a single experiment. Although traditional SPR can also provide these parameters, it typically requires higher analyte concentrations to achieve sufficient signal, which can introduce errors in high-affinity systems due to effects such as rebinding or analyte depletion. Measurements were carried out in the 0.25–16 nM concentration range, ensuring that SPARC in solution was not limiting and that mass transport was sufficient. Under these flow conditions, the Damköhler number ($Da \ll 1$) indicated that the reaction rate was slower than diffusion, thereby avoiding transport limitations.

The obtained K_D = 8 nM confirms that the SPARC–HSA interaction is of high affinity, consistent with the low-nanomolar range suggested in previous studies [21][22][23][24]. Although this value differs substantially from one earlier SPR report, the considerations discussed above indicate that the present measurement is likely more accurate. These results demonstrate the capability of the ultrasensitive BIC sensor to clarify inconsistencies in reported values by enabling measurements under optimal conditions, including reversible binding cycles, low analyte concentrations, and minimal nonspecific effects. The close agreement with ELISA data and with known physiological observations of SPARC strong affinity for albumin further supports the reliability of these findings.

4.4.2 Performance Highlights of the BIC Sensor

The BIC-based photonic crystal sensor demonstrated exceptional performance in sensitivity, speed, and stability. It achieved ultrasensitive detection of protein binding at sub-nanomolar concentrations, with an estimated limit of detection in the tens of picomolar range. This was derived from a $\Delta\lambda$ noise of 0.005 nm during a 10-minute PBS baseline and a 0.1 nm shift corresponding to 0.5 nM SPARC (Figure 4.5c). Such high sensitivity results from the large Q-factor of the BIC resonance and the low optical losses of the dielectric structure[13][26].

The sensor exhibited rapid temporal response, limited only by the 0.5 s spectrometer acquisition time. The association phase was captured within seconds (Figure 4.5d), enabling precise kinetic fitting. Unlike many label-free sensors requiring signal averaging, the BIC device provided stable, high-speed readout essential for resolving fast, high-affinity interactions. Owing to its dielectric design, the sensor induced negligible heating or optical perturbation, in contrast to metal-based SPR systems. Operation in low-power transmission mode also prevented photobleaching or photo-induced effects. The platform showed excellent reusability and chemical stability, maintaining performance over multiple regeneration cycles. The Si_3N_4-on-quartz structure remained intact after piranha cleaning and buffer exposure, and the covalent APTES/BS^3 surface chemistry ensured durable protein attachment.

Its planar, integrable architecture supports scalability for arrays or microfluidic systems. Although characterized using free-space optics, it is compatible with fiber coupling and on-chip light sources, making it suitable for portable, point-of-care sensing. Compared with other techniques, the BIC sensor achieved K_D values comparable to or better than SPR and higher sensitivity than BLI, benefiting from its sharper high-Q resonances [8]. Unlike ELISA, it provides real-time, label-free analysis. The sensor detection limit in refractive index units was 2.5×10^{-5} RIU, based on a 0.005 nm shift near an 800 nm resonance with 200 nm/RIU sensitivity. This performance rivals leading plasmonic sensors while offering narrower, more stable resonances that can be tracked with standard spectrometers.

4.4.3 Applications in Cancer and Beyond

The successful kinetic resolution of SPARC–HSA binding has important implications for both cancer biology and protein interaction analysis. In oncology, these results support the notion that SPARC-rich tumors strongly bind albumin, a mechanism exploited by therapies such as nab-paclitaxel [27][7]. Understanding the kinetic parameters provides insight into drug delivery: rapid SPARC–albumin association and moderate retention could allow albumin-bound drugs to remain in

the tumor microenvironment long enough for cellular uptake before dissociation. The measured half-life suggests that some complexes may dissociate in circulation if not rapidly localized to SPARC-expressing tissue, though continuous SPARC secretion in the stroma would maintain a local albumin reservoir. These quantitative findings deepen our understanding of SPARC role in tumor nutrient acquisition and drug transport.

Beyond SPARC–HSA, the BIC photonic sensor offers a general platform for probing high-affinity interactions such as antigen–antibody, receptor–ligand, or cytokine–receptor bindings, which often exhibit nano to picomolar affinities. Conventional sensors struggle with such strong interactions due to mass transport limitations and surface regeneration issues. The ability to measure a tight binder like SPARC–HSA demonstrates the potential to study even stronger systems by tuning flow or temperature to facilitate dissociation. In drug discovery and systems biology, this capability enables rapid kinetic screening of inhibitors targeting high-affinity protein–protein interactions, where accurate residence time measurements are essential [12]. The BIC sensor thus represents a powerful, label-free platform for real-time kinetic analysis, with potential for multiplexed or miniaturized implementations for in situ measurements. Its precise K_D and rate determinations lay a foundation for developing improved albumin-based therapeutics and for advancing SPARC as both a therapeutic target and a biomarker in oncology.

4.5 References

[1] B. Miranda *et al.*, “Resolving SPARC–HSA binding kinetics with an ultrasensitive photonic sensor based on bound states in the continuum,” *Biosens Bioelectron*, vol. 288, p. 117754, Nov. 2025, doi: 10.1016/j.bios.2025.117754.

[2] I. T. Tai and M. J. Tang, “SPARC in cancer biology: Its role in cancer progression and potential for therapy,” *Drug Resistance Updates*, vol. 11, no. 6, pp. 231–246, Dec. 2008, doi: 10.1016/j.drup.2008.08.005.

[3] T. M. Parker *et al.*, “Cell competition in intratumoral and tumor microenvironment interactions,” *EMBO J*, vol. 40, no. 17, Sep. 2021, doi: 10.15252/embj.2020107271.

[4] F. Andriani *et al.*, “Diagnostic role of circulating extracellular matrix-related proteins in non-small cell lung cancer,” *BMC Cancer*, vol. 18, no. 1, p. 899, Dec. 2018, doi: 10.1186/s12885-018-4772-0.

[5] B. Carrese *et al.*, “Controlled Release of Doxorubicin for Targeted Chemo-Photothermal Therapy in Breast Cancer HS578T Cells Using Albumin Modified Hybrid Nanocarriers,” *Int J Mol Sci*, vol. 22, no. 20, p. 11228, Oct. 2021, doi: 10.3390/ijms222011228.

[6] B. Carrese *et al.*, “Hybrid Nanoparticle-Assisted Chemo-Photothermal Therapy and Photoacoustic Imaging in a Three-Dimensional Breast Cancer Cell Model,” *Int J Mol Sci*, vol. 24, no. 24, p. 17374, Dec. 2023, doi: 10.3390/ijms242417374.

[7] P. Zhao, Y. Wang, A. Wu, Y. Rao, and Y. Huang, “Roles of Albumin-Binding Proteins in Cancer Progression and Biomimetic Targeted Drug Delivery,” *ChemBioChem*, vol. 19, no. 17, pp. 1796–1805, Sep. 2018, doi: 10.1002/cbic.201800201.

[8] A. Chlenski *et al.*, “Secreted protein acidic and rich in cysteine (SPARC) induces lipotoxicity in neuroblastoma by regulating transport of albumin complexed with fatty acids,” *Oncotarget*, vol. 7, no. 47, pp. 77696–77706, Nov. 2016, doi: 10.18632/oncotarget.12773.

[9] Q. Ji *et al.*, “GP60 and SPARC as albumin receptors: key targeted sites for the delivery of antitumor drugs,” *Front Pharmacol*, vol. 15, Jan. 2024, doi: 10.3389/fphar.2024.1329636.

[10] L. Aarons, “Kinetics of drug-drug interactions,” *Pharmacol Ther*, vol. 14, no. 3, pp. 321–344, Jan. 1981, doi: 10.1016/0163-7258(81)90031-0.

[11] A. M. Giannetti, B. D. Koch, and M. F. Browner, “Surface Plasmon Resonance Based Assay for the Detection and Characterization of Promiscuous Inhibitors,” *J Med Chem*, vol. 51, no. 3, pp. 574–580, Feb. 2008, doi: 10.1021/jm700952v.

[12] R. A. Copeland, “The drug–target residence time model: a 10-year retrospective,” *Nat Rev Drug Discov*, vol. 15, no. 2, pp. 87–95, Feb. 2016, doi: 10.1038/nrd.2015.18.

[13] S. Romano *et al.*, “Label-free sensing of ultralow-weight molecules with all-dielectric metasurfaces supporting bound states in the continuum,” *Photonics Res*, vol. 6, no. 7, p. 726, Jul. 2018, doi: 10.1364/PRJ.6.000726.

[14] S. Romano *et al.*, “Tuning the exponential sensitivity of a bound-state-in-continuum optical sensor,” *Opt Express*, vol. 27, no. 13, p. 18776, Jun. 2019, doi: 10.1364/OE.27.018776.

[15] S. Romano *et al.*, “Ultrasensitive Surface Refractive Index Imaging Based on Quasi-Bound States in the Continuum,” *ACS Nano*, vol. 14, no. 11, pp. 15417–15427, Nov. 2020, doi: 10.1021/acsnano.0c06050.

[16] G. Zito *et al.*, “Molecularly Imprinted Polymer Sensor Empowered by Bound States in the Continuum for Selective Trace-Detection of TGF-beta,” *Advanced Science*, vol. 11, no. 41, Nov. 2024, doi: 10.1002/advs.202401843.

[17] X. Guo, H. Tai, X. Li, P. Liu, J. Liu, and S. Yu, “SPARC is a Novel Prognostic Biomarker for Ovarian Cancer and Associated with Immune Signatures and Drug Response,” *Clin Exp Obstet Gynecol*, vol. 51, no. 3, Mar. 2024, doi: 10.31083/j.ceog5103061.

[18] E. De Tommasi *et al.*, “Half-Integer Topological Charge Polarization of Quasi-Dirac Bound States in the Continuum,” *Adv Opt Mater*, vol. 11, no. 18, Sep. 2023, doi: 10.1002/adom.202300475.

[19] G. Zito *et al.*, “Label-free DNA biosensing by topological light confinement,” *Nanophotonics*, vol. 10, no. 17, pp. 4279–4287, Nov. 2021, doi: 10.1515/nanoph-2021-0396.

[20] J. N. Mulvihill, A. Faradji, F. Oberling, and J. Cazenave, “Surface passivation by human albumin of plasmaperesis circuits reduces platelet accumulation and thrombus formation. Experimental and clinical studies,” *J Biomed Mater Res*, vol. 24, no. 2, pp. 155–163, Feb. 1990, doi: 10.1002/jbm.820240203.

[21] C. R. Park *et al.*, “Secreted protein acidic and rich in cysteine mediates active targeting of human serum albumin in U87MG xenograft mouse models,” *Theranostics*, vol. 9, no. 24, pp. 7447–7457, 2019, doi: 10.7150/thno.34883.

[22] D. Knauer *et al.*, “Albumin-Binding and Angiogenic Domains of SPARC Located at Its C-Terminus.,” *Cancer Res*, vol. 69, no. 24_Supplement, pp. 2144–2144, Dec. 2009, doi: 10.1158/0008-5472.SABCS-09-2144.

[23] A. M. Merlot, D. S. Kalinowski, and D. R. Richardson, “Unraveling the mysteries of serum albuminâ€”more than just a serum protein,” *Front Physiol*, vol. 5, Aug. 2014, doi: 10.3389/fphys.2014.00299.

[24] B. Zheng *et al.*, “Modulating the tumoral SPARC content to enhance albumin-based drug delivery for cancer therapy,” *Journal of Controlled Release*, vol. 366, pp. 596–610, Feb. 2024, doi: 10.1016/j.jconrel.2023.12.057.

[25] J. K. Cini *et al.*, “SON-1210 - a novel bifunctional IL-12 / IL-15 fusion protein that improves cytokine half-life, targets tumors, and enhances therapeutic efficacy,” *Front Immunol*, vol. 14, Dec. 2023, doi: 10.3389/fimmu.2023.1326927.

[26] Y. Liu, W. Zhou, and Y. Sun, “Optical Refractive Index Sensing Based on High-Q Bound States in the Continuum in Free-Space Coupled Photonic Crystal Slabs,” *Sensors*, vol. 17, no. 8, p. 1861, Aug. 2017, doi: 10.3390/s17081861.

[27] P. Vishnu and V. Roy, “Safety and Efficacy of *nab* -Paclitaxel in the Treatment of Patients with Breast Cancer,” *Breast Cancer (Auckl)*, vol. 5, p. BCBCR.S5857, Jan. 2011, doi: 10.4137/BCBCR.S5857.

Chapter 5: Bimodal Waveguide (BiMW) Biosensors

5.1 Introduction

This Chapter discusses the establishment of a label-free, real-time detection method for ibuprofen using a competitive immunoassay implemented on a Bimodal Waveguide (BiMW) platform. Specifically, the work focused on optimizing surface functionalization strategies to immobilize a human serum albumin–ibuprofen (HSA–ibuprofen) conjugate, developing a competitive assay in which free ibuprofen competes with the immobilized conjugate for antibody binding, and constructing a calibration curve to enable quantitative analysis. By leveraging the BiMW biosensor, this approach aims to provide rapid, sensitive, and versatile detection suitable for both pharmaceutical quality control and environmental monitoring. Such activities have been carried out during my exchange period at the Institut Català de Nanociència i Nanotecnologia (ICN2) under the supervision of Prof. Laura Lechuga.

5.1.1 Motivation and objectives

Ibuprofen is a widely used non-steroidal anti-inflammatory drug (NSAID) for treating pain, fever, and inflammatory conditions [1], and is the only NSAID approved for children over three months old [1][2]. Despite its efficacy and tolerability, overdose can cause serious side effects such as gastrointestinal complications, nephrotoxicity, and skin reactions [3]. Furthermore, incomplete metabolism leads to environmental contamination, [4] and chronic exposure has been linked to adverse effects on muscle development, aerobic respiration, and immune function, [5] making ibuprofen an emerging environmental pollutant.

In environmental samples, ibuprofen is typically detected at concentrations ranging from nanograms to micrograms per liter (ng/L–µg/L) [6][7]. In contrast, therapeutic plasma levels in clinical and pharmacokinetic contexts generally range from 10 to 50 µg/mL [8][9], whereas toxic concentrations are considered to exceed 100 µg/mL [10]. These concentration ranges define the relevant monitoring targets for both environmental surveillance and clinical analysis, providing benchmarks for evaluating sensor performance and analytical sensitivity.

Although instrumental techniques such as chromatography and mass spectrometry have been developed for ibuprofen detection in biological fluids and environmental samples [11][12], these approaches are often expensive, time-consuming, and require specialized personnel, limiting their

suitability for large-scale or rapid screening. Consequently, there remains a pressing need for sensitive, rapid, and cost-effective methods for ibuprofen monitoring.

5.2 Principle of bimodal interferometry

Interferometric optical biosensors are among the most sensitive label-free detection platforms developed to date. However, despite their high sensitivity and precision, the practical implementation of traditional interferometric configurations, such as the Mach-Zehnder interferometer, has been limited by fabrication complexity and performance variability.

In conventional MZI devices, a Y-junction is required to divide and recombine the light propagating through two distinct arms (the sensing and reference arms). The sensitivity of the device strongly depends on the fringe visibility (V), defined as

$$V = \frac{I_{MAX} - I_{MIN}}{I_{MAX} + I_{MIN}}, \tag{5-1}$$

which must approach unity to achieve optimal performance. Achieving high visibility requires symmetric couplers with a 3 dB coupling factor (k = 0.5), minimal Y-junction losses, and equal propagation losses in both arms. In practice, these requirements impose tight fabrication tolerances at the nanometric scale, making the process highly demanding and often resulting in reduced reproducibility and performance. Furthermore, recombination of out-of-phase optical beams at the output coupler can excite higher-order modes that are radiated away in single-mode structures [13], further complicating device optimization [14].

To overcome these challenges, a simplified interferometric configuration, known as the Bimodal Waveguide Interferometer, was developed [15]. This architecture eliminates the need for a Y-splitter by confining two optical modes within a single waveguide, allowing them to interfere directly. The BiMW consists of a straight rib waveguide that initially supports only the fundamental mode (TE_{00}). At a designed step junction, where the waveguide core thickness increases by a few nanometers, the first-order mode (TE_{10}) is also excited. Both modes then co-propagate along the same waveguide segment and accumulate a phase difference, which forms the basis of the interferometric signal.

This structural simplification offers several key advantages. The absence of a Y-coupler reduces optical losses and fabrication complexity, while the propagation of both modes within a single path ensures identical environmental and propagation conditions, improving device reproducibility and

stability. The mode distribution and interference efficiency are controlled simply by adjusting the core thickness during fabrication, a process fully compatible with standard lithographic techniques.

The BiMW operates with transverse electric (TE) polarized light. When the input beam reaches the bimodal section, both the fundamental (TE_{00}) and first-order (TE_{10}) modes are excited. These modes exhibit distinct propagation constants and evanescent field distributions: the TE_{00} mode remains largely confined within the SiN core, whereas the TE_{10} mode extends further into the external medium [16]. As a result, the TE_{10} mode is more responsive to refractive index changes occurring near the sensor surface [17].

A sensing window is opened in the bimodal section, allowing the evanescent field to interact directly with the external environment. Here, a bioreceptor layer is immobilized to provide molecular selectivity. When a target analyte binds to the functionalized surface, the local refractive index changes ($n_0 \rightarrow n_0'$), which modifies the effective refractive indices of the two modes ($n_{eff,00}$ and $n_{eff,10}$). Because the two modes experience different degrees of confinement, this perturbation induces a relative phase shift ($\Delta\Phi$) between the modes, expressed as:

$$\Delta\Phi = \frac{2\pi L}{\lambda}\left(n_{eff,10} - n_{eff,00}\right) \tag{5-2}$$

where L is the length of the sensing region and λ is the operating wavelength. The interference between the two modes at the output produces an intensity distribution described by:

$$I_{out} = I_{00} + I_{10} + 2\sqrt{I_{00}I_{10}}\cos\Delta\Phi\ , \tag{5-3}$$

where I_{00} and I_{10} are the modal intensities of the fundamental and first-order modes, respectively. Any biomolecular interaction at the sensing surface modifies the local refractive index, leading to a measurable shift in the interference pattern. This phase shift can be correlated quantitatively with the analyte concentration, enabling real-time, label-free detection. The schematic configuration and sensing principle of the BiMW device are illustrated in Figure 5.1.

The bulk refractive index sensitivity (S_{bulk}) of the BiMW can be theoretically defined as:

$$S_{bulk} = \frac{\Delta\Phi}{\Delta n} = \frac{2\pi L}{\lambda}\left(\frac{\partial n_{eff,10}}{\partial n} - \frac{\partial n_{eff,00}}{\partial n}\right)\ , \tag{5-4}$$

This relation shows that the overall sensor response is governed by the difference in the modal sensitivities of the two guided modes to external refractive index variations. The higher penetration depth of the TE_{10} mode contributes to enhanced sensitivity, while the stable confinement of the

TE_{00} mode ensures signal robustness, making the BiMW architecture a powerful platform for precise interferometric biosensing.

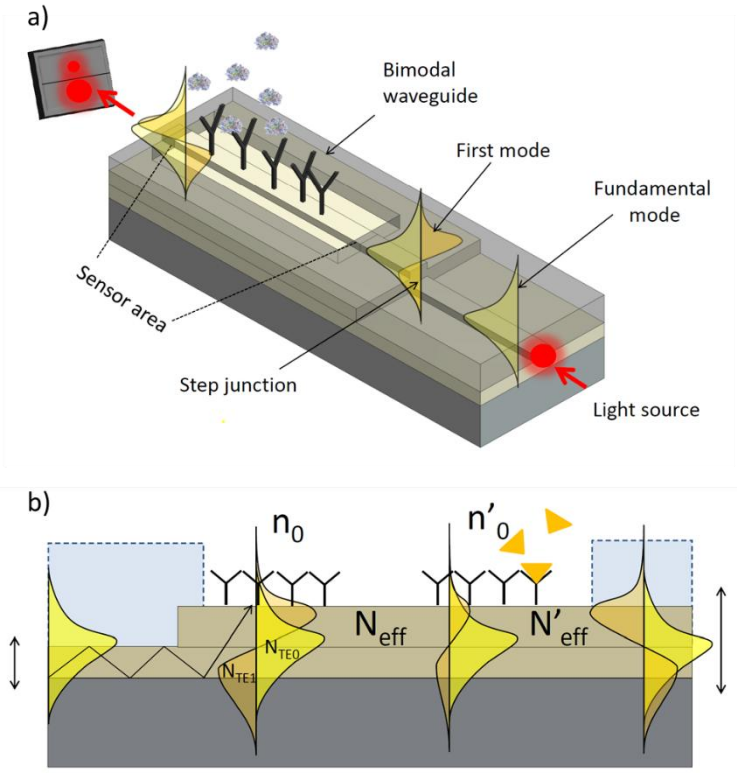

Figure 5.1: a) Schematic representation of the BiMW device. b) Operating principle of the BiMW biosensor, where light coupled into the single-mode waveguide is converted into two propagating modes that interfere along the sensing region before reaching the output [18].

5.3 BiMW Sensor Platform for Ibuprofen Detection

5.3.1 BiMW Interferometer Platform

The Silicon-based BiMW sensor chips used in this research were fabricated at the Infraestructura Científica y Técnica Singular (ICTS) Clean Room facilities of the Microelectronic National Center (IMB-CNM- CSIC) in Barcelona (Spain). The bimodal waveguide interferometric biosensor platform developed and employed throughout this work is illustrated in Figure 5.2. The BiMW sensor chip is mounted on a custom-made holder equipped with a three-axis translation platform**,** enabling precise spatial alignment and optimal coupling of the input light beam.

To minimize thermal fluctuations that could affect the intrinsic sensitivity of the BiMW biosensor, a Peltier thermoelectric cooler (TEC3-2.5, Thorlabs, New Jersey, USA) and a temperature controller are positioned behind the sensor chip. This system provides temperature stabilization with an accuracy of 0.01 °C, ensuring highly stable operating conditions during sensing experiments.

The optical setup employs a TE-polarized diode laser (λ = 660 nm, Hitachi, Tokyo, Japan) as the light source. The beam is coupled into the BiMW sensor through a lens system composed of a collimating lens (C240TME-D, Thorlabs, New Jersey, USA), a polarization-dependent isolator (IO-3D-660-VLP, Thorlabs, New Jersey, USA), and a 40× coupling objective (Achro, Leica, Wetzlar, Germany). The resulting interference pattern generated by the two guided modes is detected by a two-sectional photodetector (Hamamatsu Photonics, Hamamatsu, Japan) and processed via a data acquisition card (National Instruments, Texas, USA).

On top of the sensor chip, a PDMS microfluidic cell is mounted to establish controlled contact between the liquid sample and the sensing region of the BiMW. The microfluidic system consists of a five-channel PDMS cell with individual channel dimensions of 18.5 mm × 1.25 mm × 0.5 mm (L × W × H). A syringe pump (Darwin, Paris, France) ensures a continuous buffer flow, typically Milli-Q water or PBS for biological experiments, usually at approximately 20 µL min^{-1}, while a six-port injection valve (CHEMINERT®, VICI, Texas, USA) enables the controlled injection of analyte solutions without interrupting the flow. This setup ensures stable flow conditions, accurate sample delivery, and reproducible biosensing performance.

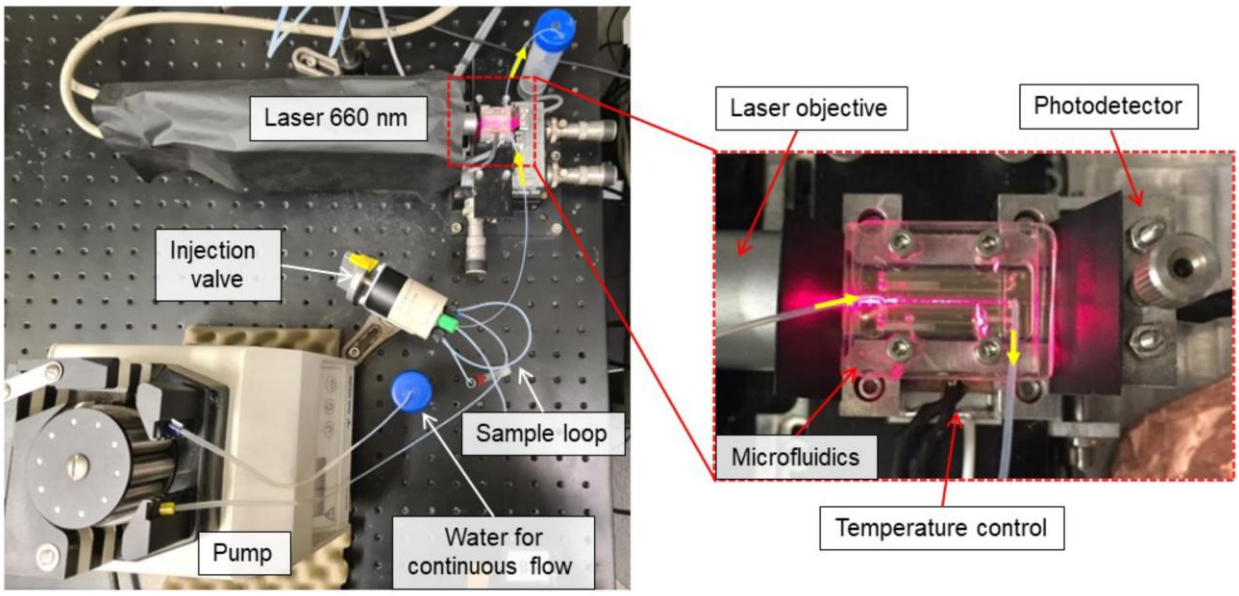

Figure 5.2: Photograph of the BiMW sensor chip mounted on its holder equipped with a temperature controller, while polarized laser light (λ = 660 nm) is coupled into the waveguide. The zoomed-in schematic provides an enlarged view of the bimodal waveguide, highlighting its key structural features [19].

5.3.2 Signal Interpretation

Real-time signal acquisition and processing are performed using a custom software developed in Python. The raw BiMW interferometric signal is inherently periodic with respect to phase

variations, which makes the direct readout of phase shifts ambiguous and nonlinear (Figure 5.3a). To overcome this limitation, a phase-modulation and demodulation system is implemented to generate a linear and continuous output.

This system operates by modulating the incident wavelength and subsequently applying a Fourier transform deconvolution algorithm (Figure 5.3b, top), which converts the periodic interferometric pattern into a real-time, linear signal (Figure 5.3b, bottom) [20]. As a result, the phase shifts (Δφ, rad) between the two guided modes can be continuously monitored and accurately quantified during sensing experiments.

The processed output is represented as sensorgrams, which depict temporal changes in the signal. These traces provide direct information on the biomolecular interactions occurring at the BiMW sensing surface.

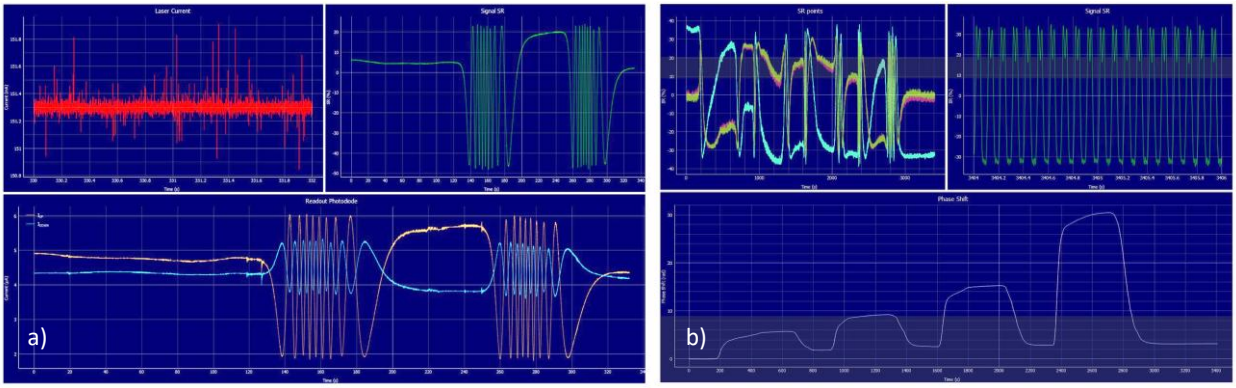

Figure 5.3: Screenshots of two different tabs in the readout software employed showing: a) the raw interferometric signal detected by the two-section photodiode from the modulated laser beam, and b) the applied deconvolution function (top) together with the resulting linearized signal (bottom).

5.3.3 Evaluation of the BiMW Biosensor Sensitivity

The bulk refractive index sensitivity of the BiMW biosensor was assessed by constructing a calibration curve based on the injection of successive HCl solutions with different refractive indices (0.025 M, 0.05 M, 0.1 M, 0.25 M, and 0.5 M). Milli-Q water was used as the running buffer. During each injection, the resulting phase variation (Δφ) due to the refractive index change between water and the corresponding HCl solution was monitored in real time (Table 5.1, Figure 5.4a). The measured phase shifts were then plotted as a function of the refractive index variation (Δn) to evaluate the bulk sensitivity of the device (Figure 5.4b).

Table 5.1: Refractive index variations produced by HCl solutions of different concentrations and the corresponding phase shifts (Δφ) recorded using the silicon-based BiMW sensor chip.

HCl Concentrations (M)	Δn (RIU)	Δϕ (rad)
0.025	2.3×10^{-4}	2.6
0.05	3.9×10^{-4}	4.7
0.1	6.9×10^{-4}	9.13
0.25	1.92×10^{-3}	25.2
0.5	3.41×10^{-3}	44.66

The calibration curve displayed a linear trend, with a bulk sensitivity (S_{bulk}) of 13166 rad·RIU^{-1}, confirming the high precision and reproducibility of the BiMW biosensor response. The LOD was found to be 8.45×10^{-7} RIU. These results demonstrate that the BiMW interferometric sensor exhibits a remarkably high refractive index sensitivity, comparable to or even exceeding that of other reported interferometric waveguide devices [21].

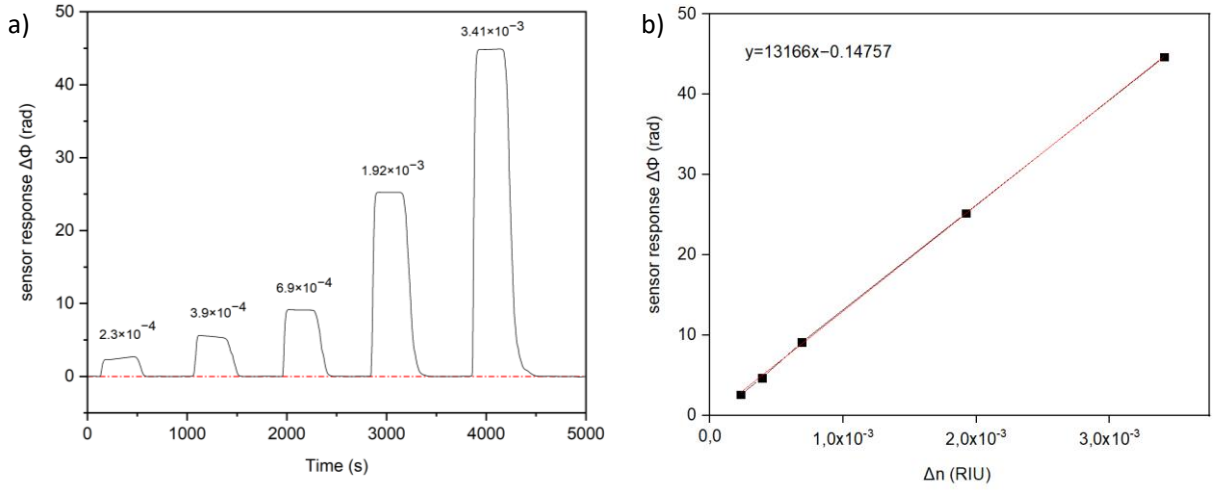

Figure 5.4: a) Real-time sensorgram obtained for successive HCl solutions using the BiMW platform. b) Calibration curve used to determine the bulk sensitivity of the silicon-based BiMW sensor, illustrating the relationship between refractive index variation (Δn) and the corresponding phase shift (Δφ).

5.3.4 Results about Sensor Functionalization and Immobilization Steps for Ibuprofen Detection

To investigate the performance of the BiMW biosensor for ibuprofen detection, two surface functionalization strategies were implemented: a Silane-PEG-COOH functionalization and an

APTES-based amine functionalization. Both methods were followed by the covalent immobilization of an HAS-ibuprofen conjugate, which served as the recognition element in a competitive immunoassay. After immobilization, a range of anti-ibuprofen antibody solutions at different concentrations were injected to determine an optimal working concentration for subsequent assay development.

The first approach employed a Silane-PEG-COOH-functionalized surface, as discussed previously in Section 2.4.1. Following sequential chemical cleaning, plasma treatment, and nitric acid oxidation, the sensor surface was silanized with silane-PEG-COOH at 4 °C for two hours. The modified surface was then rinsed, dried, and thermally cured at 121 °C for 90 minutes to ensure stable silane bonding. The carboxyl groups of the PEG coating were activated using EDC/NHS chemistry, after which a solution of HAS-ibuprofen conjugate (20 $\mu g \cdot mL^{-1}$) was injected for covalent attachment. Residual active sites were blocked with ethanolamine to minimize nonspecific adsorption.

Following surface blocking, the running buffer was switched from water to PBS or PBST to better mimic physiological conditions, and the system was equilibrated before immunoassay testing. Despite careful surface preparation, however, no measurable binding of anti-ibuprofen polyclonal antibodies (pAb-IBU) was observed at any tested concentration. This lack of response was likely caused by a buffer mismatch between the running buffer and the antibody diluent, which may have induced minor refractive index fluctuations and masked the actual signal. This limitation motivated the evaluation of an alternative surface chemistry to enhance immobilization efficiency and signal stability.

The second functionalization strategy employed an APTES-based amine-terminated surface. After the same cleaning and oxidation sequence, the sensor was incubated for one hour in a solution containing 1 vol.% APTES and 0.3 vol.% N,N-diisopropylethylamine in anhydrous toluene. The APTES-coated surface was rinsed, dried under nitrogen, and thermally cured at 110 °C for one hour. In this method, the HAS-ibuprofen conjugate was pre-activated in solution using EDC/NHS chemistry to form reactive NHS-esters, which readily coupled with surface amines to create stable amide bonds. This indirect coupling approach promotes efficient and oriented immobilization of the conjugate.

During immobilization, a pronounced phase shift of approximately 48.5 rad was recorded, confirming successful attachment of the HAS-ibuprofen conjugate. After immobilization, the running buffer was switched from water to PBS or PBST, and the system was equilibrated before

introducing antibody solutions. Low concentrations of anti-ibuprofen antibodies (below 30 $\mu g \cdot mL^{-1}$) did not generate measurable phase shifts, whereas higher concentrations (30, 40, and 50 $\mu g \cdot mL^{-1}$) produced clear sensor responses indicative of specific binding events at the sensor surface. The corresponding immobilization sensorgram for HAS-ibuprofen at 20 $\mu g \cdot mL^{-1}$, as well as the sensorgrams obtained for antibody concentrations between 30 and 50 $\mu g \cdot mL^{-1}$, are shown in Figure 5.5a and 5.5b, respectively. The resulting calibration curve derived from these data (Figure 5.5c) highlights the quantitative response of the BiMW sensor to varying antibody concentrations. Although the initial experiments focused on relatively high antibody levels, ongoing optimization aims to reduce antibody consumption while maintaining sensitivity and reproducibility.

Based on these findings, the APTES-based amine functionalization proved more suitable for the BiMW sensor platform in this study, enabling robust conjugate immobilization and consistent detection of antibody binding events. This method therefore provides a reliable and efficient surface chemistry for competitive immunoassay-based ibuprofen detection.

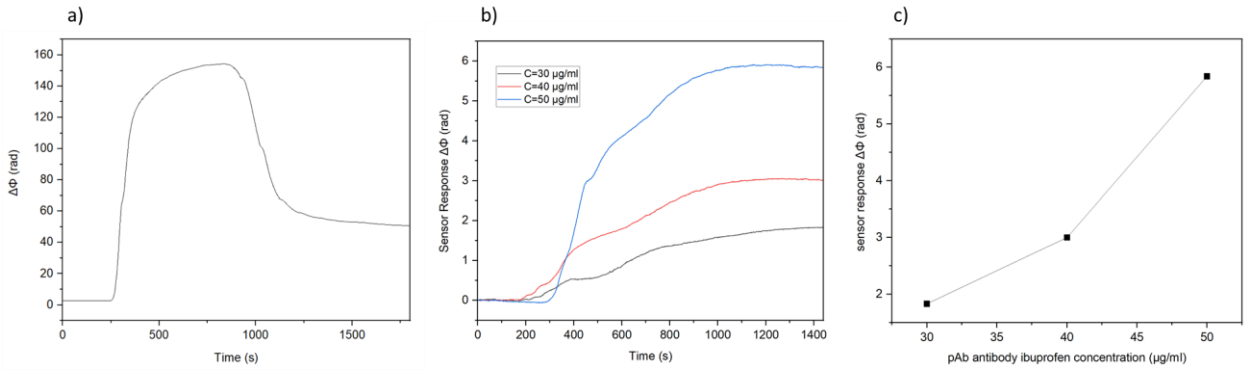

Figure 5.5: a) Sensorgram showing the immobilization of HSA-ibuprofen at 20 $\mu g \cdot mL^{-1}$. b) Sensorgrams depicting the response to different pAb antibody ibuprofen concentrations (30, 40, and 50 $\mu g \cdot mL^{-1}$). c) Corresponding calibration curve derived from the sensor responses to high pAb antibody ibuprofen concentrations.

5.3.5 Competitive immunoassay principle for ibuprofen detection

In a competitive immunoassay, the concentration of free analyte in solution is determined by its ability to compete with an immobilized conjugate for a limited number of antibody binding sites. For the BiMW ibuprofen assay, HAS-ibuprofen is immobilized on the sensor surface through functionalization, acting as the antigen. A mixture containing free ibuprofen at varying concentrations and a fixed concentration of anti-ibuprofen polyclonal antibodies is injected over the functionalized surface.

During the assay, free ibuprofen molecules in the solution compete with the immobilized HAS-ibuprofen conjugate for antibody binding. As a result, higher concentrations of free ibuprofen lead to fewer antibodies binding to the sensor surface, thereby producing a smaller phase shift in the interferometric signal. Conversely, at low ibuprofen concentrations, more antibodies are available to bind to the immobilized conjugate, resulting in a larger sensor response. Figure 5.6 illustrates the sequence of steps involved in the competitive immunoassay.

A calibration curve can be generated by plotting the sensor response (phase shift) as a function of the ibuprofen concentration, enabling quantitative correlation between the measured signal and the analyte level. The BiMW ibuprofen sensor is designed to provide rapid, label-free detection with high sensitivity. Compared to conventional chromatographic techniques, the BiMW assay offers shorter analysis times and real-time monitoring. Additionally, the platform is versatile and can be adapted to other small-molecule drugs or biomarkers by changing the conjugate-antibody pair.

As further steps of this research, optimization is required to refine the experimental protocol, particularly to adjust the buffer composition, optimize conjugate density, determine the optimal lower concentration of pAb-IBU, and perform competitive immunoassay trials in which free ibuprofen competes with the immobilized conjugate.

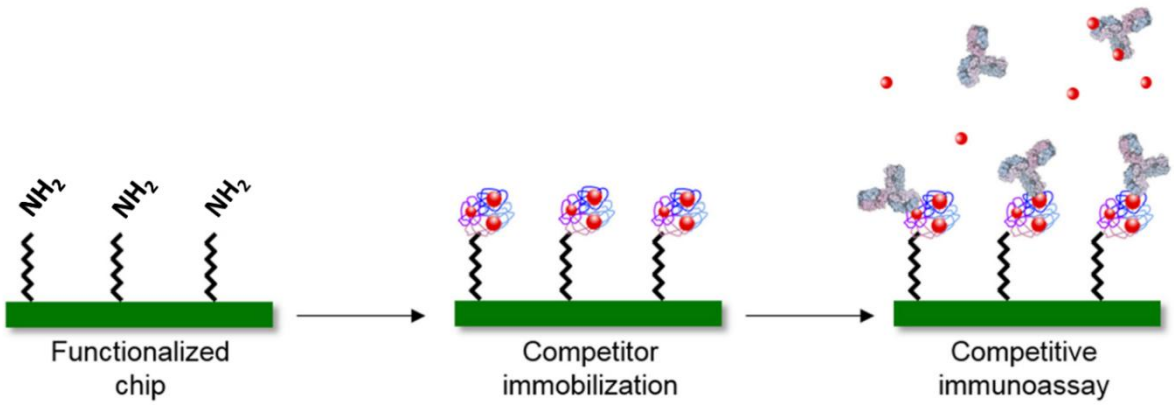

Figure 5.6: The process of a competitive immunoassay on a BiMW sensor, showing the APTES-functionalized sensor surface, competitor immobilization, and the competitive immunoassay steps [22].

5.4 References

[1] C. A. Pierce and B. Voss, “Efficacy and Safety of Ibuprofen and Acetaminophen in Children and Adults: A Meta-Analysis and Qualitative Review,” *Annals of Pharmacotherapy*, vol. 44, no. 3, pp. 489–506, Mar. 2010, doi: 10.1345/aph.1M332.

[2] C. Litalien and E. Jacqz-Aigrain, “Risks and Benefits of Nonsteroidal Anti-Inflammatory Drugs in Children,” *Paediatr Drugs*, vol. 3, no. 11, pp. 817–858, 2001, doi: 10.2165/00128072-200103110-00004.

[3] L. Hunter, D. Wood, and Dargan, “The patterns of toxicity and management of acute nonsteroidal anti-inflammatory drug (NSAID) overdose,” *Open Access Emergency Medicine*, p. 39, Jul. 2011, doi: 10.2147/OAEM.S22795.

[4] S. Chopra and D. Kumar, “Ibuprofen as an emerging organic contaminant in environment, distribution and remediation,” *Heliyon*, vol. 6, no. 6, p. e04087, Jun. 2020, doi: 10.1016/j.heliyon.2020.e04087.

[5] K. M. Jeffries, S. M. Brander, M. T. Britton, N. A. Fangue, and R. E. Connon, “Chronic exposures to low and high concentrations of ibuprofen elicit different gene response patterns in a euryhaline fish,” *Environmental Science and Pollution Research*, vol. 22, no. 22, pp. 17397–17413, Nov. 2015, doi: 10.1007/s11356-015-4227-y.

[6] J. Jan-Roblero and J. A. Cruz-Maya, “Ibuprofen: Toxicology and Biodegradation of an Emerging Contaminant,” *Molecules*, vol. 28, no. 5, p. 2097, Feb. 2023, doi: 10.3390/molecules28052097.

[7] D. S. Singh and S. Pflugmacher, “Ecotoxicological assessments of over-the-counter NSAID (diclofenac, ibuprofen, aspirin) and antipyretic (acetaminophen) pharmaceuticals: a review of their toxicity effects on aquatic crustaceans,” *Integr Environ Assess Manag*, Jun. 2025, doi: 10.1093/inteam/vjaf082.

[8] D. R. Mehlisch and J. Sykes, “Ibuprofen blood plasma levels and onset of analgesia,” *Int J Clin Pract*, vol. 67, pp. 3–8, Jan. 2013, doi: 10.1111/ijcp.12053.

[9] G. M. E. Janssen and J. F. Venema, “Ibuprofen: Plasma Concentrations in Man,” *Journal of International Medical Research*, vol. 13, no. 1, pp. 68–73, Jan. 1985, doi: 10.1177/030006058501300110.

[10] W. Holubek, A. Stolbach, S. Nurok, O. Lopez, A. Wetter, and L. Nelson, “A report of two deaths from massive ibuprofen ingestion,” *Journal of Medical Toxicology*, vol. 3, no. 2, pp. 52–55, Jun. 2007, doi: 10.1007/BF03160908.

[11] T. Hložek, M. Bursová, and R. Čabala, “Fast ibuprofen, ketoprofen and naproxen simultaneous determination in human serum for clinical toxicology by GC–FID,” *Clin Biochem*, vol. 47, no. 15, pp. 109–111, Oct. 2014, doi: 10.1016/j.clinbiochem.2014.06.076.

[12] L. M. Madikizela and L. Chimuka, “Determination of ibuprofen, naproxen and diclofenac in aqueous samples using a multi-template molecularly imprinted polymer as selective

adsorbent for solid-phase extraction," *J Pharm Biomed Anal*, vol. 128, pp. 210–215, Sep. 2016, doi: 10.1016/j.jpba.2016.05.037.

[13] L. M. Lechuga, F. Prieto, and B. Sepúlveda, "Interferometric Biosensors for Environmental Pollution Detection," 2004, pp. 227–250. doi: 10.1007/978-3-662-09111-1_10.

[14] F. Prieto *et al.*, "An integrated optical interferometric nanodevice based on silicon technology for biosensor applications," *Nanotechnology*, vol. 14, no. 8, pp. 907–912, Aug. 2003, doi: 10.1088/0957-4484/14/8/312.

[15] K. E. Zinoviev, A. B. Gonzalez-Guerrero, C. Dominguez, and L. M. Lechuga, "Integrated Bimodal Waveguide Interferometric Biosensor for Label-Free Analysis," *Journal of Lightwave Technology*, vol. 29, no. 13, pp. 1926–1930, Jul. 2011, doi: 10.1109/JLT.2011.2150734.

[16] D. Grajales García, "Lab-on-a-chip integration of the bimodal waveguide nanointerferometric biosensor," 2018, Accessed: Nov. 04, 2025. [Online]. Available: https://ddd.uab.cat/record/202182

[17] L. Chrostowski *et al.*, "Silicon photonic resonator sensors and devices," A. V. Kudryashov, A. H. Paxton, and V. S. Ilchenko, Eds., Feb. 2012, p. 823620. doi: 10.1117/12.916860.

[18] S. Herranz, A. F. Gavela, and L. M. Lechuga, "Label-Free Biosensors Based on Bimodal Waveguide (BiMW) Interferometers," 2017, pp. 161–185. doi: 10.1007/978-1-4939-6848-0_11.

[19] O. Calvo-Lozano *et al.*, "Integration of Metal–Organic Polyhedra onto a Nanophotonic Sensor for Real-Time Detection of Nitrogenous Organic Pollutants in Water," *ACS Appl Mater Interfaces*, vol. 15, no. 33, pp. 39523–39529, Aug. 2023, doi: 10.1021/acsami.3c07213.

[20] S. Dante, D. Duval, D. Fariña, A. B. González-Guerrero, and L. M. Lechuga, "Linear readout of integrated interferometric biosensors using a periodic wavelength modulation," *Laser Photon Rev*, vol. 9, no. 2, pp. 248–255, Mar. 2015, doi: 10.1002/lpor.201400216.

[21] A. Fernández Gavela, D. Grajales García, J. Ramirez, and L. Lechuga, "Last Advances in Silicon-Based Optical Biosensors," *Sensors*, vol. 16, no. 3, p. 285, Feb. 2016, doi: 10.3390/s16030285.

[22] P. Ramirez-Priego, M.-C. Estévez, H. J. Díaz-Luisravelo, J. J. Manclús, Á. Montoya, and L. M. Lechuga, "Real-time monitoring of fenitrothion in water samples using a silicon nanophotonic biosensor," *Anal Chim Acta*, vol. 1152, p. 338276, Apr. 2021, doi: 10.1016/j.aca.2021.338276.

Chapter 6: Conclusion and Perspectives

6.1 Conclusion of the thesis

This thesis has been devoted to the development of advanced photonic platforms for biosensing, where nanostructured devices, functional materials, and surface chemistry are combined to achieve high sensitivity and selectivity in biomolecular detection. The research has progressed from the theoretical understanding of the fundamental optical phenomena to the realization of practical devices for molecular diagnostics and biochemical interaction studies. By integrating fundamental optical physics with materials engineering and biochemical functionalization, the work advances the field of photonic biosensors both in theoretical understanding and practical application.

The main contributions of this thesis can be summarized as follows:
(i) design and experimental demonstration of a BIC-based MIP sensor achieving 10 fM detection of TGF-β in complex fluids; (ii) development of a photonic crystal slab platform for highly precise SPARC–HSA kinetic measurements at sub-nanomolar concentrations; (iii) adaptation of a BiMW interferometric platform for small-molecule sensing via competitive immunoassays, applied to ibuprofen detection.

The first part of the thesis established the scientific foundations on which the experimental research was built. Chapter 1 presented the fundamentals and properties of photonic crystals, outlining their historical development, classification, and role in modern nanophotonics. Particular attention was devoted to the theoretical description of light-matter interactions, photonic band structures, and the formation of photonic bandgaps, which together determine how periodic dielectric materials control the propagation of light. In this context, the concept of bound states in the continuum emerged as a particularly powerful mechanism for achieving extreme light confinement and ultra-high Q-factor resonances. This phenomenon provided the physical basis for the BIC-enabled sensing architectures in Chapters 3 and 4, demonstrating how theoretical insights can be translated into high-performance sensing platforms.

Following this theoretical foundation, Chapter 2 introduced the broader field of optical biosensors, discussing their motivations, operational principles, and comparative advantages for real-time,

label-free detection. The chapter reviewed the main types of optical biosensors, including surface plasmon resonance, ring resonators, interferometric sensors, and photonic crystal sensors, emphasizing their transduction mechanisms and performance metrics. It also analyzed the critical role of surface functionalization in enabling specific biological recognition. Different strategies, such as silane–PEG–COOH and APTES-based amine chemistries, were evaluated in terms of their influence on biomolecule immobilization and antifouling behavior. These insights were later used in the practical implementation of the photonic devices described in the subsequent chapters, particularly in optimizing the MIP–BIC sensor and BiMW interfaces.

With this theoretical framework established, Chapter 3 described the design and realization of a molecularly imprinted polymer sensor integrated with a photonic nanostructure supporting bound states in the continuum. This device was developed for the selective and label-free detection of TGF-β, an important biomarker in clinical diagnostics. By coupling the high field enhancement of BICs with the molecular selectivity of MIPs, the sensor achieved detection limits as low as 10 fM, comparable to or exceeding the performance of many conventional immunoassays reported in the literature. The MIP-BIC hybrid structure demonstrated not only excellent sensitivity but also remarkable robustness against nonspecific binding, confirming its ability to operate effectively in complex biological environments. The successful validation of this sensor in spiked saliva samples represented a decisive step toward its potential application in point-of-care diagnostics, showing that synthetic receptors integrated into photonic architectures can provide reliable and reusable alternatives to conventional immunoassay platforms. To the best of our knowledge, this represents one of the first demonstrations of a MIP-based photonic BIC sensor achieving femtomolar detection in complex media.

The research then advanced toward studying dynamic biomolecular interactions through optical sensing, as detailed in Chapter 4. This chapter presented an all-dielectric photonic crystal slab integrated with microfluidics to investigate the binding between SPARC and HSA. This engineered photonic configuration enabled precise, real-time monitoring of molecular interaction kinetics at sub-nanomolar concentrations. The dissociation constant, measured as 8.2 ± 0.8 nM, was determined with with a level of accuracy comparable to or surpassing established methods such as SPR, with the additional advantages including all-dielectric architecture and flexibility of integration. Beyond its analytical performance, this work demonstrated the potential of BIC-based sensors as a versatile optical tool for investigating protein-protein interactions relevant to cancer biology and drug delivery, such as the role of SPARC–albumin interactions in albumin-bound drug formulations.

he final part of this thesis focused on the detection of small molecules using bimodal waveguide technology, with ibuprofen serving as a model analyte. This platform required a different approach because small molecules typically induce weak optical responses due to their low molecular mass. To overcome this limitation, the BiMW system was adapted to perform competitive immunoassays, using immobilized HAS-ibuprofen conjugate as a recognition interface. Silane-PEG-COOH and APTES-based amine functionalization approaches were explored to improve surface stability and immobilization efficiency. Despite still being at the optimization stage, these experiments demonstrated that the BiMW configuration could be tailored for small-molecule detection, extending the versatility of integrated photonic biosensors to pharmaceutical and environmental monitoring.

Considering all the findings, the work presented in this thesis demonstrates that distinct photonic platforms can be rationally designed and chemically functionalized to address a wide range of biosensing applications. Across the explored photonic systems, including BIC-based photonic crystals and BiMW interferometers, the results demonstrate how light-matter interaction can be precisely controlled to enhance sensitivity, while functional materials such as MIPs or tailored surface chemistries provide the necessary selectivity for specific targets. From a scientific perspective, the research advances the understanding of how optical phenomena, surface modification, and fluidic integration interact to define the overall performance of these biosensors. It also Suggests the feasibility of scalable, reproducible platforms that can bridge laboratory research and real-world diagnostic applications.

6.2 Further steps

The outcomes of this work pave the way for several promising directions for future investigation. BIC-based photonic crystal sensors and BiMW interferometers are inherently compatible with dense spatial and spectral multiplexing, and could evolve toward multiplexed detection systems capable of monitoring multiple biomarkers simultaneously [1], thereby enabling comprehensive diagnostic panels on a single chip. Advancing integration with microfluidic systems [2] and automated data analysis would facilitate portable, point-of-care instruments suitable for clinical deployment. Continued progress in functional materials, such as responsive polymers and hybrid organic-inorganic coatings, is expected to enhance specificity and reusability [3], while the integration of data-driven methodologies, including machine-learning algorithms [4], could further refine signal interpretation and predictive accuracy. In addition, further research and experimental validation are required to finalize the Ibuprofen detection studies based on the BiMW platform,

ensuring reliable performance and extending its applicability to pharmaceutical monitoring [5]. These directions outline a clear path from laboratory prototypes to robust, user-friendly biosensing technologies. Altogether, these directions outline a clear path from the proof-of-concept photonic biosensors developed in this thesis to robust, user-friendly biosensing technologies suitable for clinical and industrial environments.

6.3 References

[1] K. R. Mitchell, J. E. Esene, and A. T. Woolley, "Advances in multiplex electrical and optical detection of biomarkers using microfluidic devices," *Anal Bioanal Chem*, vol. 414, no. 1, pp. 167–180, Jan. 2022, doi: 10.1007/s00216-021-03553-8.

[2] Q. Wang, C. Wang, X. Yang, J. Wang, Z. Zhang, and L. Shang, "Microfluidic preparation of optical sensors for biomedical applications," *Smart Medicine*, vol. 2, no. 1, Feb. 2023, doi: 10.1002/SMMD.20220027.

[3] L. S. Puumala *et al.*, "Biofunctionalization of Multiplexed Silicon Photonic Biosensors," *Biosensors (Basel)*, vol. 13, no. 1, p. 53, Dec. 2022, doi: 10.3390/bios13010053.

[4] W. J. Chin, W. Y. Lim, S. M. Khor, N. Ramakrishnan, P. S. Chee, and C.-H. Goh, "Advancement of machine learning algorithms in biosensors," *Clinica Chimica Acta*, vol. 579, p. 120677, Jan. 2026, doi: 10.1016/j.cca.2025.120677.

[5] X. Wang, L. Cohen, J. Wang, and D. R. Walt, "Competitive Immunoassays for the Detection of Small Molecules Using Single Molecule Arrays," *J Am Chem Soc*, vol. 140, no. 51, pp. 18132–18139, Dec. 2018, doi: 10.1021/jacs.8b11185.

List of Publications

1. Zito, G., Siciliano, G., Seifalinezhad, A., Miranda, B., Lanzio, V., Schwartzberg, A., Gigli, G., Turco, A., Rendina, I., Mocella, V., Primiceri, E., & Romano, S. (2024). Molecularly Imprinted Polymer Sensor Empowered by Bound States in the Continuum for Selective Trace-Detection of TGF-beta. Advanced Science, 11(41). https://doi.org/10.1002/advs.202401843
2. Miranda, B., Mele, V., Seifalinezhad, A., Zito, G., Schwartzberg, A., Mocella, V., Rendina, I., Lamberti, A., Sanità, G., & Romano, S. (2025). Resolving SPARC–HSA binding kinetics with an ultrasensitive photonic sensor based on bound states in the continuum. Biosensors and Bioelectronics, 288, 117754. https://doi.org/10.1016/j.bios.2025.117754
3. Miranda, B., Seifalinezhad, A., Rendina, I., Schwartzberg, A., Riminucci, F., Mocella, V., Zito, G., & Romano, S. (2024). All-dielectric optical biosensors based on bound states in the continuum: a new paradigm in healthcare and food quality assessment. In Proc. SPIE 13109, Metamaterials, Metadevices, and Metasystems, 131090F. https://doi.org/10.1117/12.3028102

Acknowledgment

I would like to express my deepest gratitude to **Dr. Vito Mocella** and **Dr. Silvia Romano**, my supervisors, for their invaluable guidance, continuous support, and trust throughout my doctoral studies. Their confidence in my abilities has been a great source of motivation, and I sincerely hope to have met their expectations and made them proud. Their insightful scientific direction, constructive advice, and constant encouragement have been fundamental to both my academic and personal growth.

My sincere appreciation also goes to **Dr. Ivo Rendina**, whose inspiration, support, and kindness have been a great motivation throughout these years. His encouragement has greatly influenced my professional development.

I am deeply thankful to **Dr. Elisabetta Primiceri** and her team for their continuous support during my time at CNR, for their valuable collaboration in the experiments.

My heartfelt thanks extend to **Professor Agostino Iadicicco**, **Professor Stefania Campopiano**, and **Professor Flavio Esposito** for their constant understanding and dedication to supporting international students. Their efforts in fostering a welcoming and inclusive academic environment have made my experience far more comfortable and enriching. I am especially grateful for their continuous help and encouragement throughout these three years.

I would also like to thank **Professor Laura Lechuga** and her research group at the Catalan Institute of Nanoscience and Nanotechnology (ICN2) in Barcelona for their kind support and collaboration during my exchange period.

I am sincerely grateful to my colleagues and friends at CNR-ISASI and Parthenope University, **Emanuela Esposito**, **Gianluigi Zito**, **Karen Caicedo**, **Gennaro Sanità**, **Federica Donadio**, **Bruno Miranda**, **Mozhgan Attena**, **Amin**, **Babak** and **Pegah**, for the helpful discussions, cooperation, and the pleasant working atmosphere we shared in the laboratory. Your friendship has made this journey far more enjoyable.

Finally, my deepest gratitude goes to my **family**, for their endless love, unwavering support, and encouragement through every challenge. They have been my greatest motivation and strength during difficult times.

This PhD journey has been an unforgettable experience, one filled with challenges, growth, and invaluable lessons that I will carry with me throughout my life.

Aida